Republic of Iraq

Quarterly Refereed Journal for Natural and Engineering Sciences

Issued by
Al-`Abbas Holy Shrine
International Al-`Ameed Centre for Research and Studies

Licensed by
Ministry of Higher Education
and Scientific Research

Fifth Year, Ten Volume, Issues 19 and 20
Muharram, 1441, September 2019

Secretariat General
of Al-'Abbas
Holy Shrine

Al-Ameed Interna-
tional center
for Research and Studies

Print ISSN: 5721 – 2312
Online ISSN: 0083 – 2313
Consignment Number in the Housebook and Iraqi
Documents: 1996, 2014
Postal Code: 56001
Mailbox: 232

Al-Abbas Holy Shrine. International Al-`Ameed Centre for Research and Studies.

ALBAHIR : Quarterly Refereed Journal for Natural and Engineering Sciences \ Issued by Al-`Abbas Holy Shrine International Al-`Ameed Centre for Research and Studies. - Karbala, Iraq : Abbas Holy Shrine, International Al-`Ameed Centre for Research and Studies, 1436 hijri = 2015-

Volume : Illustrations ; 24 cm

Quarterly.- Fifth Year, Ten Volume, Issue 19 and 20 (September 2019)-

ISSN 5721-2312

Includes bibliographical references.

Text in English ; summaries in English and Arabic.

1. Science--Periodicals. A. title.

LCC : Q1.A1 A8365 2019 VOL. 10 NO. 19-20

DDC : 016.505

Cataloging Center And Information Systems / Library and House of Manuscripts of Al-Abbas Holy Shrine

Mobile: +9647602355555
+9647602323337
http://albahir.alkafeel.net
Email:albahir@alameedcenter.iq

Editorial Board

Consultation Board

Publication Conditions

In as much as Al-`Bahir- effulgent- Abualfadhal Al-`Abbas cradles his adherents from all humankind, verily Al-Bahir journal does all the original scientific research under the conditions below:

1. Publishing the original scientific research in the various scientific sciences keeping pace with the scientific research procedures and the global common standards; they should be written in English .
2. The research should not be published before under any means .
3. The research should adhere the academic commonalties; the first page maintains the title, researcher name /names, address, mobile number under condition that the name, or a hint , should never be mentioned in the context and keywords should be written in Arabic and English as there is an abstract in Arabic and English.
4. The Research studies should be delivered to us either via Journal website http://albahir.alkafeel.net , after filling the two standard format the first with the name of the researcher and the second without in Word .
5. The page layout should be (2)cm .
6. The font should be of (16 bold),Time New Roman, subtitles of (14 bold) and also the context.
7. The space should be single, indentation should not be, as 0 before, 0 after and no spacing, as 0 before, 0 after.
8. There should be no decoration and the English numeral should proceed to the last text.
9. Any number should be between two brackets and then measurement unit, for instance: (12) cm .
10. All sources and references should be mentioned at the end of the article and categorized in conformity with Modern Language Association (MLA), for instance : Name of Author/ Authors, Journal Name Volume Number, pages from - to, (year).
11. There should be a caption under a diagram in 10 dark, for instance: Fig(No.): Title or explanation. Similarly done with tables but over a diagram. for instance: Table(No.): Title or explanation.
12. Diagrams , photos and statics should be in colour with high resolution without scanning.

13. The marginal notes, when necessary, should be mentioned at the end of the article before the references.

14. Wherever there is the word “ figure” should be abbreviated as Fig. and table should be Table.

15. The pages never exceed 25 pages.

16- Rersearch chapers should be numbered as 1- Introduction and so on , if there is a subtile to the main tiltle , it is to be as 1.2 , 2.2 .

17. The Formulae should be written in Math Type.

18. All the ideas and thoughts reveal the mindset of the researcher not the journal and the article stratification takes technical standards.

19. All the articles are subject to the internet Turnitin , confidential reviewing to prove its academic merits , the processes are as follows :

20-

a- The researcher is notified that his paper is received within 14 days in maximum.

b- The article is to be sent to the researcher as soon as it does not meet the requirement of the publication conditions.

c- The researcher is notified that his article is accepted.

d- The articles need certain modification , as the reviewers state, are sent to the researchers to respond in a span of a month from the date of dispatch.

e- The researcher is to be notified in case the article is rejected.

f- The researcher is to be granted an edition containing his article.

21. Priorities are given in concordance to :

a. The articles participated in the conferences held by the publication institute.

b. The date of receiving.

c. The date of acceptance.

d. The importance and originality of the article.

e. The diversity of the fields the articles maintain in the meant edition.

22. The researchers should appeal to the modifications the language and scientific reviewers find in the articles.

23. The researcher should fill the promise paper having the publication rights of the Scientific Al-Bahir Journal and adhering to integrity conditions in writing a research study.

*Open Access publishing does have its cost; however, for this journal, no

In the Name of Allah
Most Compassionate, Mort Merciful

Edition Word

Thanks to the Evolver of the world and prayer and peace be upon Abu Al-Qassim Muhammad and his Immaculate and Beneficent Progeny .

Two editions of Al-Bahr Journal heave into horizons and emanate from the ambition of the personnel as there is a diversity of peer reviewed scientific articles . With great inspiration such provides the scientific process in Iraq and the world with the latest and innovative products , to fathom the unfathomable and to take hold of the main achievement of a scientific major.

As far as it concerns itself with the engineering and natural sciences , the current articles parade such fields to seal these editions with a scientific innovation worth paying heed and esteem under such extraordinary circumstances Iraq endures .

In such an occasion , we do lay the hands of the reader on these scientific products to stimulate the morale of influence and being influenced in the intellectual orbit of the researchers first to innovate, second to maintain such a scientific impetus and last to reconnoitre the academic updated studies that require specific inquiries and acts of profound research .

Thanks be to Him for everything

Consultation and Editaril

The Transitivity of One Disconnecting Arc Spaces

Iftichar Al shraa and Alia›a Hussein
Mathematics Department, College of Education for pure Sciences,
University of Babylon ,Iraq.

Received Date: 31 / 10 / 2016
Accepted Date: 10 / 2 / 2017

الخلاصة

لتكن D فضاء القوس المفصول بنقطة و $f:D\to D$ دالة مستمرة في هذا العمل نتوصل الى :

1. اذا كانت f دالة متعدية فان مجموعة النقاط الدورية كثيفة .
2. f تكون متعدية و تمتلك نقطة دورية فردية الدوار دوارها اكبر من الواحد اذا وفقط اذا f^2 تكون متعدية و f تمتلك نقاط دورية كثيفة .
3. f^2 تكون متعدية و f تمتلك نقاط دورية كثيفة اذا وفقط اذا f متعددة كليا .
4. تكون متعددة كليا اذا وفقط اذا f تكون تبولوجي خلط .
5. اذا كانت f دالة خطية رتيبة فان f تكون تبولوجي خلط اذا وفقط اذا لكل قوس $K\subseteq D$, يوجد n بحيث ان $f^n(K)=D$.

الكلمات المفتاحية

(النقاط الدورية، تبولوجي التعدي، تبولوجي الخلط، مجموعة الغاية، قوس مفصول بنقطة).

Abstract

Let D be a one disconnecting arc space, f:D→D be a continuous map, in this work we get:

1- If f is transitive map. Then the set of all periodic points is dense in D.

2- If f is transitive and has a point of odd period greater than one if and only if f^2 is transitive and f has dense periodic points.

3- f^2 is transitive and f has dense periodic points if and only if f is totally transitive

4- f is totally transitive if and only if f is topologically mixing.

5- If f is piecewise monotone Then f is topologically mixing if and only if for every arc K⊆D, there is an n such that f^n (K)=D.

Keywords

Periodic point, topological transitive, topological mixing, limit set, one disconnecting arc.

1. Introduction

A several authors have been studied the transitive maps, periodic points and other chaotic properties on one dimensional spaces for examples (the circle, the real interval and graph maps etc). In [1] Alseda, Kolyada, Llibre and Snoha, (1990) studied if X is connected and a compact topological space and if f a transitive map with one disconnecting arc. In [2] Sabbaghana M., Damerchiloob H. , (2011), proved that it is not necessary to assume that X is connected. In this research we will generalize some of the results and theorems on the new space.

2. Preliminary

In this paper, we prove that there are relations between the transitivity and periodicity, also the transitivity with topological mixing.

2.1. Definition [6]

The orbit of p is the set of points $p,f(p),f^2(p),\ldots$ And is denoted by $orb(p)=\{f^n(p)|n\in N_\circ\}$ where $N_\circ=N\cup\{0\}$.

A point $p\in X$ is a periodic point of f if there exists a positive integer $n \in N$ such that $f^n(p)=p$. If p is a periodic point of period n ,then we say that orbit of p is a periodic orbit of period n. It is called the period of f. We denote the set of periodic points by per(f) and the set the period of f is denote by p(f).

2.2. Definition

We say that D has one disconnecting arc say J if J is an open subset of D homeomorphic with an open interval of R and when Y is the connected component of D which contains J, then for all x in J the set Y -{x} has exactly two connected components.

2.3. Definition

Let $a,b\in D$, we say that $a\rhd b$ if a follows counterclockwise to b .

2.4. Definition [3]

We say that the map f is transitive(Do) if $\exists x\in X$ such that the orbit $\{f^n(x)|n\geq 0\}$ is dense in X , that is $\bar{}(\{f^n(x)|n\geq 0\})=X$.

2.5. Definition [4]

Let $f:X\to X$ be a continuous map , if f is transitive , we say that f is totally transitive if f^n is transitive for all integers n>1 .

2.6. Definition [3]

Let $f:X\to X$ be a continuous map, we say that f is topological mixing if for every pair non-empty open sets U and V in X , there exists a positive integer n such that $f^k(U)\cap V\neq\emptyset$ for every k>n.

2.7. Definition [5]

Let X be a metric space, and let $f:X\to X$ be a continuous map. The ω -limit set of $x\in X$, denoted by ω(x,f), is the set of cluster points of the forward orbit $\{f^n(x)\}_{n\in N}$ of the iterated functionf. Hence, $y\in\omega(x,f)$ if and only if there is a strictly increasing sequence of natural numbers $\{n_k\}_{k\in N}$ such that $f^{n_k}(x)\to y$ ask$\to\infty$. Another way to express this is $\omega(x,f)=\cap_{n\in N}\bar{}\{f^k$

(x)|k>n} where $\bar{A}$ denotes the closure of the set A.

2.8. Proposition [6]

A continuous map f:X→X of a compact metric space into itself is transitive if and only if there exists a point x∈X such that ω(x,f)=X.

2.9. Lemma [2]

Let X be a topological space and let f: X → X be a transitive map. If X has a connected component with nonempty interior, then X has only a finite number of connected components and they form a regular periodic decomposition. That is, $\bigcup_{i=0}^{n-1} D_i$ where for each $0< i < n-1$, D_i is the closure of an open set and for every $0 \le i < j \le n-1$, $D_i \cap D_j$ is nowhere dense and for each positive integer k, $f^k(D_i) \subseteq D_{i+k(modn)}$.

The set $D = \{ D_0, D_1, ..., D_{n-1}\}$ is called a regular periodic decomposition for f on X.

2.10. Lemma [6]

If f:X→X is a continuous map, then the following statements are equivalent:

1) f is transitive.

2)for every non-empty open set W in X , $\bigcup_{n=1}^{\infty} f^n(W)$ is dense in X.

3) for every pair of non-empty sets U and V in X , there is a positive integer k such that $f^{-k}(U) \cap V \neq \emptyset$.

4) for every non-empty open set W in X , $\bigcup_{n=1}^{\infty} f^{-n}(W)$ is dense in X.

5)for every proper closed invariant subset of X has empty interior.

2.11. Theorem [2]

Let X be a compact space and let X have a disconnecting interval . Let also f:X →X be a transitive map. Then the set of all periodic points of f is dense in X.

3.Main Result:

Some theorems and lemmas are proved, we generalize the results of the spaces from R to R to maps from the one disconnecting arc space to itself :

3.1. Proposition

Let f:D→D be transitive map and the set of all limit points of f of a point x in D is D .Then exactly one of the following conditions holds:

1) the set of all limit points of f^s of a point x in D is D, for every positive integer s.

2) there exist non-degenerate closed arcs J and K with J∪K=D and J∩K={y} where y is a fixed point of f such that f(J)=K and f(K)=J.

Proof:

Let r be an arbitrary integer and $B_r=\omega(f^k(x), f^r)$ and for $0\le k<r$. Since $B_0 \cup B_1 \cup \ldots \cup B_{r-1}=D$ at least of B_k has nonempty interior. Moreover since the orbit of x cannot folding the arc to the a point. Since $f(B_k)=B_{k+1}$ for $0\le k<r$ and $f(B_{k-1})=B_0$, it follows that each B_i. We claim that if the interior of B_k and B_j intersect then $B_k=B_j$. To see that suppose that $B^\circ_k \cap B^\circ_j \neq \emptyset$. Then for some positive integer n $f^{rn+i}(x) \in B^\circ_k \cap B^\circ_j$

It follows that $B_k \subseteq B_j$. Since B_j is f^r-invariant and $B_k=\omega(f^{kn+i}(x),f^r)$. Since k,j can be interchanged.

Let A denote the collection of subsets of D which are component of $int(B_k)$ for some $k\in\{0,\ldots,r-1\}$. Then by Lemma 2.9 D has n connected components. Since A is finite. We may assume that has one connected component say E_1. Then $F_1=\bar{}(E_1)$ .So we have $B_k=D$ for k=0,…,r-1 . Since f is transitive, then by proposition 2.8 $\omega(x,f)=D$.

Now suppose that A have two connected components E_1 and E_2 such that $F_1=\bar{}(E_1)$ and $F_2=\bar{}(E_2)$. Let y be a fixed point. If $y\in E_1,E_2$. Then $f(F_1)=F_1$ and $f(F_2)=F_2$ which is impossible. If y cannot to be endpoint of arc in D. The only possibility y is that y is a common endpoint of F_1 and F_2. Then $f(F_1)=F_2$ and $f(F_2)=F_1$. Thus we have (2) satisfy and hence f^2 is not transitive. Since r is arbitrary, this proves that (1) satisfied if f^2 is transitive and (2) satisfied if is not.

3.2. Lemma

Let f:D→D be transitive.Then of the following holds:

1) f^2 is transitive in which f^(r+l) is transitive ∀r≥1,l≥0.

2) f^2 is not transitive in which case $D=\bar{}(\{f^2n(x)|n\in N_\circ\})\cup\bar{}(\{f^{2n+1}(x)|n\in N_\circ\})$ and $\bar{}(\{f2n(x)|n\in N_\circ\})\cap\bar{}(\{f^{2n+1}(x)|n\in N\_^\circ\})\neq\emptyset$ and $f(\bar{}(\{f^2n(x)|n\in N_\circ\}))=\bar{}(\{f^{2n+1}(x)|n\in N_\circ\})$ and $f(\bar{}(\{f^{2n+1}(x)\,|\,n\in N_\circ\}))=\bar{}(\{f^2n(x)|n\in N_\circ\})$. Moreover ∀l≥1, $\{f^2ln(x)|n\in N_\circ\}$ is dense in $\bar{}(\{f^2n(x)|n\in N_\circ\})$ and $\{f^{2ln+1}(x)|n\in N_\circ\}$ is dense in $\bar{}(\{f^{2n+1}(x)|n\in N_\circ\})$.

Proof:

Let r be an integer, r≥1and for each integer s ,0≤s≤r-1, let $B_s=\bar{}(\{f^{rn+s}(x)|n\in N_\circ\})$. Then since $\bigcup_{s=0}^{r-1}\{f^{rn+s}(x)|n\in N_\circ\}=\{f^n(x)|n\in N_\circ\}$, this implies that $\bigcup_{s=0}^{r-1}B_s=D$. Then there is an s $0\le s\le r-1$, thus $B_s^\circ\neq\emptyset$. Since f is transitive, so by Lemma 2.9 $D=\bigcup_{s=0}^{r-1}B_s$, for each $0\le s\le r-1$ and ∀ $0\le i,j\le r-1$, $B_i\cap B_j$ is nowhere dense and for each positive integer k, $f^k(B_r)\subseteq B_{r+kmodn}$.

Now we must prove that if $B_i^\circ\cap B_j^\circ\neq\emptyset$, then $B_i^\circ=B_j^\circ$.

If $B_i^\circ\cap B_j^\circ\neq\emptyset$, then there is a positive integer n , so that $f^{2n+i}(x)\in B_i^\circ\cap B_j^\circ$, and there is a sequence $n_1,n_2,n_3,\ldots$of positive integer such that $f^{n_k r+j}(x)\to f^{rn+i}(x)$. Then for every integer m>0 we have $f^{r(n_k+m+j)}(x)\to f^{r(n+m)+i}(x)$.

This implies that $\bar{}(\{f^{rn+i}(x), f^{r(n+m)+i}(x),.\})\subset B_j$ and hence that $B_i\subset B_j\cup\{f^i(x), f^{r+i}(x),\ldots, f^{(n-1)r+i}(x)\}$.Then $B_i^\circ\subset B_j^\circ$. In the same way we can prove that $B_j^\circ\subset B_i^\circ$, and so $B_i^\circ=B_j^\circ$.

Let h be a component of B_s° such that $H=\{h|$for some $s,0\le s\le r-1\}$. Since D has n of components. Then $H=\{h_1, h_2, \ldots, h_n\}$. Let $F_i=\bar{}(h_i)$. Since h_i is finite, and so F_i is finite and hence the set $\{F_1, F_2, \ldots, F_n\}$ is finite . By transitivity , we get the set $\{F_1, F_2, \ldots, F_n\}$ is permuted by f. We next prove that n≤2. Let p be a fixed point of f. If $p\in nF_i^\circ$, then $f(F_i)=F_i$ which is impossible unless n=1 . In the same way, if p is an endpoint of D, then n=1. If p is a common endpoint of F_i and F_j , then $f(F_i)=F_j$ and $f(F_j)=F_i$ which is satisfied only if n=2 . Notice that the integer n depend on s. It

follows that we will refer n as n(r).

Now we satisfy the conclusion of the Lemma, so we first suppose that f^2 is transitive. Let r be an integer, $r\geq 0$ and suppose that n(r)=2. Then there are closed arcs $F_1$and $F_2$with $F_1\cup F_2=D$, $F_1\cap F_2=\{pt\}$, $f(F_1)= F_2$ and $f(F_2)=F_1$.

Suppose that $x\in F_2$, we see that, for each m, $f^{2m}(x)\in F_2$ and hence $\{f^{2n}(x)|n\in N_\circ\}\cap F_1^\circ\neq\emptyset$. Which is contradiction with the fact that f^2is transitive, and hence n(r)=1 . Then $\forall s, 0\leq s\leq r-1$, $B_s= D$. Then $\bar{}(\{f^{rn+s}(x)\mid n\in N_\circ\})=$ D and so $f^{r+s}$is transitive. This implies that for any integer $l\geq 0$, f^{r+l} is transitive.

Next suppose that f^2 is not transitive. Let r=2. Since f^2 is not transitive $B_\circ\neq D$ and so n(2)=2 .Now let j be an integer, $j\geq 1$.Then for each integer k, $\{f^{2jn+k}(x)\mid n\in N_\circ\}\subset\{f^{2n+k}(x)\mid n\in N_\circ\}$, and since $\bar{}(\{f^{2}n(x)\mid n\in N_\circ\})\neq D$, we have n(2j)=2.

Since the common endpoints of F_1 and F_2 is the only fixed point for the map f.Then the arcs F_1 and F_2 which we construct for r=2j are independent of j. Since by assumption $x\in F_2$, we have $F_2=\bar{}(\{f^{2}n(x)\mid n\in N_\circ\})$, $F_1\bar{}(\{f^{(2n+1)}(x)\mid n\in N_\circ\})$ for each integer $l\geq 1$, $\bar{}(\{f^{2}ln(x)\mid n\in N_\circ\})= F_2$ and $\bar{}(\{f^{2}ln(x)\mid n\in N_\circ\})=F_1$. This establishes the Lemma.

In the same way the proof of Theorem 2.11, we can prove that the next Theorem:

3.3. Theorem

Let f:D→D be transitive map. Then the set of all periodic point is dense in D.

3.4. Theorem

f2 is transitive and f has dense periodic points if and only if for each arc K in Dand each pair $a, b\in D^\circ$, there is an integer M such that n>M then $[a,b]\subset f^n(K)$.

Proof:

Suppose that f^2 is transitive and f has a dense periodic points. Let K be an arc in D. Since the periodic points of fare dense, there is a periodic point $q\in K^\circ$.Suppose that q has a periodic point of period j. Let $g=f^j$. Let $E=\bar{}(\bigcup_{n=0}^{\infty} g^n(K))$ .Then E is a closed arc. Let $z\in K^\circ$such that $\{f^{2}n(z)\mid n\in N_\circ\}$ is dense D. Then f^2 is transitive .Thus from Lemma 3.2, we get $\{g^n(z)\mid n\in N_\circ\}$ is dense in D. This implies that g is transitive. Hence E=D.

We will prove that if q is aperiodic point such that $orb(q)\subset D^\circ$, then there is an integer t such that $orb(q)\subset f(K)^t$.

To see that, suppose that q is a periodic point with period l and $orb(q)\subset D^\circ$. Let $p_1\in orb(q)$ such that p_1 is the nearest point of begin point of D and let $p_2\in orb(q)$ such that p_2 is the furthest point of begin point of D.

Suppose that $p_1\neq q$. Since $\bigcup_{n=0}^{\infty} g^n(K)=D^\circ$, there is an integer r such that $[p_1,q]=g^s(K)$. Let $h=g^s$ and observe that $h^l(p_1)= p_1$, $h^l(q)=q$. By Lemma 3.2, there is a point $y\in[p_1, q]^\circ$ such that $\{h^{l}n(y)|n\in N_\circ\}$ is dense in D, and hence h^l is transitive.

Therefore there is an integer r such that $p_2\rhd h^{l}r(y)$. Then we have $h^l r(q)=q$, $h^l r(p_1)= p_1$, and $p_2\rhd h^l r(y)$. This implies that $orb(q)\subset[p_1, p_2]\subset f^{l}r(K)$. Thus for r=l.r.s.j, we have $orb(q)=f^t(K)$. Then if $r\geq t$, $orb(q)\subset f^r(K)$.

Now suppose that a,b∈D° and that a⊳b. Let c and d be periodic points such that [a,b]⊂[c,d] and orb(c)∪orb(d)⊂D°. Then there are a positive integer r_1 and r_2 such that orb(c) ⊂ f^{r_1} (K) and orb(d) ⊂f^{r_2}= (K) .Let N=max{r_1, r_2}. Then if n>N, [a,b]⊂[c,d]⊂f^n (K).

Suppose that for each arc K in D and each pair a,b∈D°, there is a positive integer N such that if n>N, then [a,b]⊂f^n (K). We must prove that f is transitive. Let U be an open arc in D, and let x∈U. We will prove that $\bigcup_{n=0}^{\infty} f^n(x)$ is dense in D . If not, there is a closed arc K such that $K\cap\bigcup_{n=0}^{\infty} f^n(x)=\emptyset$. But by the condition, there is a positive integer k such that x∈f^k (K). Hence, there is a point y∈K such that $f^k(y)=x$. Then y∈K∩U_(n=0)$^{\infty}$ f^{-n} (x). Thus $\bigcup_{n=0}^{\infty} f^{-n}(x)$ is dense in D. Since x∈U, and so $\bigcup_{n=0}^{\infty} f^{-n}(U)$ is dense in D. Then by Lemma 2.10 f is transitive. Since f is transitive . Then there is a point y∈D such that $\{f^n(y)|n\in N_\circ\}$ is dense in D.

If f^2 is not transitive. Hence $\{f^{2n}(y)|n\in N_\circ\}$ is not dense in D, then this implies that there are closed arcs F_1 and F_2 in D such that $F_1\cup F_2$=D, $F_1\cap F_2$={pt}, $f(F_1)=F_2$ and $f(F_2)=F_1$.

Let a∈F_1°, b∈$F_2^\circ$and let K be F_1. Then for each positive integer [a,b]⊄f^n (K).This is contradiction the assumption that [a,b]⊂f^n (K). Since f is transitive, then by Theorem 3.3 f has dense periodic points and hence f^2 has a dense orbit .This implies that f^2 is transitive and this is establishes the theorem.

3.5. Theorem

If f^2 is transitive and f has a dense periodic points then f has a point of odd period.

Proof:

Let K and L be arcs in D such that K∩L=∅. Then by Theorem 3.3, there is a positive integer N such that if n>N, then (K∪L)⊂f^n (K)∩f^n (L). Let r be a positive integer which is prime and larger than 2N+2. Let i=((r-1))/2,j=(r+1)/2.Then i>N,j>N, and i+j=r.

Now, since K⊂f^i (L), there is an arc L_1 of L such that f^i (L_1)=K. Then $L_1\subset f^j(K)=f^{i+j}(L_1)=f^r(L_1)$. Then there is a point y∈L_1 such that f^r (y)=y. Since y∈L_1, f^j (y)∈K,and K∪L=∅., this implies that f(y)≠y.Since r is prime we have the period of y is r. This establishes Theorem.

In [7] coven proved that the following theorem for maps from R to itself. We will generalize the same theorem to maps from D to itself.

3.6. Proposition

Let f:D→D be a continuous map .Then f is transitive and has a point of odd period greater than one if and only if f^2 is transitive and f has dense periodic points .

Proof:

Suppose that f is transitive and has a point of odd period greater than one. Since f is transitive. Then by Proposition 3.2 , f^2 is transitive and by Theorem 3.5 f has a dense periodic point.

Now Suppose that f^2 is transitive and f has a dense periodic point. Since f^2 is transitive .

Then by Definition 2.4, f is transitive .Since f^2 is transitive and f has a dense periodic point. Then by Theorem 3.4 f has a point of odd period.

3.7. Proposition

Let f:D→D be a continuous map. Then f^2 is transitive and f has dense periodic points if and only if f is totally transitive map.

Proof:

Suppose that f^2 is transitive and f has a dense periodic point. Then by Proposition 3.2, f^n is transitive for every n>0 and hence f is totally transitive.

Now Suppose that f is totally transitive. Then by Definition 2.4 f^2 is transitive and by Theorem 3.5f has dense periodic points.

3.8. Proposition

Let f:D→D be a continuous map, f is totally transitive if and only if f is topologically mixing.

Proof:

Case (1): To prove the topological mixing map imply the totally transitive

Assume that f is topologically mixing. Then By Definition 2.4, for every pair of non-empty open sets U and V in X there exists a positive integer n such that $f^n(U)\cap V\neq\emptyset$ and Definition 2.8 implies, there exists a positive integer n such that $f^k(U)\cap V\neq\emptyset$ for every k>n . Hence f^n is transitive for every n>0 and so f is totally transitive.

Case two (2): suppose that f^n is transitive for every n>0 imply the topological mixing map . Since f^n is transitive for every n>0 .Then f^2 and f are transitive .So by Theorem 3.5 f has a dense periodic point. Thus by proof of Theorem 3.3 f is topologically mixing.

3.9. Proposition

Let f:D→D be a continuous map and f is piecewise monotone, f is totally transitive if and only if for every arc K⊆D, there is an n such that f^n (K)=D.

Proof:

Assume that f is totally transitive. To prove that for every arc K⊆D, there is an n such that f^n (K)=D. We have two cases:

Case one: there is an arc L⊆D^°such that f^2 (L)=D . If K is an arc such that K⊆D . Then by Proposition3.7 , f^2 is transitive and f has dense periodic points and by Theorem 3.3 , there is an n such that L⊆f^n (K). Thus f^(n+2) (K)=D.

Case two :assume that $f^2(L)\neq D$ for every arc L⊆D^°. Let e_1 be start point in D and e_2 be endpoint in D. Since f is onto, either $f^{-1}(e_1)\subseteq\{e_1,e_2\}$ or $f^{-1}(e_2)\subseteq\{e_1,e_2\}$. This implies that either $f^2(e_1)=\{e_1\}$ or $f^2(e_2)=\{e_2\}$. We assume the former. Let q be the smallest turning point of f^2. Then f^2 has no fixed points in (e_1,q) and $y\rhd f^2(y)$ for every $y\in(e_1,q)$. (If not, then $y\rhd f^2(y)$ for every $y\in(e_1,q)$, and hence $[e_1,q]$ is f^2-invariant). But $f^2[q,e_2]\subseteq[m,e_2]$ for some m> 0 . Thusf^2n $[q,e_2]\subseteq[m,e_2]$ for every n > 0, contradicting the assumption that f^2 is

transitive.

Now suppose that for every arc $K \subseteq D$, there is an n such that $f^n(K)=D$. Then immediately f is totally transitive.

Reference:

[1] Alseda L., Kolyada S., Llibre J., Snoha L., Entropy and periodic points for transitive maps, Trans. Amer. Math. Soc., No. 351, pp, 1551-1573, (1999).

[2] Sabbaghana M., Damerchiloob H., A note on periodic points and transitive maps, Mathematical Sciences, Vol. 5, No. 3, pp. 259-266, (2011).

[3] Fotiou A., Deterministic chaos, University of London, MSc Thesis, (2005).

[4] Banks, J., Regular Periodic Decomposition for Topologically Transitive Maps, Ergodic Theory and Dyn. sys., Vol.17, pp. 505-529, (1997).

[5] Bae, J. S. and Yang S. , ω -limit Sets for Maps of The Circle, Bull. Korean, Math. Soc., Vol. 25 No.2 pp. 233-242, (1988).

[6] Block, L. S. and Coppel, W.A., Dynamics in one dimension, Notes in math., No. 1513, Springer-Verlag, Berlin, (1992).

[7] Coven, E. M. and Mulvey, I., Transitivity and The Centre for Maps of the Circle, Ergod. Th. & Dynam. Sys., 6, PP.1-8, (1986).

Analysis for X-Ray Diffraction Pattern of Annealed Fe2O3Thin Films

Mustafa Shakir Hashim, Amira Jawad Kadhim, Reem saadi Khaleel,
Esraa Akram Abbas
Physics department, Education College, Almustansiriya University.

Received Date: 10 / 5 / 2017
Accepted Date: 16 / 1 / 2018

الخلاصة

وظفت موديلات وليمسن- هول المُعدّلة لإيجاد التغيرات في المَعْلمات التركيبية لأغشية اوكسيد الحديد مع زيادة درجة حرارة التلدين. هذه النماذج هي موديل وليمسن- هول للمطاوعة الموحدة الخواص، موديل وليمسن- هول للمطاوعة غير الموحدة الخواص، وموديل وليمسن- هول لكثافة الطاقة. ولحساب الحجم الحبيبي أُستخدِمت معادلة شيرر ومعادلة شير المُعَدّلة، ايضا حُسِبَ الحجم الحبيبي، مطاوعة الشُبيكة، الاجهاد، كثافة طاقة التشوه وكثافة العيوب باستعمال هذه الموديلات. بزيادة درجة التلدين زاد الحجم الحبيبي وفقا لكل الموديلات. المطاوعه المحسوبة بثلاثة موديلات كانت سالبة وازدادت قيمتها مع زيادة درجة التلدين، وحسب موديل وليمسن- هول للمطاوعه غير الموحدة الخواص وموديل وليمسن- هول لكثافة الطاقة فان الإجهاد، كثافة الانخلاعات وكثافة طاقة إجهاد الشبيكة وصلت الى اقل قيمة لها عند درجة (500) مئوي.

الكلمات المفتاحية

هيئة القمة، تلدين، اوكسيد الحديد، معلمات التركيب المايكروي، موديلات وليمسن- هول.

Abstract

Modified Williamson-Hall (W-H) models were employed to estimate the changing of the microstructural parameters of Fe2O3 thin films with increasing annealing temperature (Ta). These models areW-H-anisotropic strain model (W-H-ASM), W-H-isotropic strain model (W-H-ISM) and W-H-energy density model (W-H-EDM). To calculate crystallite size, Scherrer equation and its modified equation were used. Also crystallite size, lattice stress, strain, dislocation density and deformation energy density have been determined by these models. By increasing Ta, crystallite sizes were increased according to all models. Three modified (W-H) models were used to calculate strain, it was negative and its values increase with Ta. According to W-H-ASM and W-H-EDM stress, dislocation density and lattice strain energy density reach minimum values when the temperature reaches (500) ^{o}C.

Keywords

Peak Profile, annealing, Fe2O3, microstructural parameters, Williamson-Hall models.

1. Introduction

Fe_2O_3 is a metal oxide has many uses [1]. In thin films field, Iron oxide has several applications. Due to its small energy gap and high absorption coefficient it is utilized as solar cell [2]. Fe_2O_3 thin film is being used in flammable gas sensing due to its fast response [3]. This material is easy to fabricate, non toxic, high chemical stability, has environmentally friendly properties, high corrosion resistance and low cost [4]. To expand the applications of Fe_2O_3 thin films its useful to estimate the microstructural properties of these films. X-ray peak profile analysis (XPPA) is important analytical method to verify this estimation. A wealth information like crystallite size, distribution of the phases in the material, strain, stress and other properties are extracted from diffraction lines of crystalline materials [5]. The aim of this contribution is applying W-H models to estimate microstructural parameters of annealed Fe_2O_3 thin films.

1.2. Theory

Bragg peaks are affected by two criteria: changing peak width or shifting peak position. From XPPA there are different models to measure crystallite size, lattice strain, stress and imperfections. The first model is Scherrer model by which crystallite size is calculated using the following equation [6]:

$$\text{Crystallite size} = k\lambda / \beta_{hkl} \cos\theta_{hkl} \quad (1)$$

Where (k=0.9) is the shape factor, λ= (0.154056) nm is the wavelength of X- rays for radiation of Cu $K\alpha_1$, in radians β_{hkl} is the widening of the hkl diffraction peak measured at half of its maximum intensity. To estimate more accurately nano-crystallite size; Monshi *et al*. utilized modified Scherrer equation using XRD [7]. The following equation is used to minimize the sources of errors by using the data from all of the available peaks.

$$\ln \beta = \ln k\lambda/L + \ln 1/\cos\theta_{hkl} \quad (2)$$

Where L is crystallite size.

The second model used to calculate lattice strain and crystallite size is (W-H-ISM) model. By assuming that the strain present in milled fishbone is isotropic; the W-H-ISM for complete widening is given by

$$\beta_{hkl} \cos\theta_{hkl} = k\lambda/L + 4\varepsilon \sin\theta_{hkl} \quad (3)$$

Where ε is strain value. If the strain is small and in all crystallographic directions the lattice deformation stress (σ) is uniform, equation (3) can be modified as following

$$\beta_{hkl} \cos\theta_{hkl} = k\lambda/L + 4\sigma \sin\theta_{hkl} / E_{hkl} \quad (4)$$

Where E is Young's modulus. In hexagonal crystals; the crystallographic direction dependent E_{hkl} is given by the next equation [8]:

$$E_{hkl} = ([h^2 + ((h + 2k)^2)/3 + (a_1/c)^2]^2) / (s_{11}(h^2 + ((h+2k)^2)/3)^2 + s_{33}(a_1/c)^4 + (2s_{13}+s_{44)} (h^2+(h+2k)^2/3) (a_1/c)2) \quad (5)$$

Where common elastic compliances for hy-

droxyapatite are $s_{11}= (7.49*10^{-12})$, $s_{13}= (-4*10^{-12})$, $s_{33}= (10.9*10^{-12})$ and $s_{44}= (15.1*10^{12})$ [9].

If extracted hydroxyapatite is not homogeneous isotropic in nature equation 3 is no longer correct to use. Also if lattice strain energy density (u) is taken into account, proportionality constants of stress-strain relation are no longer independent. By using Hook's low equation 3 will be modified as following

$$\beta_{hkl} \cos\theta_{hkl}=k\lambda/L+4[\sin\theta_{hkl} (2/E_{hkl})^{1/2}]u^{1/2} \quad (6)$$

Dislocation density (ρ) can be defined as the length of the dislocation lines per unit volume of the crystal [10]. The following equation is used to calculate ρ.

$$\rho=(12^{1/2}<\varepsilon^2>^{1/2})/(d\ L) \quad (7)$$

Where $<\varepsilon^2>^{1/2}$ is root mean squared strain, d interplanar spacing.

2. Experimental part:

On preheated glass substrates, Fe_2O_3 thin films were deposited. The optimum deposition conditions were: the spraying time 5s, temperature of substrate (200) °C, distance between nozzle and substrate was (30±1)cm and filtered air was carrier gas . As a precursor of Fe; the powder of $FeCl_3.6H_2O$ (1.6221) g dissolved in (100) ml distilled water. By using magnetic stirrer for (30) minute, complete dissolving of powder inside water was done.

The equation of decomposition is

$$2\ FeCl_3*6H_2O = 6\ HCl + 9\ H_2O + Fe_2O_3 \quad (8)$$

The thicknesses of films were estimated by weight method, its' average was (450±20) nm. To determine the orientations of Fe_2O_3 miller indices; Shimadzu X-ray diffractometer is used.

3. Results and discussions:

XRD patterns of as deposit and annealed Iron oxide thin films are shown in Fig. (1). In spite of the beginning of formation peaks along (104) and (110) directions, as deposit Fe_2O_3 sample has amorphous structure. After heat treatment, there is a transform to polycrystalline structure with dominant peak (104). Annealed samples have hexagonal phase according to standard card (JCPDS) with number (00033-0664). With increasing of Ta the sharpness of all peaks increases.

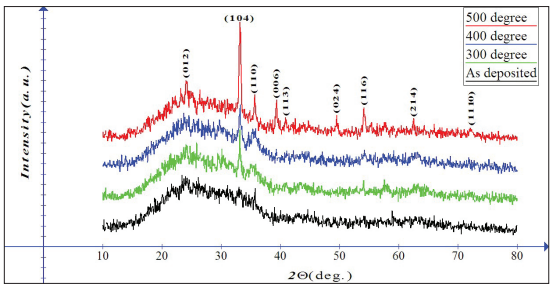

Fig. (1): XRD of as deposit and annealed samples

Equation 2 is used to draw Fig. (2) and then calculate corrected crystallite size.

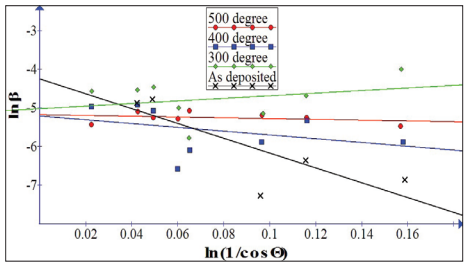

Fig. (2): Application of modified Scherrer equation to find corrected crystallite size.

Fig. (3) illustrates the variation of crystallite size and corrected one as a function to Ta.

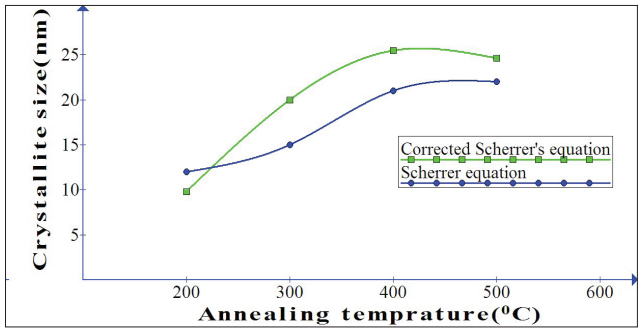

Fig. (3): Annealed crystallite sizes by using Scherrer equation.

Fig. (4) illustrates W-H-ISM plots for as deposited and annealed samples.

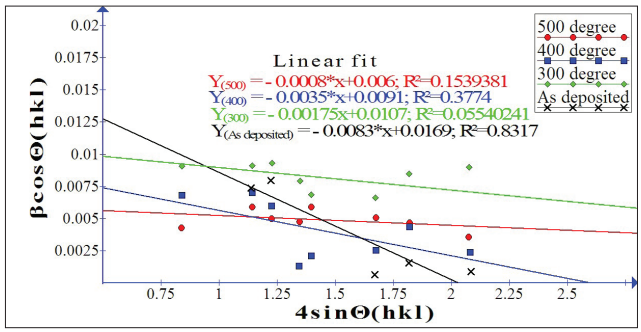

Fig. (4): W-H-ISM plots of annealed samples

Fig. (4) is used to calculate strain and crystallite size according to W-H-ISM model; i.e. using equation 3. The results of this calculation are drawn in Fig. (5). W-H-ISM model is simple technique used to separate between strain induced and size induced peak broadening as Fig. (5) show. Decreasing the total grain boundary energy produces grain growth due to the reductions of free energy [11].

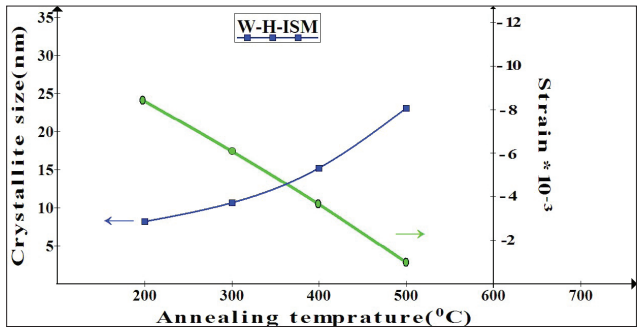

Fig. (5): Determined crystallite sizes and strain (W-H-ISM model).

In the range of current heat treatment the strain decreased with temperature and all strain's values are negative. The lattice strain is negative when crystal lattice is under the influence of compressive forces [12]. The model considers the anisotropic nature of the crystallites is called W-H-anisotropic strain model (W-H-ASM). Fig. (6) Shows $\beta \cos\Theta_{hkl}$ versus $4\sin\Theta_{hkl} / E_{hkl}$ to calculate stress and crystallite size. Fig.(7) illustrates the effect of Ta on stress and crystallite size . After calcination; the increase of crystallite size in Fig. (7) can be attributed to the reduction of defects such as dislocations that may appear in different ways [13].

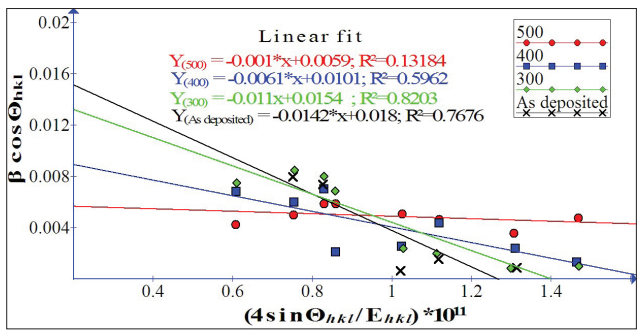

Fig. (6): W-H-ASM plots of annealed samples.

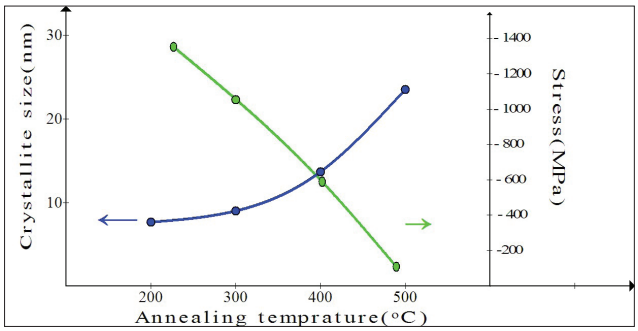

Fig. (7): Calculated crystallite sizes and stress (W-H-ASM model).

The stress reaches minimum value when the temperature reaches (500) °C. The decreased stress fields may associate with the reduction of the dislocations that decreased with heat treatment.

Table (1) illustrates calculated strain using the values of stress (calculated from Fig. 6) and $E_{(hkl)}$ (for different Millar indices). The strain values for annealed samples at (500) °C are decreased to approximately one tenth that of as deposited sample. So to remove the stress and strain from milled fishbone heat treatment at (500) °C is appropriate choice.

Table (1): Strain value according to W-H-ASM model.

Millar indices	$E_{(hkl)} *10^{11}$	$(\varepsilon = \sigma / E_{(hkl)}) *10^{-3}$			
		As deposited	°C 300	°C 400	°C 500
(012)	1.38	-102.899	-79.7101	-44.2	-7.2
(104)	1.38	-102.899	-79.7101	-44.02	-7.2
(110)	1.63	-87.1166	-67.4847	-37.4	-6.13
(006)	0.917	-154.853	-119.956	-66.5	-10.9
(113)	1.63	-87.1166	-67.4847	-37.4	-6.13
(024)	1.63	-87.1166	-67.4847	-37.4	-6.13
(116)	1.63	-87.1166	-67.4847	-37.4	-6.13

W-H-energy density model (W-H-EDM) is used to calculate the strain when the lattice strain energy density u is considered. Fig. (8) shows W-H-EDM plots.

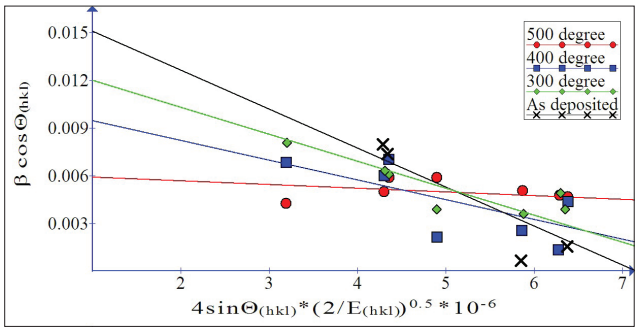

Fig. (8): W-H-EDM plots of annealed samples.

Calculated strain in Table (2) by this model is decreased with temperature but with fewer rates than that obtained by W-H-ASM model. Strain is minimized when smaller structures attach each other to form larger crystallite. It is worth to mention that surface potential is affected by the variation of strain due to its effect on bond lengths and angles [14].

Table (2): Strain value according to W-H-EDM model.

Millar indices	$E_{(hkl)}$ *10^{11}	ε =2u / $E_{(hkl)}$)$^{0.5}$ *10^{-3})			
		As deposited	°C (300)	°C (400)	°C (500)
(200)	1.63	-54.87	-45.646	-39.058	-25.901
(002)	0.917	-73.156	-60.857	-52.073	-34.532
(210)	1.59	-55.556	-46.216	-39.546	-26.225
(211)	1.56	-56.09	-46.658	-39.924	-26.476
(300)	1.56	-56.09	-46.658	-39.924	-26.476
(301)	1.51	-57.011	-47.425	-40.580	-26.919
(222)	1.52	-56.82	-47.268	- 40.446	-26.822

Fig. (9) illustrates the relationship between deformation energy density and crystallite size as a function to Ta. The heat treatment reduces the lattice strain energy density to its minimum value when the temperature reached (500) °C; this behavior might due to the ability of atoms to take their equilibrium positions at this temperature. We have seen that the crystallite sizes still increase with Ta, this confirms the improving of crystallinity of films with annealing.

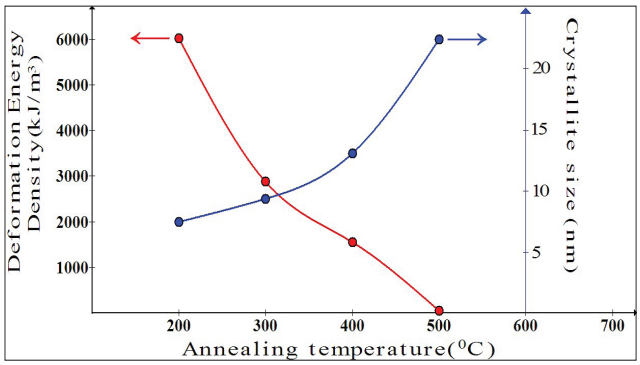

Fig. (9): Deformation energy density and crystallite size versus Ta.

The dislocation density is defined as the length of dislocation lines per unit volume. From the theoretical point view a dislocation within the crystal is a defect or a crystallographic irregularity. The defects inside the crystal have direct effect on the characteristic of the formed crystal [16].

.Fig. (10) shows the relationship between dislocation density and Ta

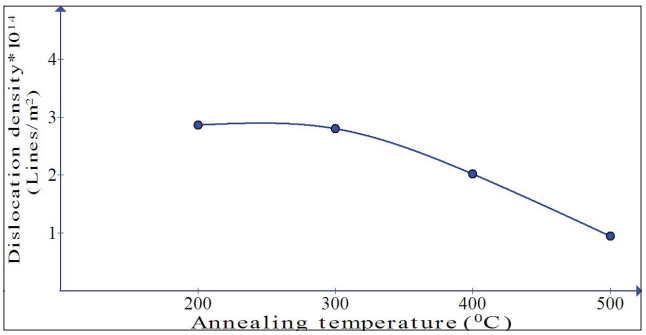

Fig. (10): Dislocation density versus Ta.

Dislocation density decreases to low value as Ta increases. So crystals with smaller dislocation density were less hardness. The formation of multiple linear defects specially dislocations which produce high dislocation density regions in the grains piling up irregular clusters into grains [15]**.**

After X-ray diffraction line profile analysis of nano $BaSr._6Fe._4TiO_3$ prepared by solid state method; Reenu Jacob and Jayakumari Isac confirmed that crystals of this material with larger dislocation density were harder. Also they found that the dislocation density increases while crystallite size decreases with increasing strain [16]. In current work; increasing of Ta produces larger crystallite size and smaller dislocation density.

The fundamental Bragg reflection can be effected by point defects (their effect on peak profile is called Huang scattering) and by dislocations. The first factor has short- range field order and the second has long- range order field [17]. The effect may appear as a shift in peak shifts (like planar defect) or peak broadening and peak shifts simultaneously (like stacking faults). Dislocation always present as a major component of lattice defects or as the only lattice defect present inside crystal lattice [14]

.

4. Conclusions:

1- In a reasonable approximation; the W-H models can be used to calculate microstructural parameters such as lattice deformation stress , lattice strain, and lattice deformation energy density.

2- To remove the stress and strain from Fe_2O_3 thin films heat treatment at (500) ^oC is appropriate choice.

3- Dislocation density decreases to low value as Ta increases.

4- The structure of Fe_2O_3 can change from amorphous to crystalline by increasing oxidation level during annealing process.

5- The present analysis can be used for understanding the stress and the strain present in the thin films through annealing.

6- The three modified forms of W-H analysis were helpful to define the crystal perfection,

References:

[1] P., Mallick, and B. N. Dash. Nanoscience and nanotechnology. 3(5),130-134, (2013).
[2] J.H.Kennedy, and D.J.Dunnwald. Electrochem. Soc. 130 , 2013-2016,(1983).
[3] K.Siroky, Jana Jirešová and Lubomír Hudec. Thin Solid Films. 245(1-2), 211-214, (1994).
[4] T.Hahn, Nathan, Heechang Ye, David W Flaherty, Allen J Bard and C Buddie Mullins. Acs Nano. 4 (4),1977-1986, (2010) .
[5] E.J. Mittemeijerv, and U. Welzel. Z.Kristallogr. 223, 552–560, (2008).
[6] S. Vives , E. Gaffet, C. Meunier. Materials Science and Engineering. A366,229-238,(2004).
[7] A. Monshi , M. Reza Foroughi , M. Reza Monshi. World Journal of Nano Science and Engineering. 2, 154-160,(2012).
[8] Y. Taraka Prabhu , K. Venkateswara Rao, V. Sesha Sai Kumar , B. Siva Kumari. World Journal of Nano Science and Engineering. 4, 21-28, (2014).
[9] D. E. Gray, American institute of physics handbook, New York McGraw-Hill Book company,(1972).
[10] B.E.Warren, E.P. Warekois. Acta Metallurgica 3, 473-479,(1955).
[11] H. Zhang, B. Chen, and J.F. Banfield. Phys Chem. Chem. Phys. 11, 2553–2558, (2009).
[12] H. Zhang and J.F. Banfield. J. Phys. Chem. B 104, 3481–3487, (2000).
[13] S. Miraghaei, P. Abachi, HR. Madaah-Hosseini, A. Bahrami. J Mater Process Technol.203(1-3), 554-60, (2008).
[14] T. Ungar , J. Gubicza , G. Ribarik , C. Pantea, T. Waldek Zerda. Carbon 40, 929–937, (2002).
[15] S. Sivasankaran, K. Sivaprasad, R. Narayanasamy and P.V. Satyanarayana. X-ray peak broadening analysis of AA 6061100 − x −x wt.% Al2O3 nanocomposite prepared by mechanical alloying. Materials characterization 6 2 (2 0 1 1) 6 6 1 – 6 7 2.
[16] R. Jacob and J. Isac. International Journal of Chemical Studies. 2(5),12-21, (2015).
[17] H.Trinkaus, Phys Stat Sol (b). 51, 307–19,(1972).

Gasification Ash Effect on the Strength and Durability of Reactive Powder Concrete

Isam Mohamad Ali
Karbala Technical Institute, Al-Furat Al-Awsat Technical University, Karbala, Iraq.

Received Date: 5 / 2 / 2018
Accepted Date: 5 / 7 / 2018

الخلاصة

أصبحت مقاومة الخرسانة للتضرر نتيجة التعرض للانجماد والذوبان ومهاجمة الأحماض من الأمور الهامة عند تصميم الخلطة وخلال وضع وإنضاج الخرسانة. كان الهدف الرئيسي لهذه الدراسة التحري عن إمكانية استخدام مخلفات الرماد الغازي من محطة المسيب الغازية كمادة مضافة بديلة عن السمنت لإنتاج خرسانة المساحيق الفعالة. أجريت فحوصات المقاومة والديمومة من أجل الوصول الى فهم واضح للخواص الميكانيكية لخرسانة المساحيق الفعالة والمعرضة لظروف قاسية بأعمار (28 و56) يوماً على التوالي.

أظهرت نتائج الفحوصات ان استخدام الرماد الغازي كمادة سمنتيه بديله له تأثير إيجابي على مقاومة الانضغاط والانشطار لخرسانة المساحيق الفعالة لغاية نسبة (10٪) من الاستبدال. بعد هذه النسبة لم يطرأ اي تحسن اضافي مؤثر لخواص ومقاومة الخرسانة الناتجة. كما ان تعرض خرسانة المساحيق الفعالة لدورات او تراكيز عالية من الانجماد–الذوبان ومهاجمة الاحماض يكون مصحوبا بضرر اعلى مما في حالة التراكيز والدورات الاوطأ..

الكلمات المفتاحية

مخلفات الرماد الغازي، خرسانة المساحيق الفعالة، فحوصات المقاومة والديمومة.

Abstract

The resistance of concrete to damage due to freezing-thawing and acid attack has become an increasingly important factor to be considered in both mix concrete design and its placing and curing techniques. In this study, the primary goal was to investigate whether a gasification ash GA from Al-Mussaib electrical power station can be used as a supplementary cementitious material in reactive powder concrete RPC. Strength and durability tests were conducted in order to get a good understanding of the mechanical features of concrete exposed to severe conditions at (28) and (56) days respectively.

The results of the experiments show that the use of gasification ash as a supplementary cementitious material has a positive effect on both compressive and splitting strength development of reactive powder concrete up to (10%) of replacement. Above (10%) gasification ash has no further increase in the strength of concrete. The exposure to higher cycles of freezing-thawing and larger concentrations of acid attack have higher detrimental effect than those of lower concentrations.

Keywords

Gasification ash, reactive powder concrete, strength, durability.

1. Introduction

In the last ten years, reactive powder concrete has been widely used in heavy structures as strength and durability are considered the most important factors for designers. Therefore, controlling the ingredients and surrounding environment of concrete is important to its serviceability. Moreover, it is well known that using waste materials in the manufacturing of cement based materials and concrete is an opportunity to reduce its environmental impact [1-2]. This was due to the growing knowledge of the engineering of the economic and ecological benefits that the use of waste materials have in both: cement and concrete composites [3].

In high performance concrete, a part of Portland cement is replaced by pozzolanic admixtures such as metakaolin, fly ash, etc. [4]. After that, the strength and durability of cement based composites were improved due to reducing the number and size of micro pores [5]. Further, the components of fly ash vary considerably depending upon the source of the coal being burned. Silicon dioxide (SiO_2) (both amorphous and crystalline), aluminum oxide (Al_2O_3) and calcium oxide (CaO), the main mineral compounds in coal-bearing rock [6].

Kumar et al [7], has investigated the use ash from burned wasted wood as partial replacement of cement. They mentioned that, the pozzolanic activity index was (75.9%)and it is noticed that (10 %) replacement of cement with sawdust ash shows the desired workability and strength. Abdulabbas [8], examined sustainable industrial waste materials (cement kiln dust) as partial replacement of cement. It was found that the replacement of up to (20%) (CKD) by weight of cement has a negligible effect on strength of concrete. Karthick and Nirmalkumar [9], studied the properties of controlled low strength material made using industrial waste incineration bottom ash and quarry dust. These wastes must be properly managed and disposed without causing any harmful environmental effects. Solanki Y. and Pitroda [10], studied the use of paper mill sludge ash (PA) as supplementary cementitious material. On the basis of data collected, they concluded that PA showed a positive effect on the strength of mortars if used to replace up to (10 %) of Portland cement.

It has been known that cycles of freezing and thawing had detrimental effects on the structure and durability of concrete [11]. In addition, the effects of damage due to freeze-thaw action include cracking, loss of stiffness, increased permeability and eventually scaling and spalling. The most widely accepted hypothesis for the damage caused by freezing and thawing on concrete is that proposed by Jang et al [12]. They found that water expand (9%) when it froze at (6) C. Thus, as water froze in a pores that (91%) fill of water, the resultant expansion due to ice formation forces unfrozen water to flow into the gel structure surrounding the capillaries. When the hydraulic pressure results in stresses exceeding the strength of the paste, cracks occur.

Hydrated cement paste is alkaline; therefore, exposure to acidic waters is detrimental to its mechanical properties and durability. Beulah and Prahallada [13] mentioned "concrete is susceptible to attack by sulphuric acid produced from either sewage or Sulphur dioxide present in the atmosphere of industrial cities". They concluded that, the production of a very dense and impervious concrete is the only way to inhibit the deterioration of concrete by chloride ions. Loss in mass and strength in RPC specimens kept in acidic environment were studied by acid test and visual observation on surface deterioration is also reported. It is noted that sulphuric acid reacts with calcium present in cement and gives paste of gypsum which reduces the concrete strength. It was observed that strength loss is high after immersion in acid solution (5%) of volume of water.

2. Objectives

This paper will address some of parameters in an attempt to further the understanding of acid attack and freeze-thaw phenomena in reactive powder concrete containing gasification ash as a byproduct. So, there were two major goals of this research study. The first goal was to obtain information relating to the effect of using cheap, and local byproduct (gasification ash from Al-Mussaib electrical gas station in Babylon governorate) as a supplementary cementitious material on the strength of reactive powder concrete. In particular, the effect of the added percentage of gasification ash and the age of concrete were of interest. The second goal was to provide information for use in establishing the mechanisms by which the gasification ash improves the resistance of RP concrete to freezing-thawing cycles and acid attack.

3. Materials

The materials used in this research consisted of Type I Portland cement, natural Al-Ekhaider fine aggregate, tap water, a highly efficient high-range water reducer admixture commercially known as (Sika ViscoCrete 5930), gasification ash from ALmsaeb electrical power station (the ash precipitated mechanically before the flue gases reach the chimneys from the exhausted gases of coal-fired power station) and micro Steel fibers. The chemical composition of cement and gasification ash, presented in (Table1), confirmed that cement is complying to Iraqi Specification (No. 5/1984) and the gasification ash conforms to the requirements of (ASTM C-618) class C specification with strength activity index of (105%) at (28) days following the (ASTM C-311/05) specification. In order to get a good understanding of the mechanical features of reactive powder concrete made of gasification ash, it is recommended to sieve the ash in (No. 200) (75) μm sieve.

The fine aggregate used was a quartz based sand that is complying with (B.S. 882/1992), zone F. It was tested to determine the grading and other physical and chemical properties. Results indicated that the fine aggre-

gate grading were within the requirements of the (B.S. 882/1992). For reactive powder concrete, very fine sand with maximum size (600) μm is used. This sand is separated by sieving; its grading satisfies the fine grading in accordance with the (B.S. 882/1992). The sieve analysis of the original (column 2) and the separated fine sand (column 4) is shown in Table (2).

Table (1): chemical composition of cementitious materials*.

Constituent	Cement (%)	Limits of I.Q.S No. 5/1984	Gasification Ash (%)	Limits of ASTM C-618/05
CaO	61.35	---	21.62	
SiO_2	23.59	21 ≤	42.18	% 50 ≤
Al_2O_3	5.13	6 ≥	6.81	
Fe_2O_3	2.27	6 ≥	1.52	
MgO	2.38	% 5 ≥	0.42	
SO_3	2.9	% 2.5 >	0.89	5 ≥
NaOH+KOH	0.46		/	
Loss on Ignition	2.3	% 4 ≥	1.7	% 6 ≥
Insoluble residue	0.87	% 1.5 ≥	/	
Lime Saturated factor	0.96	1.02 – 0.66	/	
Fineness	285 m^2/kg	230 ≤ Blaine	% 28	34% ≥ No.325

* Chemical tests were made by the National Center for Geological Survey and Mines.

Table (2): Properties of fine aggregates *.

Sieve size (mm)	Cumulative passing 1 (%)	Limits of B.S. 882/1992 Over all grading	Cumulative passing 2 (%)	Limits of B.S. 882/1992 fine grading
4.75	95.2	89-100	100	-

2.36	78.6	60-100	100	80-100
1.18	52.0	30-100	100	70-100
0.60	24.3	15-100	100	55-100
0.30	10.9	5-70	59	5-70
0.15	3.8	0-15	13	-
SO_3 content = 0.28 % < 0.5 % limits of I.Q.S No.45/1984				

* Tests were made by the Concrete Laboratory in Karbala Technical Institute.

The steel fibers with a diameter of (200)µm and length of (13) mm (aspect ratio lf /df =65) were provided by Sika with a tensile strength of 1280 MPa and a density of (7820)kg/m3. According to ASTM C494-05, the used Sika ViscoCrete 5930 superplasticizer is classified as type F.

4. Experimental Program.

The shown concrete mix proportions in Table (3) were selected according to that mentioned by Ali [14]. To evaluate the compressive and splitting tensile strength at 28-day and 56-day, three concrete samples were chosen in each age. When the mixer filled with materials, the mixer was run for three min., resting for two min., and followed by remixing for three min.

Compression and splitting testing is performed on concrete cylinders that having dimensions of (20*10) cm. Making and curing of cylinders were done in accordance to (ASTM C 31/03). Capping were done according to (ASTM C 617-15) specifications using (Sika Grout 214 AE) for cylinders used in compression test. Testing the cylindrical specimens was done following both (ASTM C 39/04, and ASTM C 496-04). Testing is conducted at various ages, (28 and 56) day in order to observing the strength development with age. After that, (28) days was chosen because of most of the designers use this age in calculations and to make sure that mean target strengths were gained.

Table (3): Mix proportions.

Mix No.	Cement (kg/m³)	Sand (kg/m³)	SP by w.t of cement (%)	Gasification ash by w.t of cement		w/c (%)	Steel fiber (%) V_f	Age (days)
				(%)	(kg/m³)			
M1	1100	1100	7	0	0	30	1	28 + 56
M2	1045	1100	7	5	55	30	1	
M3	990	1100	7	10	110	30	1	
M4	935	1100	7	15	165	30	1	
M5	880	1100	7	20	220	30	1	
M6	825	1100	7	25	275	30	1	

V_f = volume fraction of fibers (%) by vol. of concrete mix.

5. Durability Tests.

The freeze-thaw test was conducted in a MATEST rapid Freeze-thaw apparatus (Plate 1), which was provided with assistance from the Building and Construction Engineering Department at the University of Technology. This machine uses a freezer-plate beneath the specimen containers to cool the concrete, and electric heaters placed between the containers to warm the concrete. The rapid freeze-thaw procedure is standardized by (ASTM C666/03). The appropriate specimens were removed from the freeze-thaw machine after (25) and (50) cycles. Then, the specimens were removed during a thaw period, and stored at room temperature until testing.

Water cured specimens for (7) days were taken out and allowed to dry for three days and then the same concrete specimens were kept immersed in (2) and (4%) concentrated (according to literature) hydrochloric acid solution for (28) days for durability observation. The curing media was replaced with fresh solution at the end of every week to maintain the same concentration.

Plate (1): experimental setup: (a) freeze-thaw climatic chamber in the University of Technology.

6. Results and Discussion.

It is well known that the serviceability of any structural concrete element depend largely on its physical and mechanical properties. Further, appropriate making and curing of concrete produces a very dense mix that could resist the ingression of chemical substances and/or severe conditions. A major concern with gasification ash byproduct GA is how GA could alter the concrete properties in the hardened state. The concrete strength may be reduced or increased according to addition percent and testing age of the investigated mix.

Table(4) and Fig. (1 & 2) present the compressive strength data for all reactive powder concrete mixtures. These data show that gasification ash has a significant effect on the compressive strength of concrete mixtures up to (10%) of replacement. Free CaO can harm the volume stability and the concrete durability. The higher the GA replacement dosage the higher the CaO content. The data in Table (4) show that the (28) days compressive strengths of mixtures containing GA were larger than all other mixes except (M6) at (56) days. This enhancement was due to both pozzolanic activity and filling effect of GA in the matrix resulting in more dense and homogenous structure.

Table (4): Results of compressive strength (MPa).

Mix No.	28-day	56-day	Freezing & thawing		Acid attack	
			cycles 25	cycles 50	2 %	4 %
M1	87.3	95.2	52.8	47.6	72.6	64
M2	109.8	118.7	92	80.8	92	85.9
M3	116.7	128.4	100.4	89.1	95.4	93.5
M4	104	109.1	78.6	67.5	84	78.3
M5	96.8	99	70.9	60	76.1	65.8
M6	88.5	93.8	57.6	52.3	68.9	63.4

Results of compressive strength for (28) day specimens under freezing-thawing and acid attack confirm that dense matrix is the reason for higher residual compressive strength, as illustrated in Fig. (4 & 5). However, the control mix showed the lowest compressive strength, because it has no pozzolanic activity since no GA was added to mix. However, the residual strength for all mixes after being subjected to accelerated durability tests still higher than the minimum value (55) MPa for high strength concrete according

to (ACI 363.2R-98) except (M6) subjected to (50) cycles of freezing and thawing.

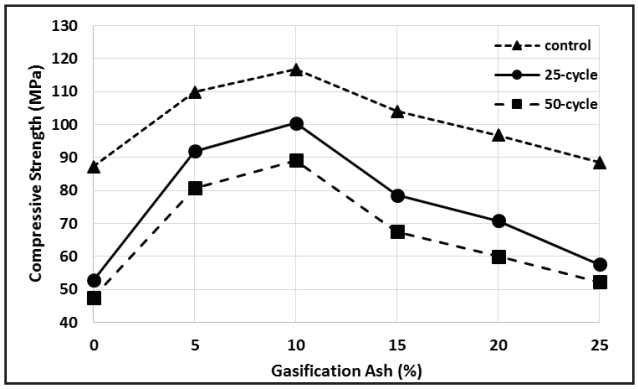

Fig. (1): Effect of gasification ash on compressive strength for (28) days samples exposed to freezing and thawing.

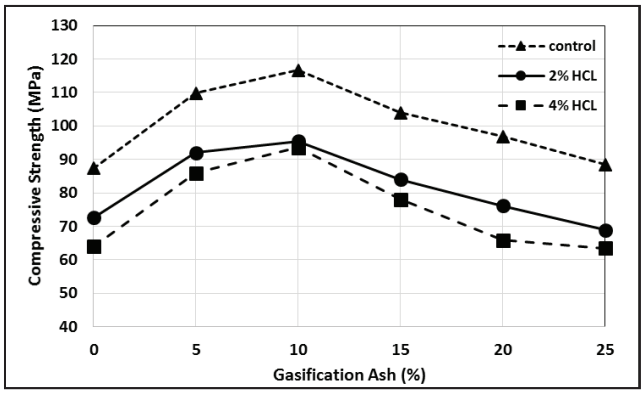

Fig.(2): Effect of gasification ash on compressive strength for (28) days samples exposed to acid attack.

After undergoing (25) cycles and then (50) cycles of accelerated aging of exposure to the environment of the freeze-thaw and (2%), (4%) HCl of acid attack, it was observed that saturated samples made with GA byproduct had higher strength values than control samples. This in agreement with [11 and 12], shows that the reactive powder concrete that contain GA byproduct is more suitable for use in hazard environments than that of control due to the filling effect of GA. Internal micro cracking without surface scaling, followed by loss in compressive strength of (14-39%) after (25) cycles and (23-50%) after (50) cycles of freezing and thawing were the main pronounced actions due to freezing and thawing.

The (28) days splitting tensile strength values for all batches are presented in Table (5) and Fig. (3 to 4). As in the case with concrete compressive strength, splitting tensile strength is heavily dependent on cementitious content and may be affected by dosing fresh concrete with GA byproduct. Data presented in Table (5) and Fig. (3 to 4) show that the splitting tensile strengths for mixtures containing GA were greater in all cases than control mix except for M6 at (28 and 56) days. Although, the variations between the reference and the GA samples are not high in most of the studied cases. As it expected, the (50) cycles of freezing-thawing exposure had the lower strength as compared to control. This is the same for (4%) concentration of HCl solution. This trend is similar to that found by Karthick M. and Nirmalkumar K [9].

Table (5): Results of splitting tensile strength (MPa).

Mix No.	28-days	56-days	Freezing & thawing		Acid attack	
			cycles 25	cycles 50	% 2	% 4
M1	9.2	9.6	4.8	3.5	3.7	3.4
M2	10.5	12.1	5.2	4.8	4.1	3.9
M3	12.2	13.4	6.3	5.9	5.3	5.4
M4	10.5	11.1	5.6	4.3	4.4	4.1
M5	9.2	9.5	4.9	3.9	3.1	2.8
M6	9.1	9.4	4.2	2.8	2.9	2.6

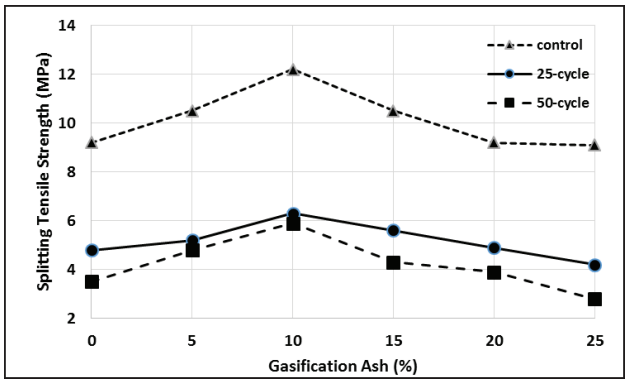

Fig.(3): Effect of gasification ash on splitting tensile strength for (28) days samples exposed to freezing and thawing.

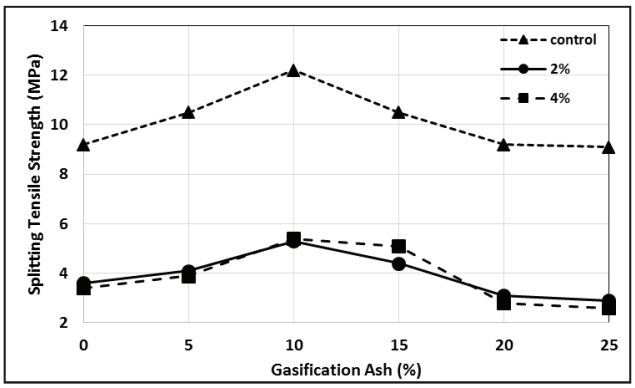

Fig.(4): Effect of gasification ash on splitting tensile strength for 28-days samples exposed to acid attack.

7. Conclusions.

Based on the analysis of data compiled throughout this research, the conclusions are summarized as follows: -

1. All mixes that contain GA byproduct had higher values of compressive and splitting strengths than that of control, which demonstrates that the GA byproduct could be used as supplementary cementitious material of not more than (10 %) of addition.
2. The inclusion of gasification ash into the RPC resulted in a good durability performance under the action of acid attack and freeze-thaw cycle.
3. Distress due to freezing and thawing action manifest in internal micro cracking without surface scaling, followed by loss in compressive strength of (14-39%) after (25) cycles and (23-50%) after 50 cycles of freezing and thawing.

4. Splitting tensile strength of RPC specimens experienced a maximum loss of about)68%(and (71%) due to exposure to (2%) HCl and (4%) HCl of acid attack respectively. However, this loss was not exceed (54%) and (59%) after the exposure to (25 and 50) cycles of freezing and thawing.

5. The deference in the strength development at (28 and 56) days lies between (3-10%) for all cases. This proves that (90%) of the ultimate strength of RPC gained at (28) days.

6. The exposure to high concentrations (i.e. 4 % HCl) have higher detrimental effect than those of lower concentrations.

References

[1] Bashandy A., "Influence of Elevated Temperatures on the Behavior of Economical Reactive Powder Concrete", Journal of Civil Engineering Research, Faculty of Engineering, Menoufiya University, Egypt, 3(3): 89-97, (2013).

[2] Kalifa H., Yahya O., Mohsen Y., "Effect of Calcined and Non Calcined Fly Ash Addition on The Strength of Concrete", Journal of Kerbala University, Vol. 13 No.1 Scientific. pp. 141-148, (2015).

[3] El-Louh O., "Fresh and Hardened Properties of Locally Produced Reactive Powder Concrete", Master degree thesis, The Islamic University Gaza, Civil Engineering Department, pp. 26, (2014).

[4] Kadhum M., "Studying of Some Mechanical Properties of Reactive Powder Concrete Using Local Materials", Journal of Engineering, Number 7, Volume 21, July pp. 113-135, (2015).

[5] Hassan M., "SEM-Backscattered Imaging analysis of Cementitious Composite Matrix Incorporating Mineral Admixture", Eng. &Tech. Journal, Vol. 32, Part (B), No.4, pp. 696-703, (2014).

[6] Agharde A. and Bhalchandra S., "Mechanical properties of reactive powder concrete by using fly ash", International Journal of Advanced Technology in Engineering and Science, Volume No.03, Issue No.01, January, pp. 603-608, (2015).

[7] Kumar M., Bivera B., Babu P. and Janagan S., "Effect of mineral admixtures on strength & durability of reactive powder concrete", Singaporean Journal of Scientific Research, Issue of International Journal of Applied Sciences, Vol.8, No.1, pp.58-70, (2016).

[8] Abdulabbas Z. "Utilization of Cement Kiln Dust in Concrete Manufacturing", Jordan Journal of Civil Engineering, Volume 7, No. 1, pp. 111-125, (2013).

[9] Karthick M. and Nirmalkumar K., "Durability Properties of High Strength Self Compacting Concrete using Silica Fume and Quarry Dust", International Journal of Scientific Engineering and Applied Science, Volume-2, Issue-4, April pp. 389-395, (2016).

[10] Solanki Y. and Pitroda J., "Investigation of Low Cost Concrete Using Industrial Waste as Supplementary Cementitious Materials", International Journal of Engineering Science and Innovative Technology, Volume 2, Issue 1, January pp. 81-88, (2013).

[11] Lee M., Lee G., Huang Y., and Lee K., "UHPC Precast Concrete under Severe Freeze-Thaw Conditions", International Journal of Engineering and Technology, Vol. 5, No. 4, August pp. 452-456, (2013).

[12] Jang S., Rokugo K., Park W. and Yun H., "Influence of Rapid Freeze-Thaw Cycling on the Mechanical Properties of Sustainable Strain-Hardening Cement Composite (2SHCC)", Materials Journal No.7, pp. 1422-1440,(2014).

[13] Beulah M., and Prahallada M. C.," Effect of Replacement of Cement by Metakaolin On the Properties of High Performance Concrete Subjected to Hydrochloric Acid Attack",

International Journal of Engineering Research and Applications, Vol. 2, Issue 6, November-December pp. 33-38, (2012).

[14] Ali I., "Optimal Strength Design of Reactive Powder Concrete", International Journal of Technical Research and Applications, Volume 5, Issue 1, pp. 5-12, (2017).

Density Functional Theory Calculations of Electronic Structure for Aluminum Metal Complexes

*Faeq A. AL-Temimei
**Hamid I. Abbood
* Physics department, College of Science, University of Kufa, Iraq
**Physics department, College of Science, University of Babylon, Iraq.

Received Date: 12 / 2 / 2018
Accepted Date: 15 / 6 / 2018

الخلاصة

التركيب الالكتروني لثلاثة معقدات معدنية مقترحة للألمنيوم تم اجراء الاسترخاء لها باستخدام الدالة الهجينة ذات المعاملات الثلاث (B3LYP) مع دالة أساس. حيث تم حساب الخواص الالكترونية والطاقات لكل معقد. اما طاقات التهيج للمعقد المعدني تمت باستخدام طريقة TD-DFT/B3LYP مع دالة الاساس SDD. ان طاقة اعلى مدار جزيئي مشغول وطاقة أدنى مدار جزيئي غير مشغول، وفجوة الطاقة، الصلابة والمرونة حسبت ليتم التنبؤ بالفعالية الكيميائية لكل معقد. النتائج التي تم الحصول عليها تبين ان معقدات الالمنيوم المعدنية تلعب دور مهم ومؤثر كمحفزات في التفاعلات الكيميائية مثل تفاعلات البلمرة.

الكلمات المفتاحية

معقد الالمنيوم المعدني، B3LYP، دالة الاساس SDD، طيف الاشعة الفوق البنفسجية المرئي.

Abstract

Electronic structures of three suggested aluminum metal complexes are relax using SDD-B3LYP/DFT method. The structural parameters and energies were calculated for each complex. The excitation energy of the complex was obtained by using the TD-DFT/B3LYP method with SDD basis sets. EHOMO, ELUMO and LUMO-HOMO energy gap, global hardness and softness were calculated to predict the chemical activity of the complexes. That results showed the aluminum metal complexes play a significant rule such as catalysts in many chemical reactions as in polymerization processes.

Keywords

Aluminum metal complex, B3LYP, SDD basis set, UV-Vis spectrum.

1. Introduction.

The metal complex compound is a structure consisting of a central metal atom or ion, in which metal is usually attached to a surrounding array by several atoms, ions or molecules, each of which is called a ligand [1]. The atom within a ligand that is bonded to the central metal atom or ion is called the donor atom and bound to the central atom by a coordinate covalent bond into an empty metal orbital. In a metal complex, a metal ion is bonded to a number of donor atoms, which can be a different or a same [2].

The electron density on the the center of molecular (metal) and the physical surroundings around the metal is affected by each ligand present in complex compound. The electronic structure can be described by a relatively ionic model that comes from electrons of the metals and ligands in metal complexes. The properties of metal complex compounds are determined by the electronic structure of molecular compounds [3, 4]. Metal complexes exhibit changed characteristic properties which depend on the nature of metal and the method arrangement of the ligand to which they are bound [5, 6].

The Ziegler-Natta catalysts, entitled after the chemists Ziegler and Natta (1955), is a catalyst used in the synthesis of polymers[7]. The Ziegler-Natta catalysts is a generic term to describe a variety of catalysts based on transition metal moieties, which are active in α-olefins polymerization and copolymerization. The Ziegler-Natta catalysts is produced from reaction between compounds of transition metal and compounds such as the hydrides or alkyls groups [7-9].

A catalyst such as Z-N catalyst is used to decrease the activation energy for the polymerization process thus speeding up the chemical reaction and allowing it to proceed even under mild conditions. The catalysts fundamentally increase a chemical reaction, it increases the chemical reaction rate without being consumed itself [6, 8].

The finding of Ziegler-Natta catalysts presented a new dimension to the domain of polymers. The Ziegler-Natta catalysts added to the development of the long chain polymers of hydrocarbons and produce various commercial polymers such as polypropylene and polyethylene. These polymers are advantageous in the construction of films, plastics and fibers. Application of Ziegler-Natta catalysts trend clearly reflects the care specified to this area both in researches, academic and industrial laboratories in the world [6, 7, 9]. In this study design new aluminum metal complex compounds (1, 2 and 3 molecular in Fig. 1) represented catalysts moleculars such as catalysts Ziegler-Natta and have various applications in many chemical reactions as in polymerization processes.

2. Theory.

The initial structures of the complexes were designed and drawn at Gauss View (5.0.8) program [10]. The calculations were carried out by using Gaussian (09) package of

programs [11]. The studied aluminum metal complexes were fully relax by employing B3LYP-SDD/DFT (52). B3LYP combination of exchange and correlation functional [12,13] in DFT is applied to all calculations of the electronic structure. The electronic excitation energy was calculated for the relaxed aluminum metal complexes by employing TD-DFT/B3LYP method with SDD basis sets. TD-DFT with SDD basis sets has been proved to be depend for calculating the electronic structure of heavy transition metals [14-16].

3. Results and Discussion.

The structures of the suggested aluminum metal complexes in Fig. (1) are relax by employing the SDD-B3LYP/DFT method. Table (1) states the results of the optimized parameters (bonds in Angstroms and angles in degrees) for the aluminum metal complexes. The coordination of the molecules after the relaxation showed a suitable method we used with the SDD basis sets where the calculated bonds are in good agreements with the experimental data [4,17]. The theoretical values of Al-O bonds in complex (2) are agree with the results in [17]. Al-O bonds are change depending on the coordination of the complex and the position of the central aluminum metal. The bonds C-C are varied depending on the coordination for each complex and their values are in good agreements with those in open and cyclic carbon compounds. From Table (1) shows that Al-Cl bond in complex (2) is (2.24000) A° and complex (3) is (2.20107-3.09606) A° these value are in good agreement with the results of metal complexes [17,18].

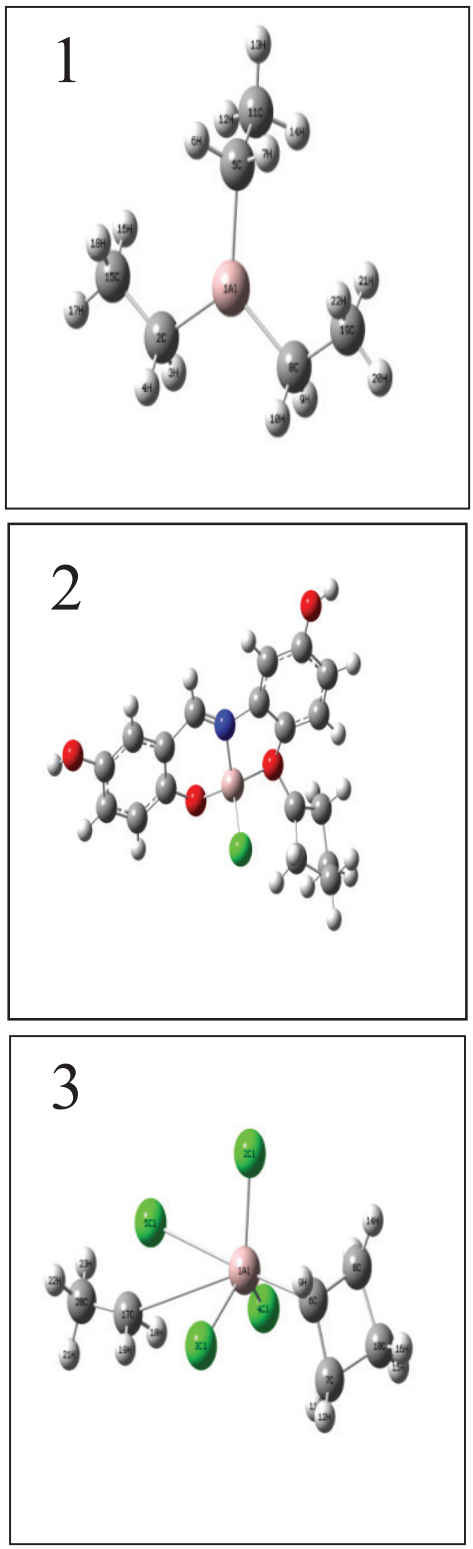

Fig. (1): The relax structures of aluminum metal complexes.

Table (1): The optimized parameters of the aluminum metal complexes.

Aluminum Metal Complex	Bond length (A°)		Bond angle (deg.)	
	Bond	Value	Bond angle	Value
1	Al-C	2.02000	H-C-H	109.47122-109.47125
	C-C	1.54000	C-Al-C	120.000
	C-H	1.07000	C-C-Al	109.47120- 109.4712
2	Al-Cl	2.24000	Cl-Al-O	108.95937-111.87067
	Al-N	1.81545	O-Al-N	96.17055-109.54072
	Al-O	1.86576-1.86592	C-N-Al	103.69243-120.10640
	C-C	1.40272-1.58807	C-O-Al	105.22779
	O-C	1.43000-1.45923	C-C-C	101.51277-118.09572
	H-C	1.07000	H-C-N	120.63898
	H-O	0.96000	H-C-C	114.19864-119.43061
	N-C	1.27681-1.48400	H-C-H	108.31531
			H-O-C	109.47122
			C-C-O	116.70290-126.34110
3	Al-Cl	2.20107-3.09606	Cl-Al-Cl	83.52799-120.23120
	Al-C	2.29878-3.95960	C-Al-Cl	28.35233-71.67279
	C-C	1.52184-1.53632	H-C-Al	75.18740-89.07055
	H-C	1.09066-1.09406	H-C-H	109.10634-111.04073
			H-C-C	113.83217-114.77388
			C-C-Al	113.56426-159.58647
			C-C-C	85.85701-93.60788

Table (2) declare the results of High Occupied Molecular Orbital Energy E_{HOMO}, Low Unoccupied Molecular Orbital Energy E_{LUMO} and LUMO-HOMO Energy gap E_g for the studied aluminum metal complexes from the SDD-B3LYP/DFT calculations at the minima energy. As shown, for each complex the LUMO energy is greater than HOMO energy. Complex (2) has the highest values of E_{LUMO} and E_{HOMO}. High values of LUMO energy means low ability of complex to accepting an electron. Therefore, the order of complexes to acceptance an electron and become anions is as: 3 > 1 > 2. Also, we noted from Table (2) the highest bond (Al-C) found in compound 3 and the highest bond (Al-Cl) in compound 3. In addition, the highest angle in this compounds were found in compound 1 according to the position of atoms in metal complexes.

Low value of HOMO for complex means high energy that complex required to donating an electron. Therefore, the order of complexes to donating an electron and become cation is as: 2 > 1 > 3.

The LUMO-HOMO energy gap (Eg) values in Table (2) showed the suggested aluminum metal complexes have Eg between (2.8) eV for complex (2) and (5.88) eV for complex1, means these aluminum metal complexes have varying electronic applications such as catalyst in polymers process. The lowest Eg is (2.8) eV for complex (2) refers to that this complex has a suitable semiconducting electronic applications. Fig. (2) declare the LUMO-HOMO energy gap of the studied complexes. Also we noted from Table (2) that the complexes (1) and (3) needed higher energy to exaction the electrons from level to other comparing with complex (2) according to energy gab (Eg).

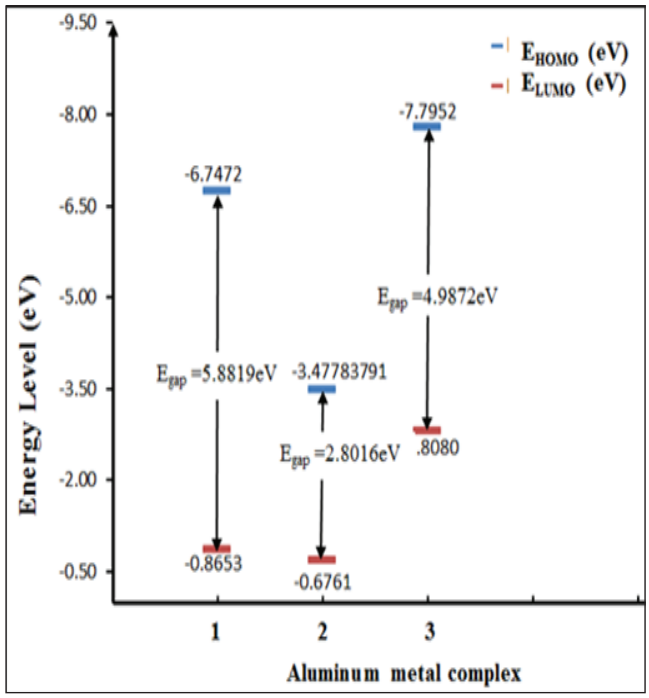

Fig. (2): LUMO-HOMO energy gap of metal complexes.

We noted from Fig. (2) and Table (2) the compound 1 has large energy gab this mean this compound can be using in chemical reactions applicatins as in polymerization isolated processes. Also, we noted that metal complexes (1) gives the highest Eg as shown from Table (2). This may relate to the highest angle obtained for complexes (1) in Table (1).

Table (2): The E_{HOMO}, E_{LUMO} and E_g for aluminum metal complex.

Aluminum Metal Complex	E_{HOMO} (eV)	E_{LUMO} (eV)	E_g (eV)
1	-6.7472	-0.8653	5.8819
2	-3.4778	-0.6762	2.8016
3	-7.7953	-2.8080	4.9872

Fig. (3) illustrates the 3-D distribution of HOMO and LUMO energies of the aluminum metal complexes. $HOMO_s$ and $LUMO_s$ are molecular orbitals building according to linear combination atomic orbitals-molecular orbitals $LCAO^s$-MO^s theory. Each MO constructs due to charge distribution in the complex, and therefore, the atomic charge density population in the metal and the ligands in the complex. The difference of the HOMO and LUMO distribution of the aluminum metal complexes in Fig. (3) refers to more differences in molecular polarizabilities and electronic structures of these complexes, and therefore, differences in chemically reactivity for the complexes as catalysts.

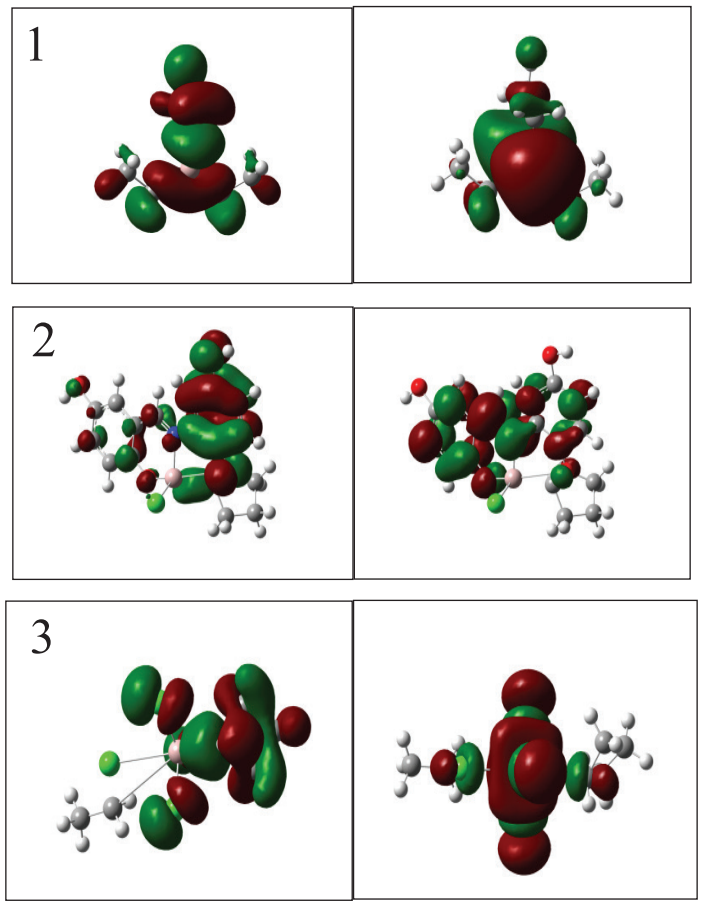

Fig. (3): 3-D HOMO (Left) and LUMO(Right) distribution of the complexes.

The electrostatic potential (ESP) surfaces distribution of aluminum metal complexes calculated from the total self-consistent field SCF and shown in Fig. (4). In complex 1, the ESP surface was approximately drag uniformly in space of the complex towards the three ligand groups connected to the central aluminum metal. In complex (2), the ESP surface were dragged towards the chlorine and oxygen atoms due to their high electronegativity in comparison with hydrogen and carbon atoms. In complexes 3, the ESP surface were approximately dragged towards the chlorine atoms only. These results means that the determination of the active areas of the ESP for these complexes to play an important factor as catalysts in many chemical reactions as in polymerization processes.

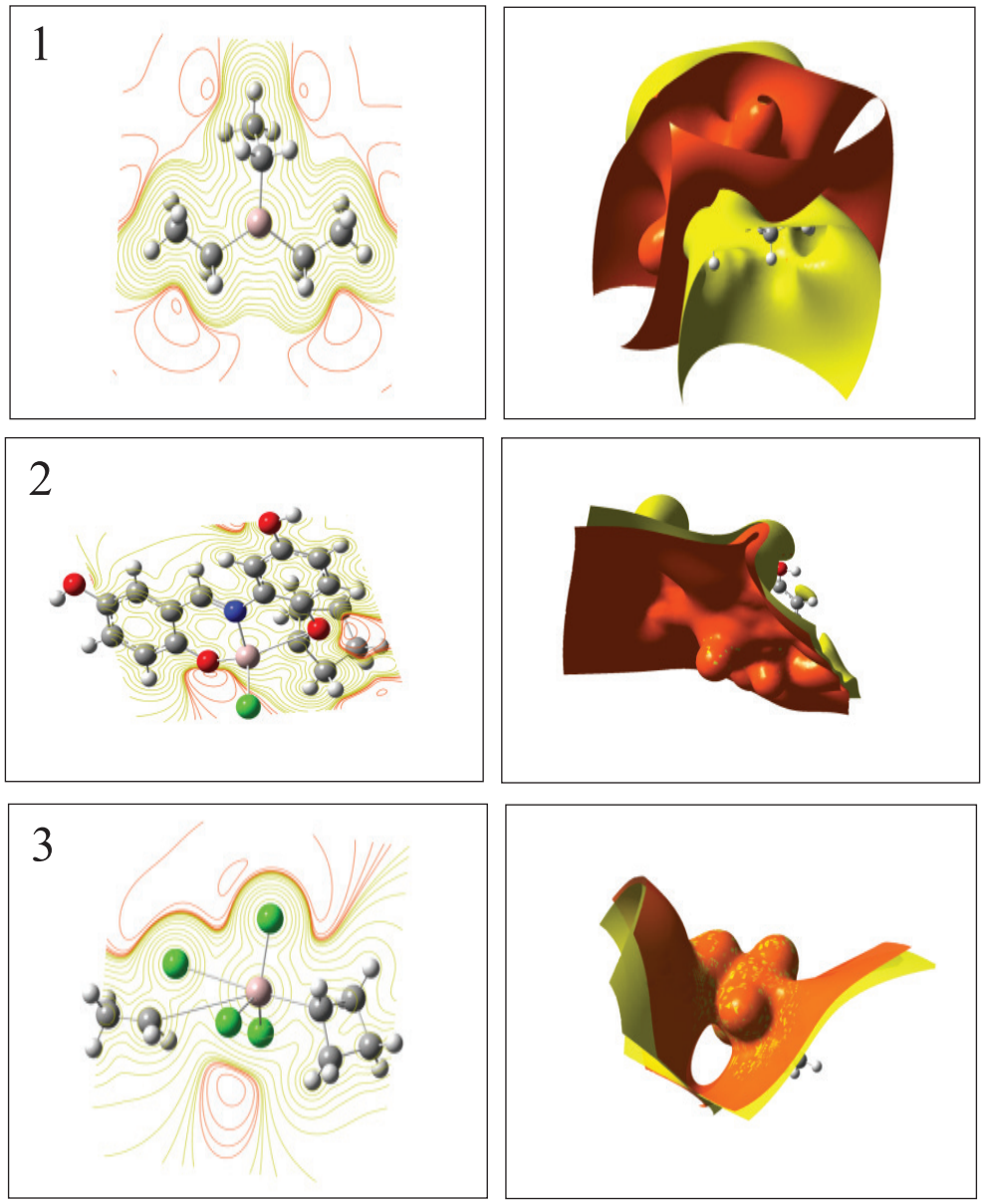

Fig. (4): The 2-D counter (Left) and 3-D (Right)ESP distribution of the complexes.

Table (3) lists the results of global hardness and softness as quantum chemical parameters. The computation of molecules properties (hardness and softness) are carried out by Koopmans theorem (KT) [4] as shown in the following:

Here H indicates the hardness, is the ionization potential, is the electron affinity and S denoted the softness.

As can be seen, the trend of the quantum chemical parameters depend on the coordination and the molecular geometry of each complex. The coordination tendencies of complexes as catalysts can be discussed with the global hardness and softness. Soft complexes have small energy gap and therefore, small excitation energies required for electron transfer. Hard complexes have large energy gap and more complex to interact with other species. Approximately, all studied aluminum metal complexes have low values of H and S, they are weak in electron transfer, therefore, they can work catalysts for chemical reactions.

Table (3): Quantum chemical parameters for aluminum metal complexes.

Aluminum metal complexes	1	2	3
Hardness (eV)	2.9410	1.4008	2.4936
Softness $(eV)^{-1}$	0.1700	0.3569	0.2005

As shown previously, the energy gap of the studied aluminum metal complexes was varied from (2.8) eV for complex (2) to (5.88) eV for complex 1. Know, the behavior of excitation energies of the studied complexes that are analyzed in the B3LYP-SDD/TD-DFT. Table (4) illustrates the wavelength of excitation energies for the main band, oscillator strength, electronic transitions HOMO-LUMO and the state for the aluminum metal complexes.

Fig. (5) declare the Ultraviolet-Visible (UV-Vis.) spectra of the studied complexes. As seen, complex 1 have one peak of excitation energy at (356.17) nm wavelength with full transition between the frontier orbitals HOMO→LUMO. Two peaks of excitation energy were observed for complex (2) at (333.33) nm and (459.82) nm with two main electronic transitions H-5→LUMO and H-4→LUMO. Complex C exhibits one peak of excitation energy at (362.56) nm with many electronic states in the doublet.

Table (4): UV-Vis results of aluminum metal complexes.

Complex	Wavelength (nm)	Oscillator Strength	Electronic Transition HOMO→LUMO	State
1	356.17	0.0047	HOMO→LUMO (99%)	Singlet
2	333.33	0.2944	H-5→LUMO (79%) H-4→LUMO (16%)	Singlet
	459.82	0.1147	H-1→LUMO (95%) HOMO→LUMO (3%)	
3	362.56	0.0823	H-13(α) →LUMO(α) (21%) H-11(α) →LUMO(α) (12%) H-10(β) →L+1(β) (33%) H-15(α) →LUMO(α) (4%) H-14(α) →LUMO(α) (6%) H-10(α) →LUMO(α) (2%) H-11(β) →L+1(β) (6%) H-9(β) →L+1(β) (6%)	Doublet

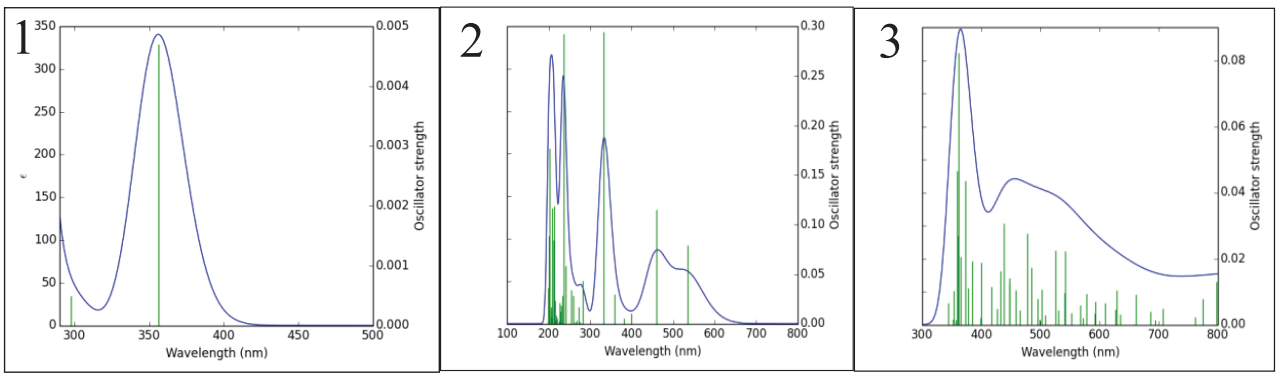

Fig. (5): UV-Vis Spectra of aluminum metal complexes.

86.09, 125.64)

The results of molecular polarizability for complexes (1,2 and 3) showed the catalyst (1) has low dipole momentum (D.M) (0.137) Debye, catalyst (2) has large D.M (8. 119) Debye and catalyst (3) has D.M of (3.979) Debye, means complex (1) has the highest symmetry in comparison with the others while complex (2) has very low symmetry and this due the coordination of each catalyst. From the results, the studied aluminum metal complexes have large values of molecular polarizability (101.72, 86.09, 125.64) a. u, respectively, and therefore, they have high ability to interact with other molecules. Aluminum metal complexes play a significant role in chemical reactions as catalysts and all compounds in this study represented Ziegler-Natta catalysts according to the results and it properties.

4. Conclusions:

1. Aluminum metal complexes have different electronic applications due to different values of LUMO-HOMO energy gap obtained.

2. The differences of HOMO and LUMO distribution and ESP distribution of the complexes refer to more differences in molecular polarizabilities and electronic structures of these complexes and therefore, differences in chemically reactivity as catalysts.

3. Aluminum metal complexes play a significant influence as catalysts in many chemical reactions as in polymerization processes.

4. Approximately all studied aluminum metal complexes have low values of global hardness and softness, they are all weak in electron transfer and can be used as catalysts in chemical reactions.

5. The results of UV-Vis spectra declare the studied aluminum metal complexes have various applications such as Ziegler-Natta catalysts.

References:

[1] F. Albert Cotton and G. Wilkinson, Third Edition, John and Wiley Inc., New York, (1972).
[2] A. Geoffrey Lawrance, A John Wiley and Sons, Ltd., New Delhi, India, (2010).
[3] D. Tzelia and A. Mavridis, The Journal of Chemical Physics, Vol. 128, pp. 1-14, (2008).
[4] R. Pandey, B. K. Rao, P. Jena and M. Alvarez Blanco, Journal of American Chemical Society, Vol. 123, pp. 3799-3808, (2001).
[5] G. Neil Connelly, T. Damhus, M. Richard Hartshorn and T. Alan Hutton, U P a C Recommendations, International Union of Pure and Applied Chemistry, (2005).
[6] L. Gary Miessler, Paul J. Fischer and A. Donald Tarr, Fifth Edition, Library of Congress Cataloging-in-Publication Data, (2014).
[7] K. Vassilev, S. Turmanova, E. Ivanova and V. Trifonova, Journal of Biomaterials and Nanobiotechnology, Vol. 4, pp. 28-36, (2013).
[8] C. Athanassios Tsipis, Coordination Chemistry Reviews, Vol. 272, pp. 1-29, (2014).
[9] K. M. Bichinho, G. P. Pires, J. H. Santos, M. M. Camargo Forte and C. R. Wolf, Journal Analytica Chimica Acta, Vol. 512, pp. 359-367, (2004).
[10] Gauss View 5.0, Gaussian Inc. Wallingford, CT, USA, (2009).
[11] Gaussian 09, rev. A-02, Gaussian Inc. Wallingford, CT, USA, (2009).
[12] Hay P.J. and Wadt W.R., The Journal of Chemical Physics, 82, 270, pp.134-145, (1985).
[13] A. D. Becke and J. Chem. Phys., 98, 5648, pp.27-

39, (1993).
[14] C. Lee, W. Yang and R. G. Parr, Phys. Rev. B, 37, 785, pp. 56-69, (1988).
[15] T. Liu, H. X. Zhang and B. H. Xia, J. Phys. Chem. A, 111, 8724, pp. 121-134, (2007).
[16] X. Zhou, H. X. Zhang, Q. J. Pan, B. H. Xia and A. C. Tang, J. Phys. Chem. A, 109, 8809, pp. 49-63, 2005.
[17] X. Zhou, A. M. Ren and J. K. Feng and J. Organomet. Chem., 690, 338, pp. 131-143, (2005).
[18] A. Faeq Mohammed and I. Hamid Abbood, International Journal of Advanced Engineering Research and Science, Vol. 4, pp.82-86, (2017).

Study The Bulk Density, Open Porosity and Coefficient of Thermal Conductivity of Refractory Mortar Contains Kaolin-Metakolin-Fire Brick Powder-SiC

*Harith Ibrahem Jaaffer
**Hani mahmood hussien
*Department of Physics, College of Sciences, University of Baghdad, Baghdad, Iraq.
**Department of Science, College of Basic Education, University of Babylon, Hilla, Iraq.

Received Date: 28 / 3 / 2018
Accepted Date: 12 / 4 / 2018

الخلاصة

يتضمن هذا البحث استخدام مادة خام اقتصادية متوفرة في العراق وهي الكاؤولين(kaolin)، والتي تتوفر في الصحراء الغربية من العراق، حيث ان تشخيص تأثير بعض الإضافات على خواص الكاؤولين يفتح الافاق للاستفادة منه في التطبيقات الصناعية المستقبلية للبلد. تم تحضير عينات من (٪90) (٪70كاؤولين + ٪30 ميتاكاؤولين) مع استخدام نوعين من الإضافات وهي مسحوق كاربيد السليكون (SiC) والنوع الثاني من الإضافات هو مسحوق الطابوق الناري(FBP) والذي تم تحضيره من مخلفات البطانة الحرارية للأفران الحرارية. حرقت العينات بدرجات حرارة (1100)، (1200)، (1300)، (1400) و(1500) م^0. عدة خواص تم دراستها خلال هذا البحث مثل الكثافة الحجمية والمسامية المفتوحة ومعامل التوصيل الحراري، حيث وجد إن زيادة درجة حرارة التلبيد تزيد من الكثافة الحجمية ومعامل التوصيل الحراري وتتناقص المسامية المفتوحة. وجد ان الإضافة (٪10) من مسحوق كاربيد السليكون تزيد من معامل التوصيل الحراري والمسامية المفتوحة وتقلل من الكثافة الحجمية. اما العينات المحتوية على5%SiC+5%HBP تكون ذات خواصها المدروسة بحالة متوسطة بين (٪10) مسحوق كاربيد السليكون و(٪10) مسحوق الطابوق الناري. في حين العينات المحتوية على (٪10) مسحوق الطابوق الناري لها اقل مسامية مفتوحة ومعامل توصيل حراري وكان لها أكبر كثافة حجمية.

الكلمات المفتاحية

كاؤولين عراقي، مسحوق طابوق ناري، كاربيد السليكون، مسامية مفتوحة، كثافة حجمية، معامل التوصيل الحراري.

Abstract

This study includes the use of economic raw material available in Iraq, which is available in the Western Desert of Iraq, where the knowledge of the effect of some additives on the properties of the Iraqi kaolin allows for use in the future industrial applications for the country. The samples were prepared from (90%,70%Kaolin+30% meta kaolin) with two types of additives, the first type is the powder of silicon carbide(SiC) and the second type of additives is the fire brick powder(FBP) which was prepared from the wastes of the furnace linings. The samples were fired at the temperature of (1100), (1200), (1300), (1400) and (1500) C^{o} and several properties were studied such as bulk density, open porosity and coefficient of thermal conductivity. The addition of (10%) silicon increases the thermal conductivity and open porosity coefficient and reduces the bulk density, while the addition of (5%SiC + 5%FBP) have an intermediate property between (10%) Silicon powder and (10%) FBP. While samples contain (10%) FBP have lower open porosity and coefficient of thermal conductivity with larger bulk density.

Keywords

Iraqi kaolin, fire brick powder, SiC, bulk density, open porosity, coefficient of thermal conductivity.

1.Introduction

Refractory are materials, mostly non-metallic minerals that have enormous heat capacities and can withstand high temperatures, refractory materials are used in various fields and different aspects of the scientific life process and industrial plants such as lining furnaces, reactors and others [1]. Therefore, according to the working conditions and application of these materials, refractories must possess certain characteristics that enable them to have a long life, they must have a good thermal shock, corrosion resistance and have a specific value for thermal conductivity and thermal expansion coefficient [2]. Many types of refractories are often used in various basic metal industries such as in the process of making steel [3]. The requirements for refractories vary according to industrial application e.g., the properties of refractories used in the aluminum metal industry may be different from those used in the steel industry [4]. The clay minerals are considered to be important industrial raw materials which used in many industrial and scientific applications, such as ceramics, paper industry, petroleum industry, catalysts, etc. [5]. The field of application of the clays is closely related to its general characteristics. Therefore, studying and diagnosing the nature of industrial clays helps in determining the best exploitation, thus providing greater opportunities to benefit from the various modern applications [6]. Many studies have dealt with different and varied aspects of clay properties. Al-Nasrawy *et al*. [7] investigated the effect of different percentage addition of α-SiC powder on the physical and mechanical properties of Iraqi kaolin, where they made sample consist of SiC with additions from different percentages of Iraqi kaolin, they found that the physical and mechanical properties of the samples fired at (1400) ^{o}C changed with the addition of added kaolin. Iyasara *et al.* [8] examined the possibility of improving the physical properties of dense refractory bricks (reducing shrinkage, pores and increased corrosion resistance) of the local clay with grog addition, where they found that the increase in the percentage of grog resulted in decreased shrinkage and density, through their findings they concluded that the use of (% 30) grog led to get optimal apparent porosity of (% 20.22) and cold crushing strength of (61.77) MPa. Amkpa *et al*. [9] found that the firing temperature (1200) ^{O}C was better for mechanical, chemical and physical properties, the optimum values for porosity was (24.52%), the compressive strength was (15.37) MPa and bulk density was (1.8) g/cm^3. Also Bwayo and Obwoya[10] studied the effect of particle size of a mixture of ball clay, kaolin, and sawdust on thermal conductivity and diffusivity of ceramic bricks through preparing samples fired at (950) ^{O}C, they found that coefficient of thermal conductivity decreased with increased particle size of kaolin and ball clay. The objective of the present study is to characterize the effect of SiC and FBP on the open porosity, bulk density and coefficient of thermal conductivity of refractory mortar prepared from Iraqi kaolin.

2.Experimental Part

2.1. Raw materials

The raw materials used in this research are Iraqi kaolin, powder of silicon carbide(SiC) and fire brick powder (FBP). FBP was obtained from the grinding of waste lining furnace. Iraqi kaolin was laboratory milled into powder of particle size of (4.299) μm and particle size distribution given in Fig. (1). The particle size measurement were done by using Bettersize (2000) laser particle size analyzer. Metakaolin powder(MK) was fabricated by heating Iraqi kaolin at (800) C^o for an hour. Metakaolin powder was identified from disappearance of the kaolinte peaks in XRD pattern. Metakaolin has particle size of (7.067) μm and the particle size distribution is shown in Fig. (2). Silicon carbide is the first type of additives which has a particle size of (69.81) μm and particle size distribution is shown in Fig. (3). While firebrick powder (FBP) is the second type of additives. It has a particle size of (97.08) μm and particle size distribution is shown in Fig.(4).

2.2. Sample preparation

The best conditions were chosen in terms of the percentage of water added (solid/ water =1.5) and the binding material sodium silicate (4) g. The ratio of metakaolin added to kaolin was (30%), in other words, the main mixture consists of (70% Kaolin+30%) meta kaolin. So that the samples after drying had no cracks and have the largest values of bulk density and compressive strength.

Table (1) shows the weight ratios of prepared mixtures. The ingredients were mixed with an electrical mixer where the amount of binding material was (4) g of sodium silicate, the water quantity was (100) g and the total solid powder was (150) g. The powders are then weighed and mixed with water (but manually mixed for (5) minutes before that), then powders were added to water gradually and continue mixing for (2) hours. After finishing the mixing process, the mixture put in lubricated wooden molds, leave for a week and be removed from the molds, then placed in the oven and gradually rise to (110) ° C and remain for (24) hours. Samples were fired by an electric furnace at (1100), (1200), (1300), (1400), and (1500) °C with a sintering rate of (3) C^o / min with a soaking time of one hour.

Table (1): The sample compositing of different additives and firing temperature.

Matrix(70%kaolin+30%metakaolin) wt%	SiC wt%	FBP wt%	Firing temperature ^oC
90	١٠	0	1100
			1200
			1300
			1400
			1500

90	5	5	1100
			1200
			1300
			1400
			1500
90	0	10	1100
			1200
			1300
			1400
			1500

2.3. Physical Measurement

2.3.1 bulk density

It is calculated by using the Equation [11]:

$$BD = W_1/(V_1-V_2),$$

where BD: bulk density, g/cm^3

W_1: Dried weight, g;

V_1: Soaked weight, cm^3;

V_2: Suspended weight, cm^3.

2.3.2 Apparent porosity

It is calculated from Equation [11]:

$$AP= (W-D)/(W-S)*100,$$

where *AP*: Apparent porosity, %; *W:* Suspended weight, g; D*:* Dry weight, g;

S: Soaked weight, g.

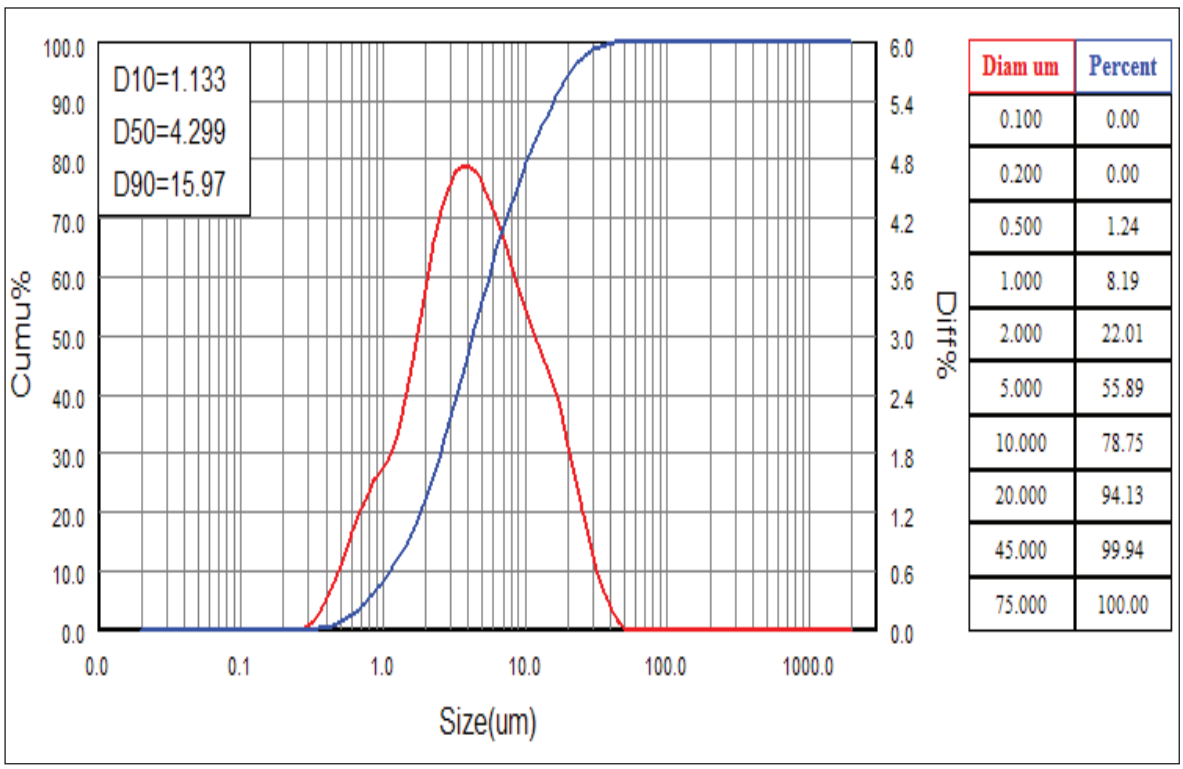

Diam um	Percent
0.100	0.00
0.200	0.00
0.500	1.24
1.000	8.19
2.000	22.01
5.000	55.89
10.000	78.75
20.000	94.13
45.000	99.94
75.000	100.00

Fig. (1): particle size distribution of Iraqi kaolin.

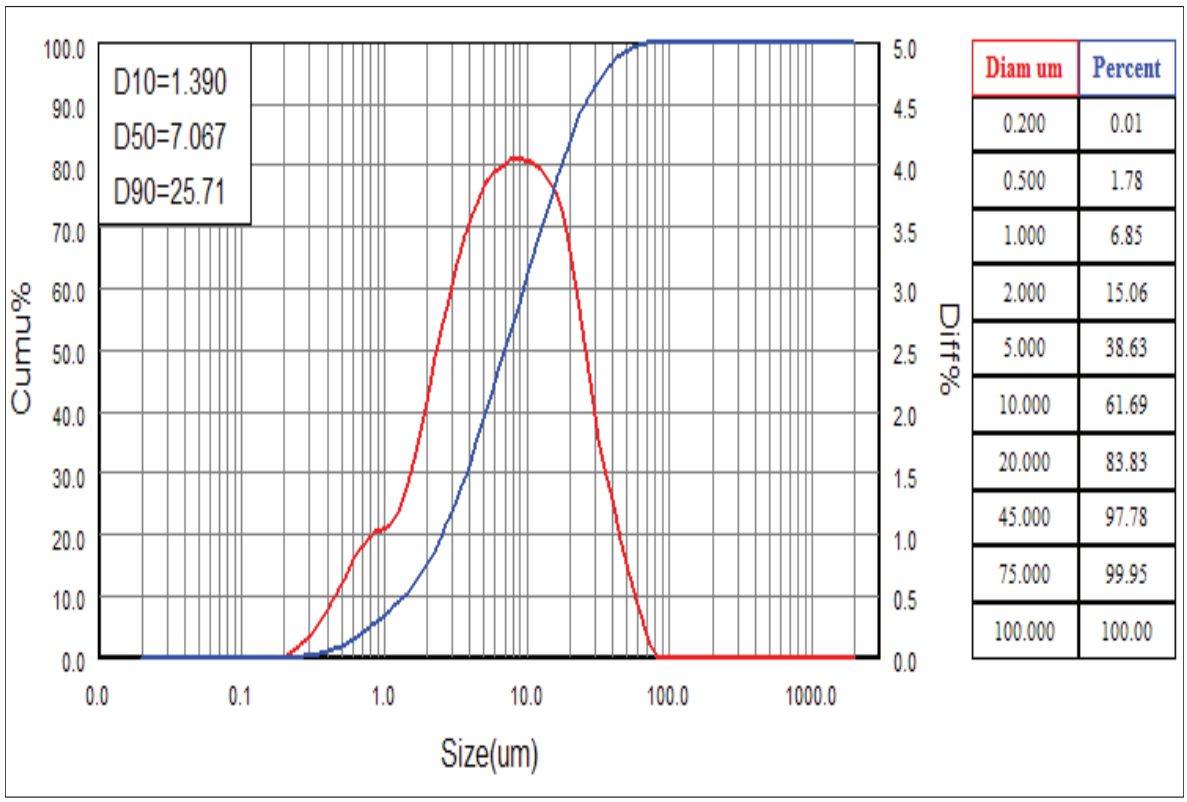

Diam um	Percent
0.200	0.01
0.500	1.78
1.000	6.85
2.000	15.06
5.000	38.63
10.000	61.69
20.000	83.83
45.000	97.78
75.000	99.95
100.000	100.00

Fig. (2): particle size distribution of Iraqi metakaolin.

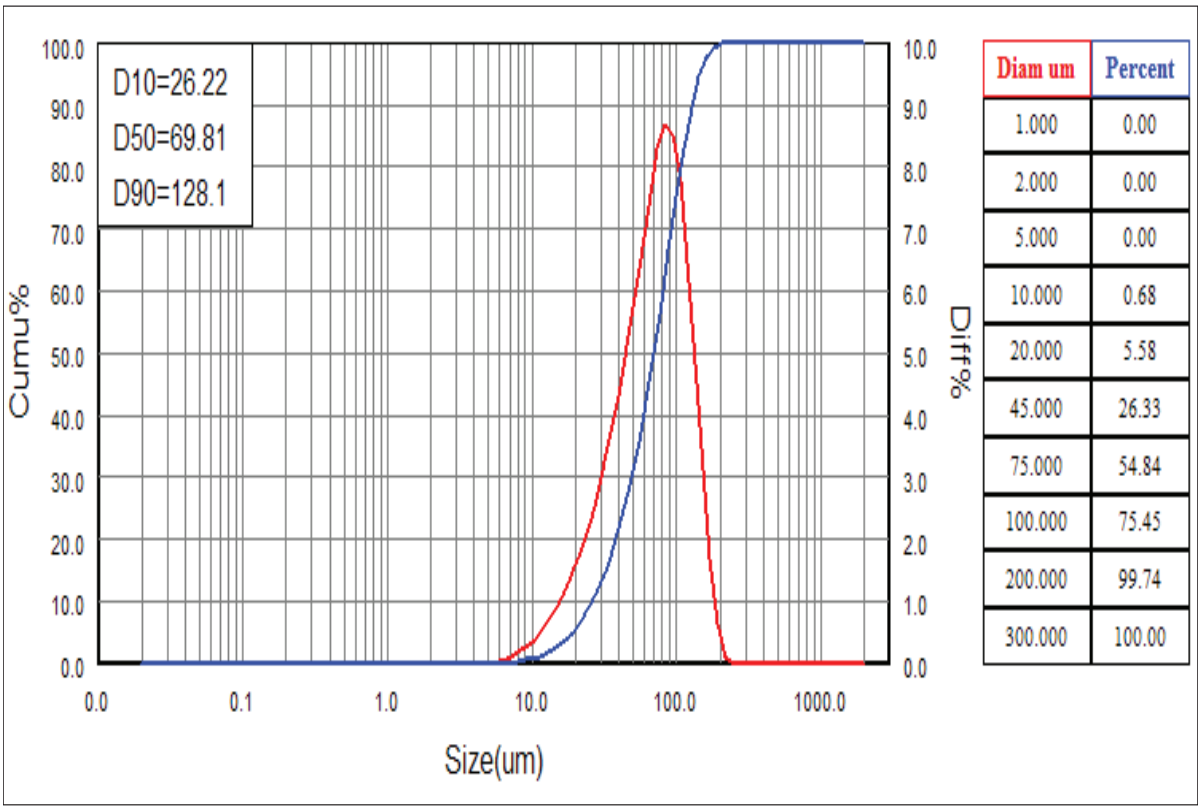

Diam um	Percent
1.000	0.00
2.000	0.00
5.000	0.00
10.000	0.68
20.000	5.58
45.000	26.33
75.000	54.84
100.000	75.45
200.000	99.74
300.000	100.00

Fig. (3): particle size distribution of SiC powder.

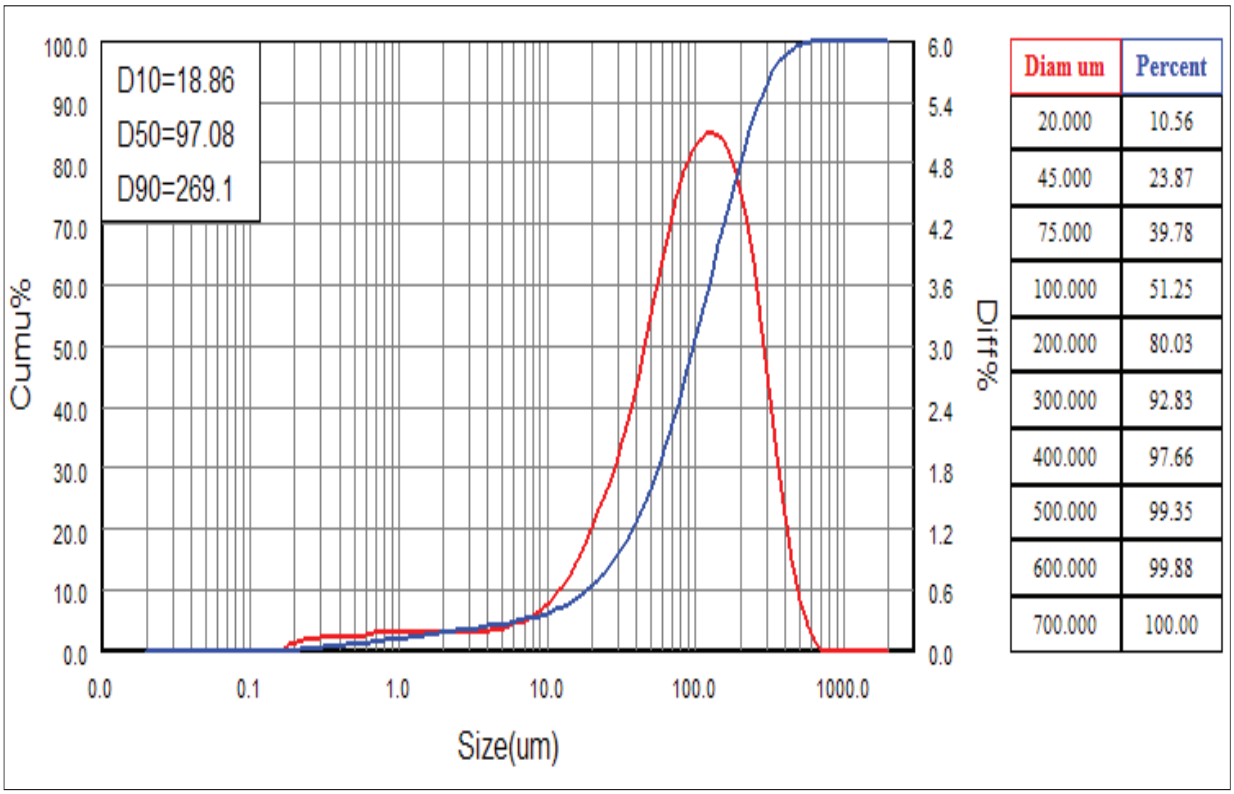

Diam um	Percent
20.000	10.56
45.000	23.87
75.000	39.78
100.000	51.25
200.000	80.03
300.000	92.83
400.000	97.66
500.000	99.35
600.000	99.88
700.000	100.00

Fig. (4): particle size distribution of fire brick powder(FBP)

2.3.3. Coefficient of thermal conductivity

The coefficient of thermal conductivity is measured by using a YBF-3 thermal coefficient meter, which depends on the steady state method The time required to measure the sample is two hours. The sample is placed between the two copper disks, after which the apparatus is programmed at (100)°C. After reaching the steady state, the voltage values V_1 and V_2 are taken. The irradiation rate of the lower copper disk, at the adjacent to V_2, was then calculated directly and the following equation is used:

$\lambda=(mch_B) / (\pi R_B^2 (V_1-V_2)) ((2h_p+R_p))/((2R_p+2h_p)) \Delta T/\Delta t_{T=T_2}$ $W.m^{-1}.C^{-1}$,

where:

V_1: the value of voltage of the upper copper disk,

V_2: the value of voltage of the upper lower disk,

m: the mass of the radiating disk, i.e. the lower copper plate,

c: the specific heat capacity of the copper plate ($3.805*10^2$ $jkg°C^{-1}$)

h_B: the thickness of the sample,

R_B: radius of the sample,

h_P: the thickness of the radiating disk,

R_P: radius of radiating disk,

$\Delta T/\Delta t_{T=T_2}$: The radiating rate of the lower copper disk at temperature adjacent to T_2.

3. Result and discussion

Fig. (5) shows the behavior of samples prepared from 70%))90%(kaolin +30%

metakaolin) with the additives. It is found that the bulk density increases with the increase of firing temperature until (1400) C°. This general behavior is due to the increase in the percentage of the liquid phase which forms the glass phase after the firing process [12]. While the density drops at (1500) C°. This is mainly a result of the expansion of gases (bloating) enclosed in the matrix due to the presence of Fe_2O_3 in the kaolin powder which changes into Fe_3O_4 and generates O_2 at elevated temperature [13,14].

As shown in Fig. (5) the bulk density values are greater in the case of (% 10) FBP. On the other hand, the addition of (5%) FBP+(5%) SiC caused increasing the values of bulk density compared with the addition of (10%) SiC alone. However, silicon carbide possesses the advantage of inhibiting sintering rate of the refractory material [15]. Silicon carbide is a crystalline material, the colour of which is determined by the level of impurities. Pure silicon carbide is colour less and transparent, the green to black colour of the industrial SiC results from impurities mostly iron [16,17]. Therefore, it is expected that samples prepared with addition of (10%) SiC will cause an increase in bloating during sintering leading to decreasing the values of bulk density.

Fig. (6) and three shows the variation of open porosity with the addition of FBP and / or SiC. Open porosity is found to be less when (10%) FBP is added, while open porosity is greater in case of (10%) silicon carbide. Hamisi *et a.l*[18] expressed the densification in term of open porosity where they found that the decrease in open porosity for Pugu kaolin is due to densification that has taken place. Therefore, sintering is less in samples containing (% 10) SiC as evidenced by high values of open porosity.

Fig. (7) shows the behavior of the coefficient of thermal conductivity of samples of prepared from (90%) (70%)K + 30% MK) with different additives of B.P and / or SiC with increased firing temperature. It is clear that the values of the coefficient of thermal conductivity are greater for samples containing (10%) SiC, while decreasing with decreasing SiC. While samples containing (10%) FBP have the lowest values for conductivity. It is important to say that porosity is an important cause of decreased thermal conductivity where thermal conductivity decreases in refractory materials as its porosity increases with the pores acting as non-heat conducting media [19].

Although the samples containing (10%) SiC have higher open porosity than the other samples but they have a larger values of thermal conductivity. This is because the thermal conductivity of SiC is (270) W / mK°[20]. In other words, the high value of SiC conductivity has a greater effect than the effect of increased open porosity. For example it was found that samples prepared from a mixture of SiC and alumina, at sintering temperature of (1500) C°, have a higher thermal conductivity than samples of prepared from alumina alone [21].

4.conclusion

From study the behavior of samples prepared from (90%) (70%kaolin +30% metakaolin) with additives with firing (1100), (1200), (1300), (1400) and (1500) C° some conclusion are found. It was found that, for all samples, the bulk density increases with increasing of firing temperature up to (1400) C° then the density drops at (1500) C°**.** The open porosity decreases with increasing firing temperature up to (1500) C°. The bulk density increases with increasing of FBP while the open porosity decreases with increasing of FBP. Finally, the values of the coefficient of thermal conductivity are greater for samples containing (10%) SiC.

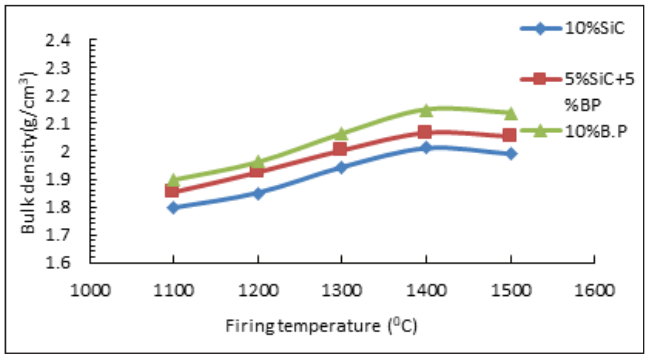

Fig.(5): variation of bulk density with firing temperature with different additives.

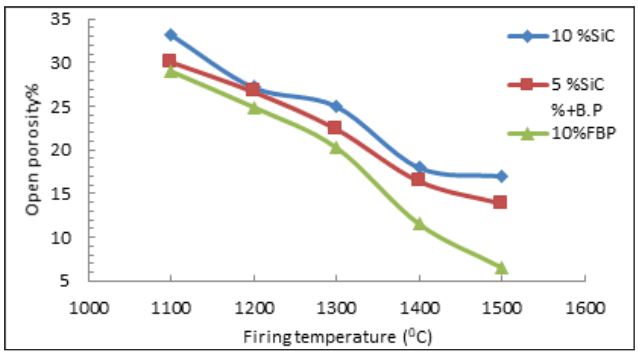

Fig (6): variation of open porosity with firing temperature with different additives.

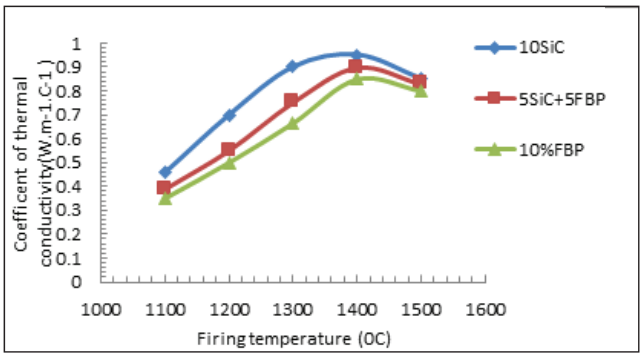

Fig (7): variation of coefficient of thermal conductivity with firing temperature with different additives.

References

[1] A. Craig, How cool are refractory materials, The Journal of The Southern African Institute of Mining and Metallurgy,108,1-16, (2008).

[2] C. Sikalidis, Advances in Ceramics - Characterization, Raw Materials, Processing, Properties, Degradation and Healing, (2011).

[3] D. Brosnan, Alumina-silica brick in Refractories Handbook , (2004).

[4] C. Sadika, I. Amranib, A. Albizaneaa, Recent advances in silica-alumina refractory: A review, Journal of Asian Ceramic Societies, 2, 83–96, (2014).

[5] C. Iyasara, M. Joseph, C.Azubuike, T. Danie ,Exploring Ceramic Raw Materials in Nigeria and Their Contribution to Nation's Development, American Journal of Engineering Research (AJER), 3, 127-134, (2013).

[6] F. Olufemi, Effects of sintering temperature on the phase developments and mechanical properties ifon clay, Leonardo Journal of Sciences, 26, 67-82, (2015).

[7] D. Al-Nasrawy, N.Dahham , A. Judran, Study the effect of kaolin addition on some physical and mechanical properties of α-SiC powder, Tikrit Journal of Pure Science, 15, (2010).

[8] A.Iyasara, E.Stan, O.Geoffrey, M.Joseph, N.Patrick, N.Benjamin, Influence of Grog Size

on the Performance of NSU Clay-Based Dense Refractory Bricks , American Journal of Materials Science and Engineering , 4, 7-12, (2016).

[9] J.Amkpa, A.Aye, F.Omagu, Mechanical and Physicochemical Evaluation of Alkaleri Fireclay for Refractory Application, Path of Scienc, 3, 15-20,(2017).

[10] E. Bwayo and S.Obwoya, Coefficient of Thermal Diffusivity of Insulation Brick Developed from Sawdust and Clays, Journal of Ceramics, 2014, 1-6, (2014).

[11] Standard Test Methods for Apparent Porosity, Water Absorption, Apparent Specific Gravity, and Bulk Density of Burned Refractory Brick and Shapes by Boiling Water, Designation: C20 – 00, (2010).

[12] M. Katayama, Y. Kawai, Y.Mizuno, K. Mizuno, M.Aoyama and Y. Kobayashi, Preparation of dense mullite polycrystals by reaction sintering of kaolin materials and alumina and their microstructure, Journal of the Ceramic Society of Japan, 122, 300-306, (2014).

[13] L. Akwilapo, K. Wiik, Ceramic Properties of Pugu Kaolin Clays. Part I:Porosity and Modulus of Repture, Bull. Chem. Soc. Ethiop., 17, 147-154, (2003).

[14] C. Chen, G. Lan, W. Tuan, Microstructural evolution of mullite during the sintering of kaolin powder compacts, Ceramics International, 26, 715-720, (2000).

[15] V. Pilli, Study on the alumina - silicon carbide - carbon based trough castable, M.Sc thesis, Department of Ceramic Engineering National Institute of Technology, Rourkela, (2015).

[16] J. Roy, S. Chandra, S. Das, S. Maitra, Oxidation behavior of silicon carbide Rev.Adv.Mater. Sci. 38, 29-39, (2014).

[17] N. Wright, Silicon Carbide, John Wiley & Sons, Inc, (2001).

[18] H. Hamisi, Seungyong Eugene Park, Byung-Hyun Choi, Yong-Taie An, Lee Jeongin, Influence of firing temperature on physical properties of Same clay and Pugu kaolin for ceramic tiles application, International Journal of Materials Science and Applications, 3, 143-146, (2014).

[19] I. Titiladunayo, O. P. Fapetu, Selection of Appropriate Clay for Furnace Lining In a Pyrolysis Process, Journal of Emerging Trends in Engineering and Applied Sciences (JETEAS), 2, 938-945, (2011).

[20] G. Harris, properties of Silicon Carbide, Published by: INSPEC, the Institution of Electrical Engineers, London, United Kingdom. (1995).

[21] R. Bareaa, M. Belmonteb, M. Osendia, P. Miranzoa, Thermal conductivity of Al2O3/SiC platelet composites, Journal of the European Ceramic Society, 23, 1773–1778, (2003).

Improving Band Width of Rectangular Microstrip Antenna for 5 GHz Application

Huda Sh. Gally
Zeki A.Ahmed
*Ahmad H. Abood
Physics Department, Science College, University of Basarh, Iraq
*Physics Department, Science College, Misan University, Iraq.

Received Date: 7 / 5 / 2018
Accepted Date: 11 / 9 / 2018

الخلاصة

الاتصالات اللاسلكية والاجهزة المحمولة قطعت شوطا طويلا منذ إنشائها وذلك من أجل التواصل. فنحن بحاجة إلى هوائيات مصغرة الحجم مثل الهوائيات الشريطية microstrip antennas. في هذا العمل، اقترح هوائي شريطي مستطيل الشكل antenna microstrip Rectangular. ويعد من التصاميم المستقبلية للاتصالات المتنقلة التي تعمل بالجيل الخامس (5) كيكاهرتز، يتركب الهوائي من مشع مستطيل الشكل على المادة العازلة (FR-4) والتي ثابت عزلها (4.4). وتم عمل قطع على شكل[ ][ ] في المشع المستطيل لغرض تحسين عرض النطاق الترددي، وقد اظهرت النتائج ان عرض الحزمة أصبح يساوي (20٪) وكذلك تحصيل الهوائي بلغ (7.41) ديسيبل عند التردد (5.1) كيكاهرتز. تم تنفيذ تصميم الهوائي والمحاكاة باستخدام طريقه العناصر المنتهية (FEM) باستخدام برنامج HFSS.

الكلمات المفتاحية

هوائي شريطي مستطيل الشكل، HFSS ، FR-4، عرض النطاق الترددي، طريقة العناصر المنتهية.

Abstract

The wireless communication has developed very fast since its creation. So for efficient communication we require miniature sized antennas such as microstrip antenna. In this paper, it proposes an efficient wide band rectangular microstrip antenna. In Equally important this design of future antenna for 5G mobile communication, a rectangular patch is mounted on FR-4 substrate material with dielectric constant (εr =4.4). A slot shape (] [) is etched on the rectangular patch to provide wideband operation, which provide a wider bandwidth of (20%) and high gain of (7.41) db. Antenna design and simulation were carried out in Finite Element Method (FEM) based High Frequency Structural Simulation (HFSS) tool. This antenna has good performance in terms of antenna Band width, return losses, VSWR, Characteristics impedance, and gain at the frequency (5.1) GHz.

Keywords

Rectangular Microstrip Antenna, FR-4 Substrate, HFSS, Bandwidth, FEM.

1. Introduction

The wireless communication system needs small antennas for mobile devices, and high band wide in multi-frequency bands for different applications [1].

In fact, the future wireless networks also require high band width systems with high mobility environments [2].

The principal advantages of microstrip antenna include, small size, light weight, low fabrication cost, low profile planar, and can be manufactured either as a separate component or part of array [3].

Some of disadvantages of microstrip antenna are: narrow bandwidth; low efficiency; low Gain; and thicker substrate results in excitation of surface waves [4].

The simplicity of Microstrip antennas and compatibility with printed circuit technology Led to great interest in them recently and its use on a widely in the microwave frequency spectrum. Microstrip antenna consists of dielectric substrate and conducting patch printed on in one side and in the other side printed a conducting ground plane [5].

Therefore, the radiating element can be take several shapes such as a rectangular, square, monopole, circular, triangular, circular ring, and elliptical, or other configuration. As a result, there are special features for each shape, but the rectangular, circular and square shapes are the most common configurations [6].

The used of different materials to design the dielectric substrate of microstrip antennas, where the range dielectric constant of this materials usually in ($2.2 \leq \varepsilon r \geq 12$). The thickness (h) is small fraction of a wavelength ($h << \lambda o$) [7]

Equally important, the ground plane of antenna is placed below dielectric substrate and represents the third part of the microstrip antenna. The ground plane is made of the same conductive material as the patch.

The dimension of ground plane effect on the edge fields (fringing fields) Which is very important to increases the radiation from the microstrip antenna [8].

There are different methods to feeding the patch of microstrip antenna such as the transmission line feed, coaxial probe feed, aperture coupling feed and proximity coupling feed.

Of these methods, connected or unconnected, connected methods include direct connection between the patch and transmission line. But in unconnected method used coupling electromagnetic field method to transfer energy to the patch [9].

The different techniqes have been used leately to increase the bandwidth of microstrip antennas [10], such as increasing the height of the substrate, microstrip slot antenna loaded approach on the patch and using different shapes of microstrip patch [11].

By increases thickness of substrate increases the gain, but may lead to surface wave excitation which decrease efficiency and perturb the radiation pattern [12].

Different shapes of slot loading in radiated patch to improving the antenna bandwidth [13].

In this study, a slot shape (] [) patch antenna were designed with coaxial -probe feed.

The software which is the industry standard for simulating high-frequency electromagnetic structure (HFSS).

2. Design of RMSPA in 5.2 GHz

To design an initial antenna in (5^{th}) generation (a future antenna for 5G mobile communication) and in the ultra-wide band UWB application for wireless communication. In this work, three parameters must be selected, there are: Resonance frequency is (5.2) GHz, the dielectric constant of the substrate is (4.4) (FR4-epoxy) , thickness (3.5)mm. The size of rectangular patch antenna are (46×33) mm^2, the size of ground plane is (67×54.8)mm^2. The co-axial feeding technique is used and the optimum location of feed is (0, -5) mm.

3. Design of RMSPA in 5.2 GHz with slot shape (] [)

The slot techniques etched in the rectangular patch is used here to improving the bandwidth of the antenna. The slot shape (] [) was to be etched in the rectangular patch of the proposed antenna, as shown in Fig. (1).

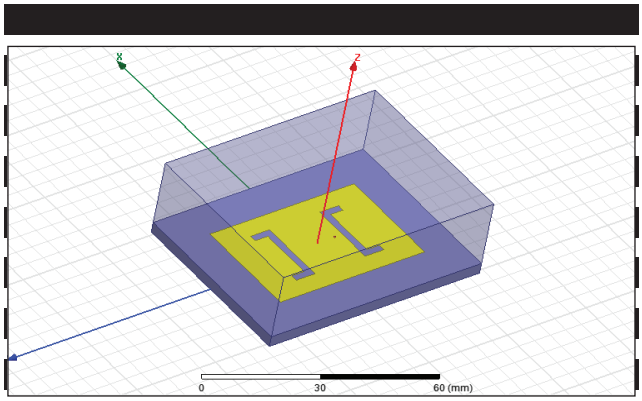

Fig. (1) rectangular antenna with ( ] [ )-slot

The dimensions of antenna with] [-slot as shown in Fig. (2), the total area of patch is (L x W) printed on a FR4 substrate having dielectric constant (4.4) with size (L_g x W_g), with thickness is (h). The antenna uses co-axial feeding technique, The position of feed point is (X_f, Y_f), where the feed location and the slots were tuning to give good impedance matching.

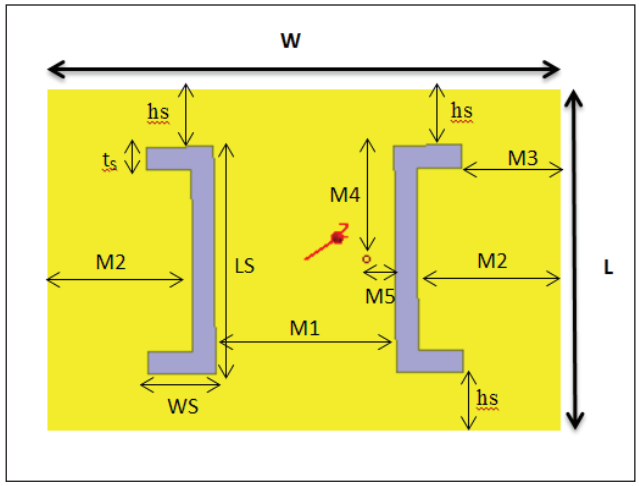

Fig. (2): Dimensions of Rectangular patch loaded by slot shape (] [)

4. simulation results of RMSPA in (5.2) GHz

Return loss versus frequency is shown in Fig. (3). While it is true that the bandwidth is(3.1%) at (4.5)GHz,(2.5%) at (5.2) GHz and (1.6%) at (6.26)GHz. The return loss value of these bands is (-18.06 dB,-18.9 dB and -13.39) dB respectively.

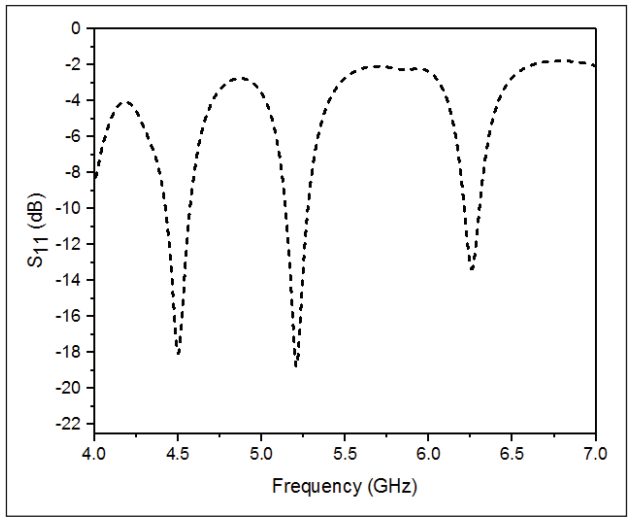

Fig. (3): Return loss of RMSPA at 5.2GHz

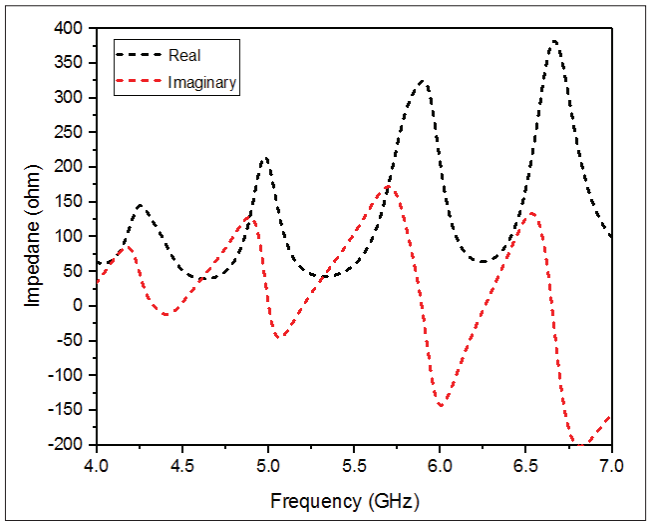

Fig. (5): Real and imaginary parts of the input impedance of RMSPA at (5.2) GHz

VSWR (Voltage Standing Wave Ratio) versus frequency is shown in Fig. (4). The values of VSWR for rectangular microstrip patch antenna is (1.10, 1.03 and 1.15) at (4.5) GHz, (5.2)GHz and)6.26(GHz respectively.

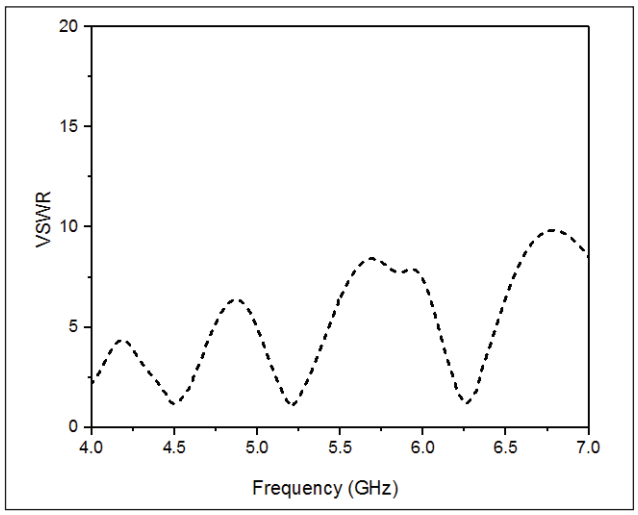

Fig. (4): VSWR of RMSPA at)5.2(GHz

The input impedance of rectangular microstrip antenna is shown in Fig. (5). The figure shows, at frequency (5.2) GHz, the real part of impedance approximately (50) Ω while the imaginary part equal to zero.

2-D radiation pattern antenna at (5.2)GHz as shown in Fig. (6). The Fig. shown as E and H-Plane radiation pattern of rectangular microstrip antenna,

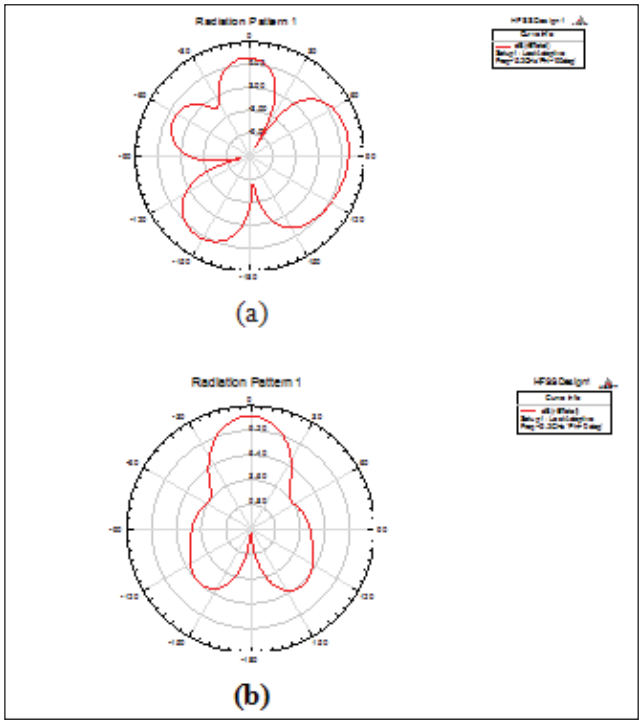

Fig. (6): E and H -Plane radiation pattern of RMSPA at (5.2) GHz

The gain of the proposed antenna is shown in Fig. (7). The maximum gain is (6.24)dB at (5.2)GHz, and the average gain is (5.12)dB.

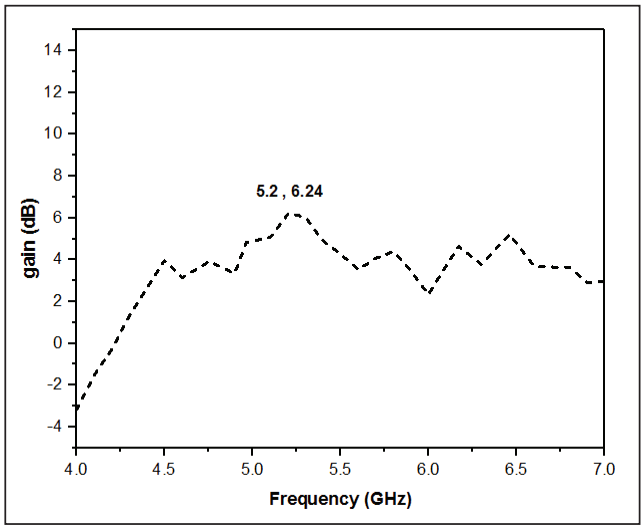

Fig. (7): gain of RMSPA at)5.2(GHz

As shown above the performance parameter of a rectangular patch is shown in Table (1).

Table (1): RMSPA performance parameters at (5.2) GHz

S11	-18.9 dB
Bandwidth	2.5%
VSWR	1.03
Average Gain	5.12 dB

5. simulation results of RMSPA with slot shape (| |)

Parametric study done to get the optimum dimension for the slot, to get the best value of band width. For different values of (ts), when (Ws = 6mm), the results show the best value of a bandwidth for the thickness of the slot equal to (2) mm , as in Fig.(8).

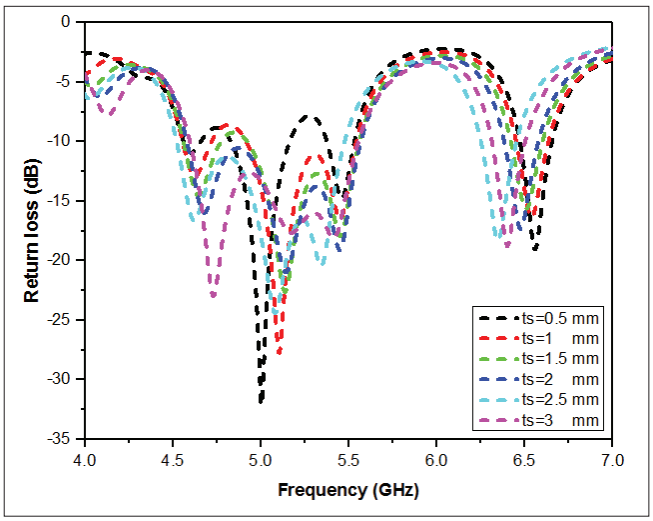

Fig. (8): Return loss of proposed antenna with different ts value>

Now, for the thickness of the slot (ts = 2) mm, the results show that, the best value of a bandwidth was obtained at the width of slot equal to (6) mm, as in Fig. (9).

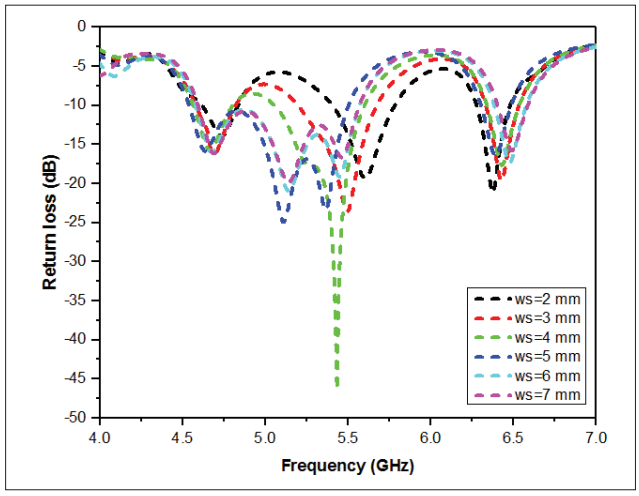

Fig. (9): Return loss of proposed antenna with different Ws of slot.

The optimum dimensions of the patch and slots of the proposed antenna, with the best value of the band width listed in Table (2).

Parameters	Value
Size the ground plane (Lg × Wg)	52 mm * 67 mm
Dielectric constant (ε_r)	4.4 (FR4-epoxy)
Thickness of substrate (h)	3.5 mm
Size of the patch (L × W)	31mm x 46 mm
Feed position (X_f , Y_f)	(0 mm , -5.5 mm)
Frequency	5.1 GHz
Size of the slot Ls × Ws	20 mm * 6 mm
thickness of the slot t_s	2 mm
hs	5.5 mm
M1	16 mm
M2	13 mm
M3	9 mm
M4	10 mm
M5	2.5 mm

According to the dimensions listed in the Table (2), the return loss of (] [) -slot antenna shown as in Fig. (10). The bandwidths for (-10) dB return loss ranging from (4.5 to 5.54) GHz or (% 20.4) especially at (5.11) GHz, and ranging from (6.35 to 6.540) or)3%(at (6.44) GHz.

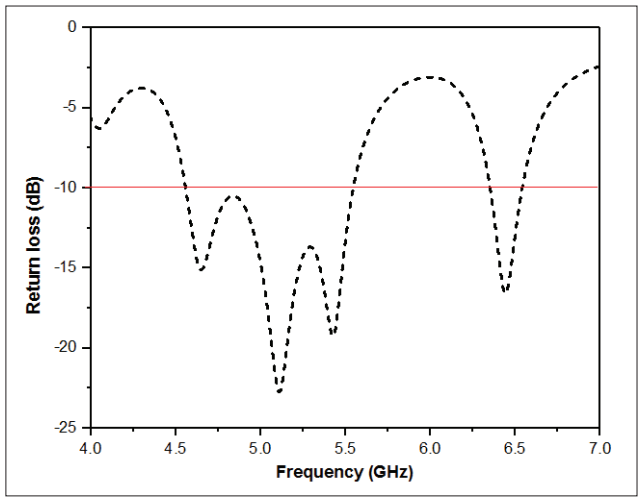

Figure (10): Return loss of proposed antenna

The values of VSWR are (1.09 and 1.26) for the antenna at resonant frequencies at (5.11) GHz and (6.44) GHz as shown in Fig (11).

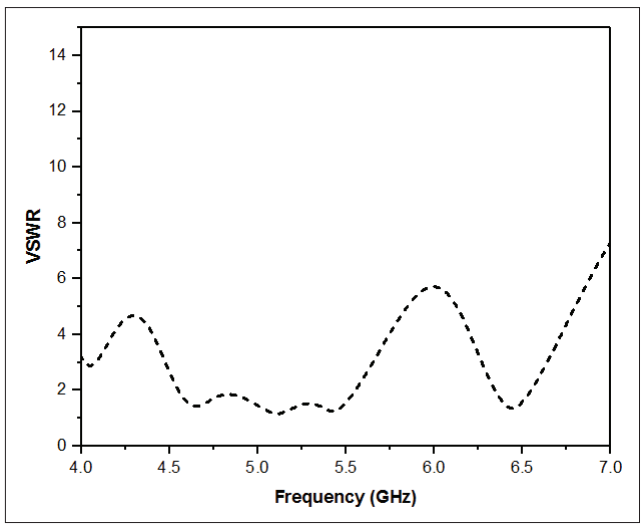

Fig. (11): VSWR of the proposed antenna.

The input impedance as shown in Fig. (12), at resonant frequency (5.1) GHz the real part of impedance is approximately (50) Ω and the imaginary part is zero

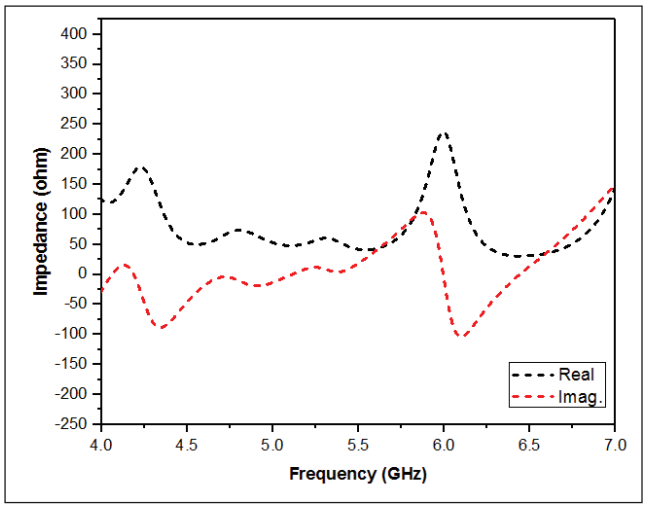

Fig. (12): The real and imaginary part of input impedance vis. Frequency.

The proposed antenna's radiation patterns are shown in Fig. (13).

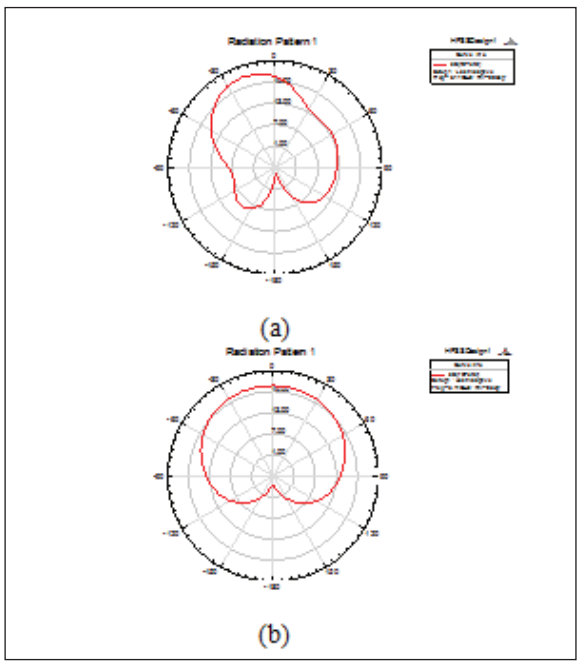

Fig. (13): (a) E-plane and (b) H-Plane pattern of proposed antenna at)5.11(GHz

The gain of proposed antenna shown in Fig. (14). The maximum gain is (7.41) dB at (5.11) GHz and the average gain is (6.5) dB.

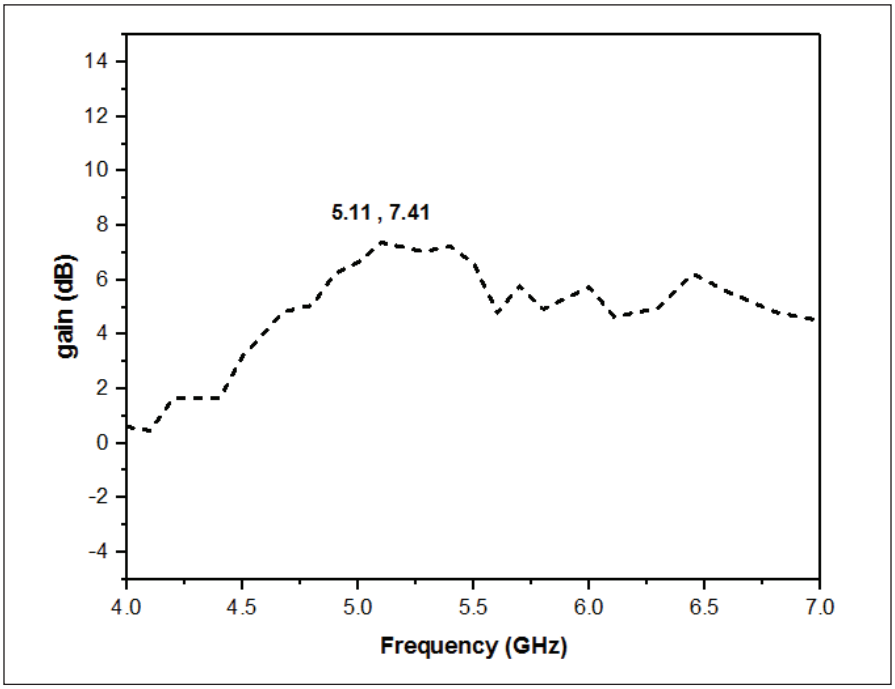

Fig. (14): The gain of the proposed antenna at (5.11)GHz.

As shown previously above the performance parameter of the proposed antenna is shown in Table (3).

Table (3): Proposed antenna performance parameter

f_r	5.11 GHz
S_{11}	-22.735 dB at 5.11GHz and -16.6 dB at 6.44 GHz
B.W	20% at 5.11GHz and 3% GHz at 6.44 GHz
VSWR	1.09 at 5.11GHz and 1.26 at 6.44 GHz
average gain	6.5 dB

6. Conclusion

In this work we proposed a rectangular micro strip patch antenna with (] [)-shaped slot to improving the band width of micro strip antenna. The proposed antenna was designed at (5.1)GHz with wider bandwidth and high gain. Hence this antenna used widely in different applications of communication system.

Reference

[1] M. Ali, T. Sittironnarit, H.S. Hwang, R. A. Sadler, and G. J. Hayes, "Wide-Band/Dual-Band Packaged Antenna for (5–6)GHz WLAN Application," IEEE Trans. Antennas Propagat., vol.52, N.2. pp. 610-615, February. (2004).

[2] Pankaj Sharma, " Evolution of Mobile Wireless Communication Networks-1G to 5G as well as Future Prospective of Next Generation Communication Network ", A Monthly Journal of Computer Science and Information Technology, Vol. 2, Issue. 8, pg.47 – 53, August (2013).

[3] Supriya J., " The Application of Ku-band VSAT Systems to Single Layer Hexagonal Micro Strip Patch Antenna ", International Journal of Modern Engineering Research (IJMER), Vol.3, Issue.2, pp-1150-1156, March-April,)2013(.

[4] V. Mohan Kumar, and N. Suit," Enhancement of Bandwidth and Gain of A rectangular Micro Strip Patch Antenna ", Thesis of Bachelor of Technology, National Institute of Technology Rourkela, (2010).

[5] Christopher B. S., "Wideband Dual-Linear Polarized Micro Strip Patch Antenna", M.Sc. Thesis from Texas A&M University, December, (2008).

[6] Abdul Rashid O. M. W., " Analysis of Three Different Dielectric Substrates on Square Ring Slot Micro Strip Patch Antenna for Wireless Application ", MS.c Thesis, Universiti Tun Hussein On Malaysia, January, (2015).

[7] Amite T., Manoj C. and Mithilesh K., " Effect of Substrate relative dielectric constant on Bandwidth characteristics of Line Feed Rectangular Patch Antenna", International Journal of Engineering Science Invention Research & Development, Vol(I). April (2015).

[8] Constantine A. B., " Antenna Theory: Analysis and Design" Third edition, A john Wiley & SONS, Canada, (2005).

[9] Khalid A.A.," Development of Compact Rectangular Micro Strip Patch Antenna for Wimax, Fixed Service Satellite and Microwave C-Band Applications ", M.Sc Thesis , Universiti Tun Hussein On Malaysia , January, (2014).

[10] W. G. Whitlow, S. S. Bukhari, L. A. Jones and I. L. Morrow, " Applications and Future Prospects for Microstrip Antennas using Heterogeneous and Complex 3-D Geometry Substrates ", Loughborough University Institutional Repository, (2014).

[11] Raed M.s., " Design and analysis of Circular Microstrip Antenna Loading by Two Antenna Rings ", Ph.D Thesis , University of Basra , Collage of Science, (2017).

[12] D. Orban and G.J.K. Moernaut, " The Basics of Patch Antennas, Updated ", edition of the RF Globalnet, September, (2009).

[13] E. Shigeru, and E. Nishiyama, "Stacked microstrip antenna with wide bandwidth and high gain" IEEE. Trans. Antennas and Propagate. 44, (1996).

Performance Study of a Solar Powered Ice Maker Operating in Baghdad-City

*Abdual Hadi N. Khalifa
*Ahmed Q. Mohammed
*Asaad T.AL-Omran
**Amar Sadoon Abdul Zahara
*Engineering Technical College- Baghdad Middle Technical University
** University of Technology.

Received Date: 18 / 6 / 2018
Accepted Date: 9 / 8 / 2018

الخلاصة

يمتاز العراق بوفرة في الطاقة الشمسية، والتي يمكن الاستفادة منها في امداد العديد من المنظومات الشمسية بالطاقة بما ذلك انظمة التبريد والتثليج الامتزازي. تم بناء منظومة تثليج امتزازيه تعمل على الطاقة الشمسية وتستخدم زوج الكاربون المنشط– الميثانول في مدينة بغداد. تتكون المنظومة من مولد ابخار الشمسي بمساحة سطحية تساوي (0.211) م^2 ويحتوي مولد البخار على (3) كغم من حبيبات الكاربون المنشط من النوع (NORIT PK 1–3) وكان قطر الحبيبات بحدود (3.15) ملم. يعمل الكاربون المنشط كوسيط ماز لبخار الميثانول . ويضاف الى مولد البخار مكثف مبرد بالهواء الحر لتكثيف بخار الميثانول الخارج من مولد البخار. اما مبخر المنظومة فقد غمر في وعاء بحجم (1) لتر من الماء لغرض تحويل الماء الى ثلج. تم دراسة تأثير تغير النسبة الوزنية للميثانول الى الكاربون و ضغوط المنظومة على اداء منظومة التثليج الشمسية. بينت النتائج ان الانتاج اليومي للثلج بلغ (1) لتر في اليوم الواحد عندما كانت مساحة مولد البخار (0.211) م^2. أي ما يعادل (4.8) كغم ثلج / م^{2}يوم.

الكلمات المفتاحية

الطاقة الشمسية، التثليج الشمسي، منظومة تثليج شمسية امتزازية، التثليج الامتزازي.

Vol. 10, No. 19 and 20 P. (77-86), Sept., 2019

Abstract

Iraq is characterized by high abundance of solar energy, which can run many solar energy systems, including adsorption refrigeration systems. A solar-powered adsorption ice maker was built in Baghdad- Iraq. The ice maker works on two adsorption pairs, namely activated carbon and methanol. The unit generator is a flat plate solar collector of (0.211) m^2 filled with a grain activated carbon. The flat plate collector was covered using a glass sheet of 6 mm thickness. A (3) kg of granular activated carbon type (NORIT PK 1-3) of particle size is of (3.15) mm is used as an adsorbent. Methanol is used as a desorbent medium. Different mass of methanol is used to achieve different mass ratios of activated carbon and methanol. A natural air-cooled condenser was used to condense the methanol vapour, while, the evaporator was immersed in a water bath of 1-litre volume, intended to be frozen. The maximum solar coefficient of performance is about 0.36, while the minimum is approximately (0.1). The daily production of ice was (1) litre when the top collector area of (0.211) m^2, which is equivalent to (4.8) kg ice/m^2.day.

Keywords

Solar energy, solar refrigeration, solar ice maker, adsorption refrigerator.

1. Introduction:

Various research and development efforts have been made to predict the performance of the solar-powered ice maker.

In 1987, Pons and Guilleminot, 1986 [1] had designed a solar-powered ice maker, with 6 m^2 top collector area. The collector containing about (130) kg of active carbon, the net production of ice was (30-35) kg per day. The net COP was about (0.12). Some of the specific aspect of such machines, like heat transfer within collector, the delayed of adsorption end and the chimney effect between collectors were introduced. Lemmini and Meunier, 1990 [2] have presented a numerical simulation of one-year around the operation of a solar adsorption refrigerator operated with active carbon and methanol, the highest efficiency was obtained in winter and the average solar COP was (0.14). The solar ice maker adsorptive model was studied by Boubakri et al., 2000 [3] the identification procedure is carried out employing an experimental data base obtained from tests carried out on two adsorptive solar-powered ice-makers using a methanol/carbon pair. The packaged component, the collector–condenser, represents the main new feature of these units. The prediction is compared with results of correlations. This allows a comparison of the collector–condenser behavior in the two units since the collector–condenser of one of these units is equipped with a radiation shield. The model is then used to study daily ice production sensitivity vis-à-vis critical physical parameters of the unit and to estimate the limits of the collector–condenser technology with flat plate collectors.",”DOI”:”10.1016/S0038-092X(00, A two solar ice makers were tested, each cycle operating on methanol/carbon pair. The experimental data was as input to theoretical model. The results of the theoretical model were, the rear and front side heat transfer coefficient of the generator and condenser were obtained. Y. and Wang, 2007 [4] have reported a survey of novel technology to improve adsorption system and make it become a realistic alternative; more than (100) patients were classified into four main groups. Leite et al., 2007 [5], presented the thermodynamic processes of the adsorption cycle and the experimental results of a solar icemaker use activated-carbon methanol pair. The collector-generator consists of multi-tubular with an opaque black radiation-absorbing surface. The maximum ice production was (6.05)kg, per meter square of collector area, when the generator temperature was (100) °C. The results of an adsorptive system driven by solar energy were simulated by Freni et al. 2008 [6]. The unit was used for freezing and cold storage. The generator that contained the activated carbon was connected to a solar collector and an evaporator. The production of the unit was (5) kg of ice/day, The simulation of a solar ice maker working on the active carbon/methanol pair was introduced by Vasta et al., 2008 [7]adsorbent bed, condenser and cold chamber (evaporator and water to be frozen. The adsorption/ desorption processes through the condenser and the generator cy-

cle were described, the experimental test was carried out in north Mediterranean climate. A heat and mass recovery adsorption chiller has been designed and tested by Luo et al., 2010 [8]. The chiller under study consist of a two adsorption units, cooling tower, two stages evaporator and a fan coil unit. The adsorption pair was activated carbon- methanol. The key variables under study were temperature of hot water, chilled water temperature, time of heating and cooling processes. A two bed (1.5) adsorption chiller with mass recovery was studied by Khalifa et al., 2013 [9], the authors mentioned that a semi continuous chiller was produce when using two generators with the chiller. Simple manual valves were used to switch between the two generators. The adsorption pair was activated carbon-methanol. M.A et al., 2015 [10] has presented a tubular solar collector/adsorber intended for the adsorption refrigeration unit. Activated carbon–methanol was used as an adsorption pair. Heat and mass transfer in adsorbent bed and energy balance in the solar collector/adsorber was solved using Dubinin–Astakhov equation. Effect of some parameters, such as adsorption pair, the size of adsorber tube, the tube material and collector glazing cover, on the system performances, were investigated A two beds car adsorption chiller was introduced by Khalifa et al., 2015 [11], a two copper tube were installed concentrically to form the unit generator. Two activated carbon layers were used to line the inner surface inner copper tube, the two layered were spaced by (5) cm. the exhaust gas was simulated using propane burner to produce a hot gases in the temperature range of (80 to 140) °C. The tubular adsorber of solar adsorption cooling system was presented by Chekirou et al., 2016[12]. The unit was driven by a flat-type solar collector. Three different configurations of glazes were studied, namely; single glazed cover, double glazed cover and, transparent insulation material cover. The modelling and the analysis of the adsorber were the key points of the study. Solar energy was used to heat adsorber. The unit generator contains a porous activated carbon with methanol. Cherrad et al., 2018 [13]a transient numerical model, referred as CBSR model, was developed for determining the operating temperatures and its corresponding times of the solar adsorption refrigeration cycle with activated carbon AC35-methanol pair for unsteady solar irradiation. The operating temperatures and its corresponding times obtained by the present model compared with those of the literature showed an acceptable difference, whereas the study introduced most factors which can affect the performance of the machine. The presenting of the operating temperatures of the solar adsorption refrigeration cycle as a function of solar cold generation energy allowed to sweep the interval of cycle temperatures of functioning of the machine according to climatic conditions (solar irradiation and ambient temperature, has used a transient numerical model to determine the operating temperatures and the corresponding times of the activated carbon AC35-methanol

solar adsorption refrigeration cycle. The temperatures and its corresponding times, which obtained from the presented model, were compared with those of the literature showed an acceptable difference.

In this work, a solar adsorption ice maker was designed and built to produce (1) litre of ice. The unit performance is studied under the variation of working pressure and the mass ratio of activated carbon to methanol.

2. Principles of adsorption cycle

The adsorption refrigerator is constructed out from two containers, the first one represent the evaporator, while the second one is adsorber. The two containers, condenser and valves were connected together using copper tubes. Four processes can be recognized for the typical adsorption refrigeration cycle as shown in Fig. (1). Starting with the Isosteric heating process (1-2), in this process the system temperature and pressure increases due to solar radiation incidence on the flat plate solar collector that contains active carbon and methanol. The second process is the desorption and condensation process (2-3), desorption of methanol included in the active carbon and condensation of vapour in the air-cooled condenser. The third process isosteric cooling (3-4), during the period when solar radiation is at its lower value, active carbon cools through removing of back insulation from a collector, so that, both pressure and temperature of desorber decreases due to rejection of sensible heat. The fourth process is Isobaric (4-1), refrigeration process occurs, where both sensible and latent heat is extracted from the adsorber. The coefficient of performance (COP) is the measure of cycle performance and can be calculated as follows:

$$COP = \frac{\frac{m_w c_w (T_i - T_f)}{\Delta t_c} + \frac{m_{ice} h_f}{\Delta t_f}}{I.\tau.\alpha.A}$$

Where:

m_w and m_{ice}: Mass of water and ice respectively (kg).

c_w: Specific heat of water (kJ/kg K).

T_i and T_f: Initial and final temperatures of water (°C).

h_f: Latent heat of water fusion (kJ/kg).

Δt_c: Time required to cool water from initial to final temperature (s).

Δt_f: Time required to freeze the water (s).

I: Solar radiation falls on tilt surface (kW/m2).

τ and α: Transmissivity and absorptivity of glass cover.

A: Collector area m2.

3. Construction of the solar refrigerator

To find out the best mass ratio of active carbon to the methanol, working pressure and working temperatures, an experimental pilot device made of a small glass ice maker was built firstly. The glass ice maker that is shown in Fig. (2) was built from around bottom, three necks glass flask of (1) litre volume, which acts as vapour generator, a glass condenser, and a round bottom glass flask, which serves as an

evaporator. The generator is heated by a hot water bath, while, the evaporator is immersed in another water bath at ambient temperature. Different experiments were achieved; the key variables are the mass ratio of activated carbon to the methanol. After finding the suitable mass ratio of active carbon to methanol, working pressure and temperatures, the solar-powered ice maker was built as shown in Fig. (3).

This solar-powered ice maker aims to produce about (1) kg of ice per day, so, the components of the system should be specified and designed to meet this objective.

The components of the solar powered ice maker are flat plate solar collector of dimensions of (460×46050 ×) mm .The collector was made from a copper plate of 1 mm thickness, and contain about (3) kg of active carbon. The cooling of the collector during the night is improved by using air dampers within the collector.

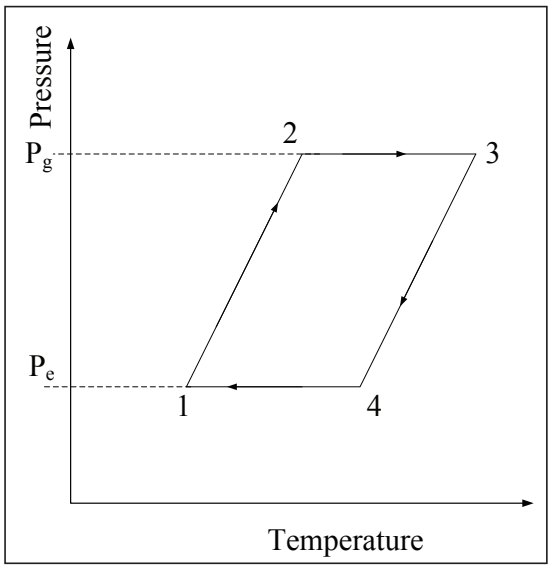

Fig. (1): Adsorption refrigeration cycle

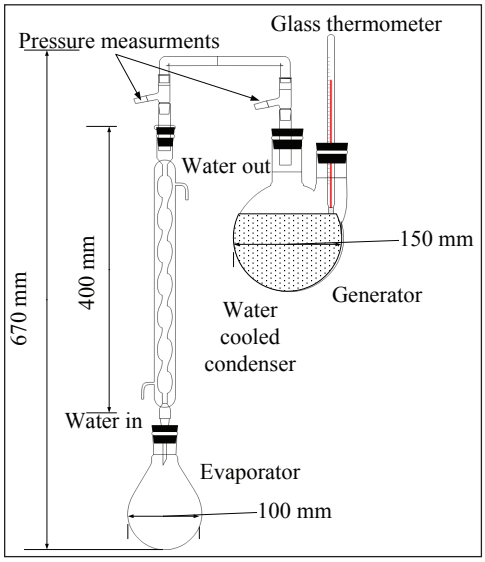

Fig. (2): The pilot adsorption refrigeration unit

To enhance the heat, transfer between the top side of collector and adsorbent, four copper fines are placed inside the collector in contact with top side and adsorbent, as shown in Fig. (3). The air-cooled condenser was made of finned copper tubes. A glass flask of (0.5) litre volume was used as a receiver and equipped by a valve, as shown in Fig. (3a). The glass flask was used to measure the volume of condensate methanol. Finally, an evaporator of dimensions of (26026 ×260 ×) mm, made from a copper plate of (1) mm thickness. The evaporator was immersed in a water bath of (1) litre volume at ambient temperature. The receiver, evaporator and water bath are placed in an insulated container. The temperature were measure at (18) points, two pints at the condenser surface, (6) points at the collector surface, another (6) point through the collector, the remaining thermocouples are used to measure the evaporator, water around the evaporator, receiver and ambient tempera-

tures. All thermo couples were inserted in copper tubes of (5) mm in diameter, then the copper tube were installed through the unite generator, as shown in Fig.(3b).

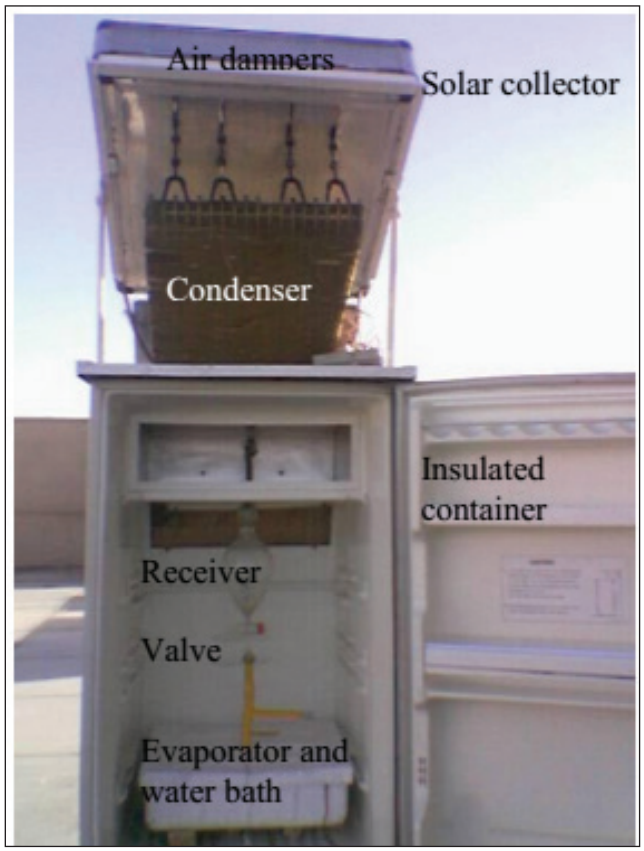

Fig. (3a): the solar adsorption ice maker

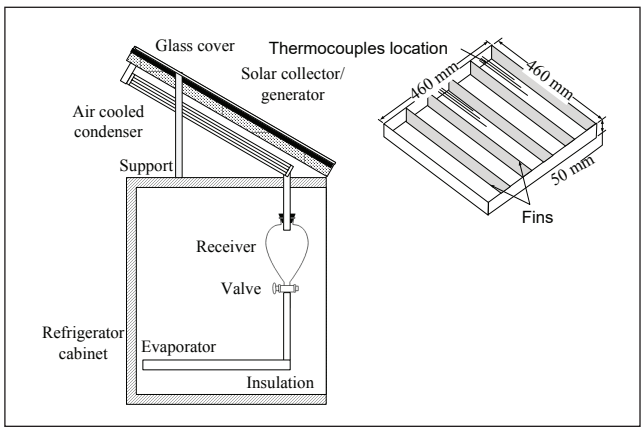

Fig. (3b): The solar adsorption ice maker, showing the solar collector

The solar-powered ice maker is built in Baghdad, Iraq to undergo the first cycle in middle August. The key variables to be examined are working pressure; namely; (3, 3.5, 4 and 5) kPa. and the under study mass ratios were (3.8:1, 3.2:1 and 2.56:1).

4. Results and discussion

Fig. (4) shows the variation of the temperature of unit components with the time, when the mass ratio (MR) of activated carbon to the methanol of (3.8:1) and the working pressure is (5) kPa. It can be seen from the figure that, the maximum mass of condensate methanol is about (275) grams, while the minimum temperature of the evaporator is about (5) °C, and it remains constant for about (2) hours. It can be seen from the figure that the activated carbon temperature follows the collector outer surface temperature. It can be seen that the mass of liberated methanol starts from (10) hr due to the opening the valve separated generator. As the solar radiation increases, the mass of liberated methanol increases rapidly tell (16) hr, then the mass of methanol kept constant 16 to (24) hr. due to constant pressure of generator during the period of time mentioned above.

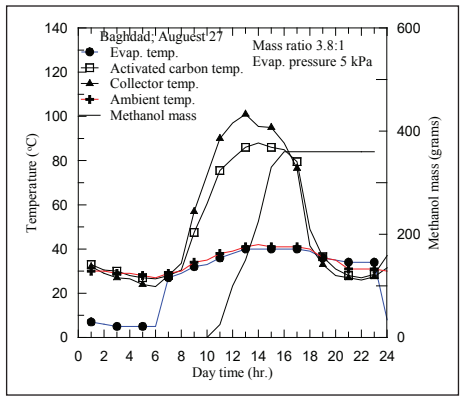

Fig.(4): The variation of condensate methanol mass and cycle components temperatures with the day time, mass ratio is 3.8:1 and evap. Pressure is (5) kPa.

Fig. (5) shows the variation of the temperature of unit components with the time, when the MR is held constant at (3.8:1), but the working pressure reduces to (4) kPa. It can be seen from the figure that, due to the reduction in working pressure, the mass of condensate methanol increases to (315) grams, while the evaporator temperature reduces to (0)°C, for about (2.5) hours. The maximum collector temperature follows the solar radiation.

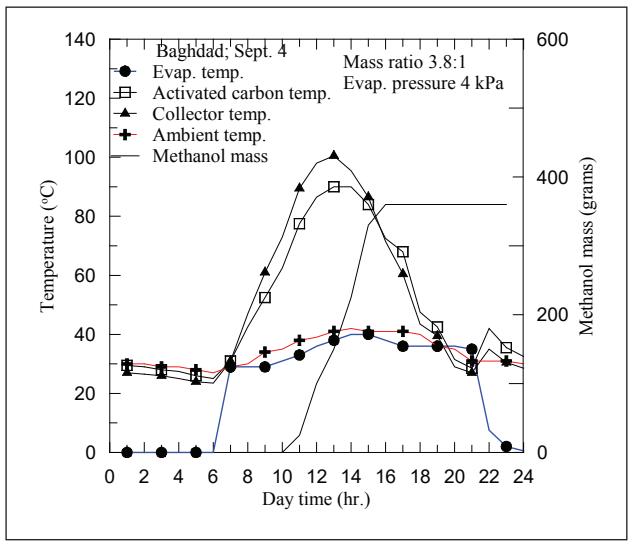

Fig. (5): The variation of condensate methanol mass and cycle components temperatures with the day time, mass ratio is 3.8:1 and evap. Pressure is (4) kPa.

Fig. (6) shows the variation of the temperature of unit components with the time when the working pressure is (3) kPa, while the MR is the same as in above. It can be seen from the figure that, there is insignificant effect on the performance of the machine as a result of the reduction in working pressure below (4) kPa. But, it can be seen that the evaporator temperature is slightly below (0)°C, which means the formation of ice. The reduction in evaporator temperature is due to the low saturation temperature that corresponding to the saturation pressure.

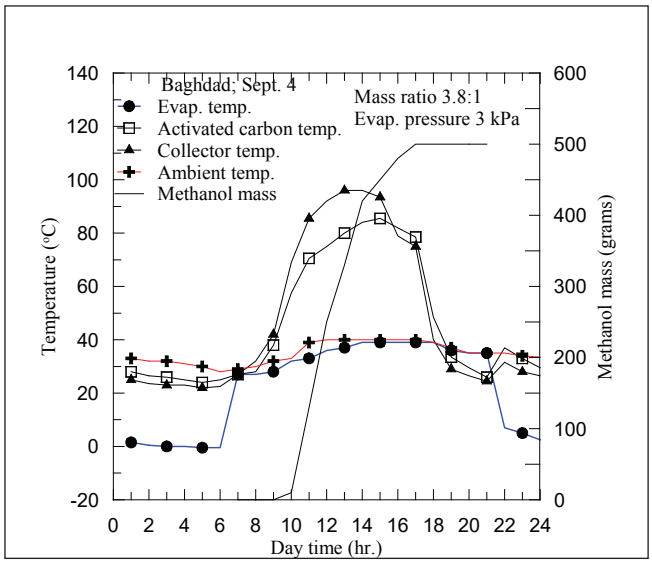

Fig. (6): The variation of condensate methanol mass and cycle components temperatures with the day time, mass ratio is 3.8:1 and evap. Pressure is (3) kPa.

Fig. (7) shows the variation of variables mentioned above when the MR reduces to (3.2:1), and the working pressure is (3.5) kPa. It can be seen from the figure that the mass of condensate methanol is about (395) grams, which offers more heat of evaporation that must be delivered from evaporator water bath, and also it can be seen that the evaporator temperature bellows (0) °C, which means freezing of water in the evaporator water bath.

5. Conclusions

The feasibility of ice production or even cooling using solar energy was studied; it was found that from the study:

1. it is possible to produce about (1) kg of ice per day when the collector area is (0.221) m^2, which is equivalent to about (4.5) kg ice/m^2.day.
2. The solar COP of the machine ranged from (0.1 to 0.36).
3. Working pressure and mass ratio of active carbon to methanol have a significant effect on the performance of the machine. The best mass ratio of active carbon to methanol is about (3.8:1), when the working pressure is (4) kPa.

References:

[1] M. Pons and J. J. Guilleminot, "Design of an Experimental Solar-Powered, Solid-Adsorption Ice Maker," J. Sol. Energy Eng., vol. 108, no. 4, pp. 332–337, Nov, (1986).

[2] F. Lemmini and F. Meunier, "Simulation of an adsorptive solar refrigerator operating in Morocco," J. Islam. Acad. Sci., vol. 3, no. 4, pp. 273–279, (1990).

[3] A. Boubakri, J. J. Guilleminot, and F. Meunier, "Adsorptive solar powered ice maker: experiments and model," Sol. Energy, vol. 69, no. 3, pp. 249–263, Jan, (2000).

[4] L. Y. and R. Z. Wang, "Adsorption Refrigeration: A Survey of Novel Technologies," Recent Patents on Engineering, 31-Jan-2007, [Online]. Available: http://www.eurekaselect.com/89853/article. [Accessed: 10-Aug, (2018).

[5] A. P. F. Leite, M. B. Grilo, R. R. D. Andrade, F. A. Belo, and F. Meunier, "Experimental thermodynamic cycles and performance analysis of a solar-powered adsorptive icemaker in hot humid climate," Renew. Energy, vol. 32, no. 4, pp. 697–712, Apr, (2007).

[6] Freni, G. Maggio, S. Vasta, G. Santori, F. Polonara, and G. Restuccia, "Optimization of a solar-powered adsorptive ice-maker by a mathematical method," Sol. Energy, vol. 82, no. 11, pp. 965–976, Nov, (2008).

[7] S. Vasta, G. Maggio, G. Santori, A. Freni, F. Polonara, and G. Restuccia, "An adsorptive solar ice-maker dynamic simulation for north Mediterranean climate," Energy Convers. Manag., vol. 49, no. 11, pp. 3025–3035, Nov, (2008).

[8] H. Luo, R. Wang, and Y. Dai, "The effects of operation parameter on the performance of a solar-powered adsorption chiller," Appl. Energy, vol. 87, no. 10, pp. 3018–3022, Oct, (2010).

[9] A. H. N. Khalifa, F. M. Hussein, and F. M. Hadi, "Experimental Study on Two Beds Adsorption Chiller with Regeneration," Mod. Appl. Sci., May, (2013).

[10] M.A, H. Ammar, B, Benhaoua, M, and Balghouthi, "Simulation of tubular adsorber for adsorption refrigeration system powered by solar energy in sub-Sahara region of Algeria," Energy Convers. Manag., (2015).

[11] A. H. N. Khalifa, A. H. Jabbar, and J. A. Muhsin, "Effect of Exhaust Gas Temperature on the Performance of Automobile Adsorption Air-Conditioner," Am. J. Eng. Appl. Sci., vol. 8, no. 4, pp. 575–581, Oct. (2015).

[12] W. Chekirou, N. Boukheit, and A. Karaali, "Performance improvement of adsorption solar cooling system," Int. J. Hydrog. Energy, vol. 41, no. 17, pp. 7169–7174, May, (2016).

[13] N. Cherrad, A. Benchabane, L. Sedira, and A. Rouag, "Transient numerical model for predicting operating temperatures of solar adsorption refrigeration cycle," Appl. Therm. Eng., vol. 130, pp. 1163–1174, Feb, (2018).

[14] Z. F. Li and K. Sumathy, "A solar-powered ice-maker with the solid adsorption pair of activated carbon and methanol," Int. J. Energy Res., vol. 23, no. 6, pp. 517–527, May, (1999).

Wastewater Treatment Modeling Using Combined System Bio-Filter With Activated Sludge

*Ahmed Samir Naje
Department of Architect Engineering, College of Engineering, Almuthana University, Almuthana Governorate, Iraq.

Received Date: 10 / 8 / 2018
Accepted Date: 16 / 12 / 2018

الخلاصة

الغرض من هذه المقالة هو تقييم إمكانيات إزالة النتروجين والفوسفات لتعزيز إزالة المركبات البيولوجية في محطة معالجة مياه الصرف الصحي باستخدام النترجة المنفصلة على الأغشية الثابتة. استند التحليل على محاكاة عدة متغيرات للنظام المدمج: أداء الحمأة المنشطة بالغشاء الثابت. تم استخدام موديل الحمأة المنشط ASIM 2d المرتبط بموديل تحولات الملوثات في الغشاء الثابت. أجريت نتائج التحاليل وفقاً لمعايير المدخلات: المعدل اليومي لمياه الصرف الصحي، درجة الحموضة، المتطلب الكيميائي للاوكسجين، قيم العوالق الصلبة الكلية، النتروجين الكلي، نيتروجين النيترات، الفوسفور الكلي، والقلوية. أشارت النتائج إلى إمكانية تضمين الغشاء الثابت في تكنولوجيا الحمأة المنشطة لتحسين إزالة النيتروجين والفوسفور من مياه الصرف الصحي. تم إجراء عملية النترجة في غشاء ثابت، في حين تم تنفيذ إزالة النيتروجين والفوسفور من مياه الصرف الصحي في غرف الأكسدة التي تعمل بتقنية الحمأة المنشطة. تضمن عملية ازالة النتروجين والفوسفات الى هبوط مستوى الفوسفور بنسبة (81٪)، ولكن فقط إذا استهلكت الكائنات الدقيقة الموجودة في حجرة الأكسدة بسهولة الطبقة التحتية القابلة للتحلل وإذا كانت هناك نترات كافية.

الكلمات المفتاحية

مياه الصرف المنزلي، الحماة المنشطة، الاغشية الثابتة، ازاله النترجة، ازالة الفوسفات، النموذج الرياضي.

Abstract

The purpose of this article is evaluation of the possibilities of using denitrifying dephosphatation to enhance biogenic compounds' removal in the wastewater treatment plant with separated nitrification on fixed-film. The analysis was based on the multi-variant simulations of the combined system: fixed film activated sludge performance. Activated sludge ASIM 2d model related with the model of pollutions transformations in fixed film was used. The results of exploitation analyses were performed according to the input parameters: average daily rate of wastewater, pH, COD values, total suspended solids, total Kjeldahl nitrogen, nitrate nitrogen, total phosphorus and alkalinity. The results indicated that there is a possibility of including fixed film in the activated sludge technology in order to improve nitrogen and phosphorus removal from the wastewater. Nitrification process will be performed in fixed-film, whereas nitrogen and phosphorus removal from the wastewater will be performed in anoxic chambers which operate in the activated sludge technology. Denitrifying dephosphatation process guarantees the high level of total phosphorus reduction (81%), but only if the whole easily decomposable substrate will be consumed by microorganisms in the anoxic chamber and if enough nitrates will be present in the environment.

Keywords

Household wastewater, Activated sludge, Fixed-film, Denitrifying, Dephosphatation, Mathematical model.

1. Introduction

Wastewater treatment plants which were put into operation in the late (70s and 80s) of (20^{th}) century do not fulfill the normative requirements any more, particularly regarding biogenic compounds removal [1]. Treatment plant modernization means liquidation of biofilters. Normally a designer does not see the possibility of including biofilters into biological dephosphatation scheme coupled with nitrification and gentrification. Possibility of integration biofilters and activated sludge to intensify biogenic compounds removal from the wastewater occurred when bacteria capable of denitrifying dephosphatation were identified [2,3]. Bacteria that accumulate phosphates may be divided into two groups: bacteria that accumulate phosphates from wastewater with oxygen as an electron acceptor and with nitrites as electron acceptors [4,5,6,7,8,9]. The first one belongs to classic anaerobic-aerobic system whereas in the second case phosphorus is removed in anaerobic48 anoxic zones. Denitrifying dephosphatation allows for elimination of oxygen chamber. In such system competition between microorganisms is directed towards predomination of bacteria capable of dephosphatation in anoxic conditions. By avoiding unnecessary aerobic usage of organic compounds, denitrifying potential of the system increases and enables effective wastewater dephosphatation with low BOD_5/P ratio. Closing dephosphatation in anaerobic-anoxic cycle allows for separation of nitrification and dephosphatation system, and conducting it on isolated biofilters or on separate part of activated sludge [10,11,12]. Dephosphatation can be also effective when nitrites act as electron acceptors. However they cannot occur in to high concentration due to their inhibiting influence on process of excessive phosphates intake by microorganisms, which continues even after cessation of NO_2-N dosage into the sludge. According to Huang et al. (2015), critical concentration of nitrite nitrogen in anoxic chamber should not exceed (5-8) mgN-$NO_2 \cdot dm^3$ [13]. Separation of nitrification beyond the traditional system leads to increasing the percentage of nitrifiers in biomass, thus increase in productivity of this process [14,15]. Introduction of nitrification on biofilters into activated sludge systems allows for more effective nitrogen removal in low temperatures without necessity of increasing volume of oxygen chamber [16,17,18]. Removal of higher amount of organic compounds in anoxic conditions stands for deeper denitrification and in consequence reducing energy consumption for aeration and lower production of excess sludge. Process of denitrifying dephosphatation is possible in flow and cyclically operating systems. Research on denitrifying dephosphatation in SBR reactor carried out by Styka (2004) showed that due to introduction of anoxic phase in the middle of aerobic phase in anaerobic-aerobic SBR reactor with quick filling, fraction of denitrifying bacteria PAO (Phosphate Accumulating Organisms) increased from (16 to 44%) of the total

number. DEPHANOX system is an example of practical realization of nitrification separated on biofilter in a flow system [19]. This system reduces general phosphorus by (71%) with 7.8 $mgP \cdot gsmo^{-1} \cdot d^{-1}$ of its intake, whereas efficiency of nitrate nitrogen reduction reached about (60%) with (30) $mgNO_3\text{-}N \cdot gsmo^{-1} \cdot d^{-1}$ speed of the process. DEPHANOX system also contributed to improvement of sludge sedimentation capacity (sludge index equaled $ml \cdot g^{-1}$) [20,21,22]. The objective of the paper is to evaluate possibilities of removal of biogenic compounds using denitrifying dephosphatation process in a treatment plant with nitrification separated on biofilters. This evaluation was carried out on the basis of data from one of municipal wastewater treatment plants in Kuala lumpur Malaysia, in which only trickling filter technology is currently used as a biological component.

2. Material and methods

Results of municipal wastewater treatment obtained in exploited mechanical-biological wastewater treatment plant in kualalumpur-Malaysia were the basis for performed calculations. Wastewater from about (14) thousand of citizens runs into the treatment plant. The designed wastewater treatment plant capacity equals (8620) m^3/d. The following objects are included into the technological chain of the analyzed treatment plant: horizontal sand separator with manual sand removal, two Imhoff's primary settling tanks, two submerged anoxic filters filled with BIOPEX packages (currently out of exploitation), two I stage trickling filters filled with quartzite break stone of 80 $m^2 \cdot m^{-3}$ active surface, three vertical intermediate settling tanks, II stage sewage pump station, three II stage biofilters (two with quartzite break stone filling and one filled with BIOPEX packages), coagulant PIX dosing station and two II stage secondary settling tanks (vertical and radial) as shown in Fig.(1). In determining the configuration of each variant of modernized in the future technological chain of wastewater treatment a principle of maximum use of objects, which already exist in the treatment plant, and minimum dosage of chemicals was applied. Computations were carried out for five technological variants as shown in Fig. (2).

Differences in variants I-V result from adopted values of anoxic chamber volume and oxygen concentration. In general, wastewater treatment processes in the discussed variants run as follows: after initial treatment in primary settling tank wastewater goes to anaerobic chamber where orthophosphates are released by bacteria cells. Energy to obtain and converse substrates (easily decomposable organic carbon) into polyhydroxyalkanoates, mainly poly-β- hydroxybutyrate, accumulated in PAO microorganisms' cells is derived from hydrolysis of cell polyphosphates. Subsequently, wastewater runs into intermediate settling tank, where residue is separated in sedimentation process. Supernatant rich in orthophosphates and

ammonium nitrogen with small amount of organic matter is transferred to trickling filter, in which nitrification of ammonium nitrogen occurs.

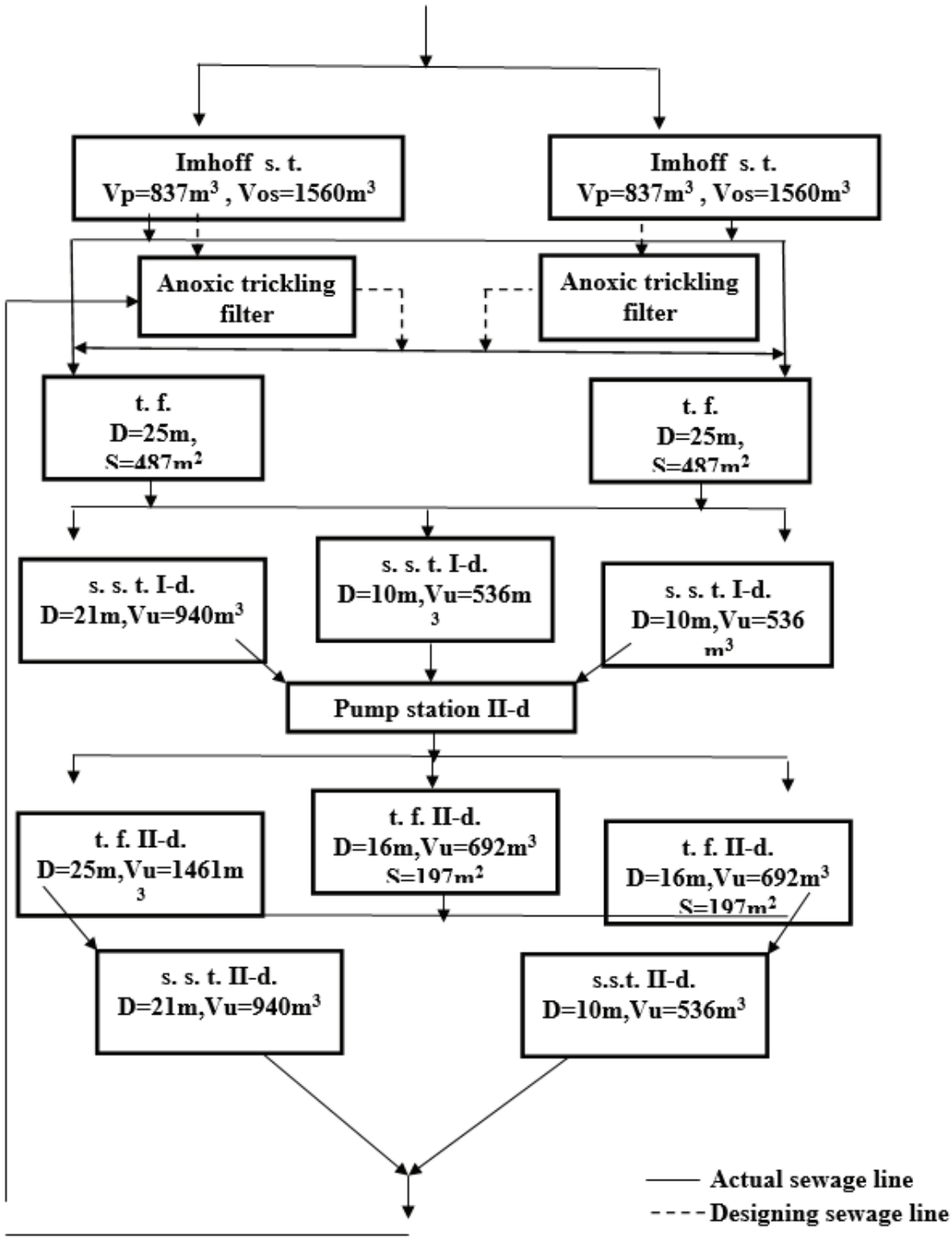

Fig. (1) The exploited technological chain of the analyzed wastewater treatment plant: Imhoff s. t. - Imhoff settling tank; t. f. - trickling filter; s. s. t. I-d. - secondary settling tank first degree; Pump station II-d. - Pump station second degree; t. f. II-d. - trickling filter second degree; s. s. t. II-d. - secondary settling tank second degree

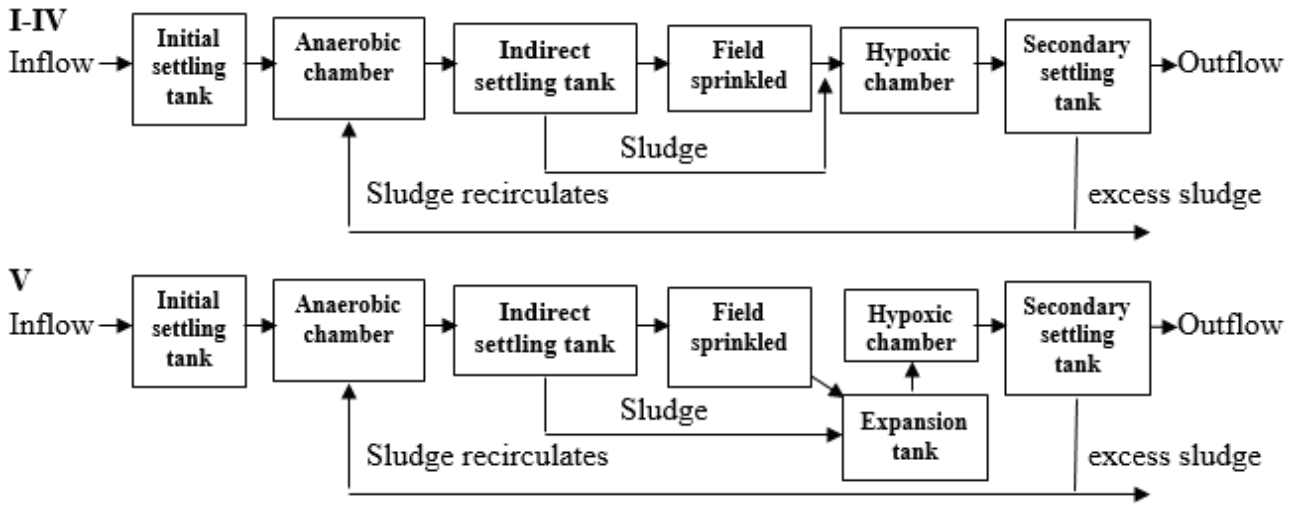

Fig.2 The technological variants of the wastewater treatment plant facilities, included in the variant calculations.

Sediment from the intermediate settling tank with PAO bacteria is transported to anoxic chamber to which also nitrified wastewater from biofilter, rich in nitrates, flow in. In anoxic chamber with low oxygen concentration and presence of nitrates as electron acceptors excessive intake of dissolved orthophosphates with simultaneous denitrification of nitrates takes place. The last element of the system is the secondary settling tank in which activated sludge is separated from the treated wastewater by sedimentation. Treated wastewater runs into the collector and sludge is partially recirculated to anaerobic chamber, while the remainder is discharged outside the system as the excess sludge.

Table (1) compares technical parameters of devices included in the analyzed variants. Equipment from the mechanical part of the wastewater treatment plant, II stage of bio filter with BIOPEX packages filling, intermediate and secondary settling tanks from the previously exploited technological chain were left for operation, but I and II stage filters filled with quartzite break stone will be eliminated. Two existing chambers with submerged beds, which currently are not exploited, will be adapted as anaerobic chamber. In proposed variants anoxic chamber will be a new object created within modernization efforts.

Table (1) Technical characteristics of devices included in the analyzed variants

Device	Device characteristics				
Variant	I	II	III	IV	V
Primary settling tank	Settling tank volume V = 837m^3; Depth of the flow part H = 2.5m; Amount of sludge/wastewater = 0.20; hydraulic load O_h = 13.44 m^3·m^2·d^{-1}				
Anaerobic chamber	Oxygen concentration O_2 = 0.0 mg·dm^3; Chamber volume V = 100 m^3; Retention time T_h = 0.4 h.				

Intermediate settling tank	Amount of sludge/wastewater = 0.60
Trickling filter	BIOPEX packages; Specific surface A = 150 $m^2 \cdot m^3$, Filter volume V = 1460 m^3, Oxygen concentration O_2 = 2 $mg \cdot dm^3$
Anoxic chamber	Volume Volume Volume Volume Volume 400m^3 400m^3 1000m^3 1000m^3 600 m^3 O_2 = 0.8 O_2 = 0.5 O_2 = 0.8 O_2 = 0.5 O_2 = 1.0 $mg \cdot dm^3$ $mg \cdot dm^3$ $mg \cdot dm^3$ $mg \cdot dm^3$ $mg \cdot dm^3$ Depth H=4m Depth H=4m Depth H=4m Depth H=4m Depth H=4m
Secondary settling tank	Volume V = 1880 m^3; Depth H= 4 m; Hydraulic load O_h = 9.74 $m^3 \cdot m^2 \cdot d^{-1}$; Sediment load O_o = 4.77 $kg \cdot m^{-2} \cdot d^{-1}$; Amount of sludge/wastewater = 0.20; Reactive settling tank

Although it was assumed that in anoxic chamber denitrifying dephosphatation will occur, dissolved oxygen concentration was accepted to range from (0.5 to 1.0) $MgO_2 \cdot dm^{-3}$ for additional intake of phosphates remaining in the wastewater by microorganisms. Calculations of pollution removal capacity in analyzed variants of technological chain were based on commonly used mathematical models of pollutants transformation in bioreactors with activated sludge and bio filters. In recent years such attitude is more and more common in simulation of exploited treatment plants as well as in designing new technological systems of treatment. Processes related to wastewater treatment can be predicted using artificial neural networks (ANN), where the number of input variables can be separated by cluster analysis [23,24] or by the principal component analysis [25,26]. Models ASIM (Activated Sludge Simulation Model) widely discussed in literature, where the researchers are leading in the modeling issues of operation of systems with activated sludge [27,28, 29,30,31,32,33]. In the present work, the activated sludge chambers were based on ASIM 2d model. This model represents continuation of the previous version called ASIM 2 [34,35,36]. It takes into account dissolved substance which consists of fermentation products, wastewater alkalinity, very easily and easily decomposable organic matter, nitrogen dioxide as denitrification product, ammonium and ammonium nitrogen, nitrite and nitrate nitrogen, dissolved oxygen and inorganic phosphates. This model also includes non-dissolved substances, such as: nitrifying organisms, heterotrophic aerobic and facultative anaerobic organisms, indecomposable molecular organic substance, salts and metal hydroxides included in processes of chemical phosphorus precipitation, PAO phosphate accumulating bacteria, cell components of bacteria e.g. poly-β-hydroxybutyrates, polyphosphates,

slowly decomposable hydrolysed organic substances and general suspended solids [37]. ASIM 2d model considers (21) unitary processes qualified into (5) groups of: hydrolysis, processes with heterotrophic bacteria, processes with autotrophic bacteria, polyphosphate accumulating bacteria and chemical processes. Mathematical description of denitrification processes with polyphosphates accumulating bacteria was included in this model. Simulative calculation of activated sludge chambers was realized using BioWin 2 software [38]**.** To realize the objective of the research, model of pollutants' transformation on biofilter, described in Rauch's et al. (1999) was also included in ASIM 2d model [39]. This model consists of the following assumptions: biological membrane is of homogenous structure and density throughout the depth, microorganisms are uniformly distributed in the biological membrane, reactions occur with first-order kinetics and dissolved substances are immediately diffused by biological membrane. Transformation of organic matter and nitrification of ammonium nitrogen in biological membrane were calculated according to the scheme given by Henze et al. (2002) [40]. Results of exploitation research on the objective treatment plant, which included: average daily wastewater inflow, pH reaction, COD values (total and dissolved), total suspended solids, Kiejdahl's general nitrogen, nitrate nitrogen, general phosphorus and alkalinity were adopted as input parameters for calculations. Wastewater composition was determined by referential methods stated by standards [40]. Analyses of total and dissolved COD content (after filtering through a filter of (0.45) µm pore size in raw wastewater were performed and then share of each fraction was defined according to methods described by Henze et al. (2002) [40]. Life time of sludge was at 10 d and constant temperature at (T = 20ºC.) Constants of reaction kinetics were implemented from the range given by Henze et al. (1999) [41]; therefore, the obtained results can only illustrate the potential possibility of adaptation the existing biofilters into chain with activated sludge. All simulations were performed in set conditions.

3. Results and Discussion

3.1 Technological chain of wastewater treatment plant

The main reason why variant calculations of technological chain of the wastewater treatment plant were undertaken was because the treated wastewater did not meet conditions from the water law permission for the objective treatment plant for general nitrogen and phosphorus concentrations, which was confirmed by the statistical analysis of the obtained outcomes. The results showed that concerning BOD_5 values correctly for (66.2%) of year, COD = (99.4%), total suspended solids = (98.6%), general nitrogen = (3%) and general phosphorus = (89.8%). Considering insufficient capacity of wastewater treatment concerning removal of biogenic compounds, variant deliberations were carried out to search

for optimal solution of technological chain which would guarantee reliable operation of the object, regarding nitrogen and phosphorus removal from the wastewater and would also enable maximum usage of the existing objects. Classical technological systems with activated sludge need to modify in order to intensify the process of biogenic compounds removal [40]. Table (2) presents average values of each COD fraction in raw wastewater, which were used for modeling. Dissolved COD fraction constituted less than (21%) of total COD whereas share of decomposable (dissolved and molecular) organic substances equaled (82%) in total COD.

Table (2) COD fraction in wastewater running into the treatment plant.

COD fraction	Value, mg/dm^3
Dissolved decomposable S_{BS}	110.53
Dissolved indecomposable S_{US}	34.54
Molecular decomposable S_{BP}	456.92
Molecular indecomposable S_{UP}	89.81

It suggests that the analyzed wastewater is susceptible to biochemical decomposition. Table 3 shows average values of the analyzed pollution indexes in the treated wastewater obtained in performed calculations compared to values gained from the exploitation of the existing technological chain. Variants I – IV lower treatment capacity was obtained for organic matter in comparison to the existing object. BOD_5 values were significantly higher than the admissible level of (15) mg $O_2 \cdot dm^{-3}$. However, it was observed that increase of anoxic chamber volume from (400 to 1000) m^3 and increase of oxygen concentration from (0.5 to 0.8) mg $O_2 \cdot dm^{-3}$ causes increase of organic pollutants' reduction. It results from the fact that although nitrified wastewater after biofilter with low amount of organic pollutants flows into the anoxic chamber, it is still overloaded with organic matter from the residue after intermediate settling tank. Calculations showed that the average BOD_5 value in the sludge was (1117.9) mg $O_2 \cdot dm^{-3}$, and COD (2550.3) mg $O_2 \cdot dm^{-3}$.

Table (3) Capacity of selected pollution indexes observed in exploited technological chain and calculated for analyzed variants.

Pollutants character	RWW	Removal efficiency of TWWTP* (%)	Removal efficiency variant (%)				
			I	II	III	IV	V
BOD_5 (mgO2·dm^{-3})	267.01	95	83	81.5	89	88	96

COD($mgO_2 \cdot dm^{-3}$)	690.83	92	90	88	92.5	91.5	95
TSS ($mg \cdot dm^{-3}$)	209.23	91	98.5	99.5	99.5	99.5	98
General nitrogen ($mg \cdot dm^{-3}$)	62.37	58.5	70	70.5	72	73	42
General phosphorus ($mg \cdot dm^{-3}$)	9.03	62	65	65	66	68	81

*Treated wastewater of treatment plant

High load of sludge with organic substances causes increase of oxygen demand. Keeping low oxygen concentration in anoxic chamber causes substrate to be only partially mineralized which results in low BOD_5 and COD production. It also results from low activity of activated sludge in anoxic chamber. The calculated respiration speed for variants I and II ranged from (0.12 to 1.25) mg $O_2 \cdot gsm^{-1} \cdot h^{-1}$, and for variants III and IV (7.54 and 9.67) mg $O_2 \cdot gsm^{-1} \cdot h^{-1}$, respectively. For total suspended solids obviously higher reduction is observed in variants I-IV in comparison to the one obtained in the existing object. In each variant concentration of total suspended solids in the outflow was lower than the admissible value of (35) $mg \cdot dm^{-3}$. Introducing anoxic chamber after nitrifying filters contributes to increase of removal of general phosphorus from wastewater. It is mainly caused by significant ammonium nitrogen reduction in the wastewater in the nitrifying filter and its slight increase in anoxic chamber.

3.2 Nitrogen and phosphates Removal calculations

Clear nitrate nitrogen reduction resulting from classic dissimilative denitrification is not observed Fig.(3). In variants I-IV general nitrogen concentration in the outflow is significantly lower than the one obtained in the real object, however in each case the admissible value of (15) $mg \cdot dm^{-3}$ is exceeded. In variants I-IV significant improvement of phosphorus removal in comparison to the existing treatment plant is not observed. Average concentrations of general phosphorus obtained from the calculations are slightly lower than the real values for the analyzed object and exceed the admissible value of (2) $mg \cdot dm^{-3}$.

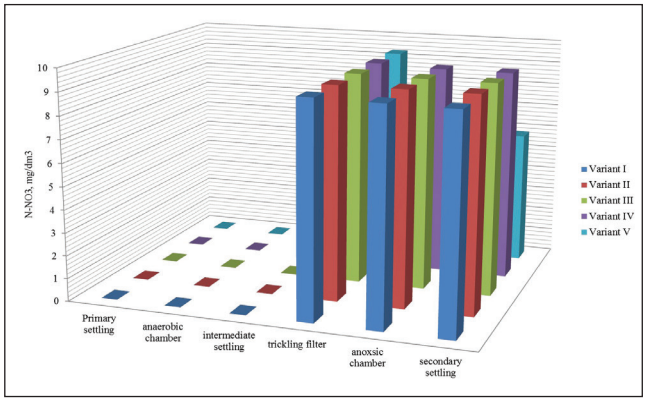

Fig. (3) Profile of concentration values of nitrate nitrogen for analyzed calculation variants.

It is worth noting, that phosphorus is removed only biologically in the analyzed variants, whereas in the existing treatment plant it is removed by chemical precipitation

with PIX coagulant, dosed at the inflow to the II stage secondary settling tank. Therefore, possible modernization of technological chain carried out accordingly to the discussed variants would contribute to lowering the costs of wastewater treatment. Together with increase of anoxic chamber volume and decrease of dissolved oxygen concentration from (0.8 to 0.5) mg $O_2 \cdot dm^{-3}$ increase of consumed phosphates can be noticed as shown in fig. (4). Considering the fact that in anoxic chamber nitrate nitrogen occurred in concentration of about (9) mg $N\text{-}NO_3 \cdot dm^{-3}$, there was a possibility of denitrifying dephopsphatation, because $N\text{-}NO_3$ was electron acceptor for PAO bacteria. On the other hand, speed of phosphorus intake in anoxic chamber could have been be limited by insufficient nitrate. Phosphates were partially consumed by PAO bacteria when initial concentration of $N\text{-}NO_3$ equaled (25) $mgN\text{-}NO_3 \cdot dm^{-3}$, whereas practically total phosphates intake occurred with initial $N\text{-}NO_3$ concentration of (60) $mgN\text{-}NO_3 \cdot dm^{-3}$ and lasted until their complete depletion. COD/N ratio confirms nitrates deficiency for denitrifying dephosphatation. Optimum value of this ratio should amount (3.5) g COD/gN. With ratio higher than the given one (in the analyzed wastewater it was 11.1) incomplete phosphorus removal occurs, caused by deficiency of nitrates [42,43,44].

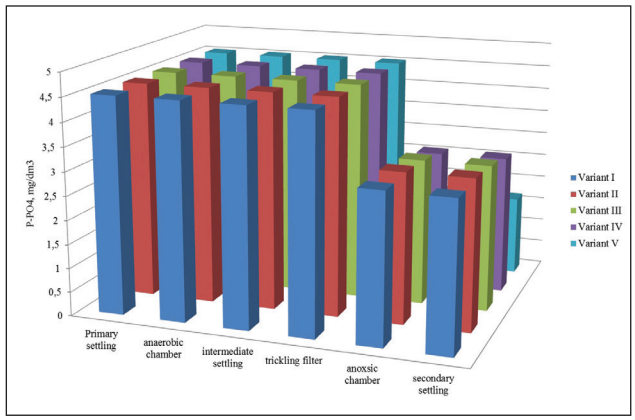

Fig. (4) Profile of concentration values of phosphates for analyzed calculation variants.

In variant V volume of anoxic chamber was decreased to (600) m^3 and oxygen concentration was increased to (1) mg $O_2 \cdot dm^{-3}$. As a result, significant improvement in organic pollutants removal was observed in comparison to variants I-IV. Average BOD_5 and COD values at the outflow from the secondary settling tank were lower than the admissible value defined in the water-law permission. Concentration of total suspended solids slightly increased at the outflow in comparison to previously analyzed variants. General nitrogen reduction was significantly worse and its average concentration at the outflow reached (36.44) $mg \cdot dm^{-3}$ and clearly exceeded value obtained in the existing object and admissible value from the water law permission. This situation is mainly caused by significant increase of $N\text{-}NH_4$ concentration in anoxic chamber to the level of (26.14) $mgN\text{-}NH_4 \cdot dm^{-3}$. Increasing of oxygen concentration in anoxic chamber caused decrease of denitrification process, which

in turn caused increase of general nitrogen concentration at the outflow of the treatment plant. At the same time, such action caused increase of phosphorus consumed by PAO bacteria (general phosphorus concentration at the outflow of the settling tank was (1.74) mg $P_{og} \cdot dm^{-3}$ and does not exceed the admissible value. In anoxic chamber bacteria do not have organic acids to their disposal so only organisms capable of using stored, easily decomposable substrates exclusively in presence of nitrates as an electron acceptor are promoted [45].

4. Conclusion

The use of biofilters as biological stage in wastewater treatment plant exhibits a significantly removal of organic pollutants (BOD_5, COD) and total suspended solids. General phosphorus may be removed only by chemical precipitation. There is a possibility of including biofilters into activated sludge technology in order to improve nitrogen and phosphorus removal from the wastewater. Nitrification process will be carried out on biofilters, whereas in anaerobic and anoxic chambers operating in activated sludge technology process of nitrogen and phosphorus removal will take place. Separation of nitrifiers from heterotrophic organisms causes lack of competition between these organisms and higher stability of nitrifiers population. In systems with nitrification in so called"side sequence" denitrifying dephosphatation process will be possible. Using of denitrifying dephosphatation process reduces energy consumption of the system related to decreased oxygen need. Calculations showed that even with oxygen concentration of (1) $mgO_2 \cdot dm^{-3}$ in anoxic chamber, denitrification as well as orthophosphates' intake were carried out by microorganisms. It results from the fact that PAO bacteria can use oxygen as well as nitrates as electron acceptors. Effective biological phosphorus removal is also possible, therefore amount of chemicals used for the process may be reduced Denitrifying dephosphatation process guarantees high general phosphorus removal at (81%) provided that total easily decomposable substrate will be consumed by microorganisms in anaerobic chamber and that sufficient amount of phosphates will be available. Calculations showed that integration of biofilters with activated sludge in flow system allows for high reduction of organic pollutants, total suspended solids and biogenic compounds from the wastewater. Considering general nitrogen reduction, the most favorable variant was the system with anoxic chamber (1000) m^3 in volume and oxygen concentration equal to (0.5) $mgO_2 \cdot dm^{-3}$, whereas for phosphorus removal the solution with anoxic chamber (600) m^3 in volume and oxygen concentration of (1) mg $O_2 \cdot dm^{-3}$. ASIM 2d model seems to be extremely useful tool for designing and simulation of wastewater treatment plant operation. It follows from the fact that it enables simulation of most processes occurring in bioreactor with activated sludge. This model considers

mathematical description of denitrification processes with phosphate accumulating bacteria.

Acknowledgements

The author thank Al-muthanna University, Universiti Teknologi Malaysia and Ministry of Higher Education and scientific research of Iraq for supporting this research.

References

[1] BUGAJSKI P., CHMIELOWSKI K., KACZOR G. Pol. J. Environ. Stud., 25 (4), 1421, (2016).
[2] WĄSIK E., CHMIELOWSKI K. Ecological Engineering, 106, 378, (2017).
[3] MADEROVAZ., BALDIKOVAE., POSPISKOVA A., SAFARIK I., SAFARIKOVA M. International Journal of Environmental Science and Technology, 13 (7), 1653, (2016).
[4] XIAO-MEI L., MING-FEI S., CHAO-LIN L., JI L., XIN-IEI G., FEI-YUN S. Microbes Environ., 29 (3), 261, (2014).
[5] RUBIO-RINCÓN F., LOPEZ-VAZQUEZ C., WELLES L., VAN DEN BRAND T. ABBAS B., VAN LOOSDRECHT M., BRDJANOVIC D. Biotechnol., 101, 6229, (2017).
[6] WILFERT P., KUMAR P. S., KORVING L., WITKAMP G. J., VAN LOOSDRECHT M. C.M. Environ. Sci. Technol., 49, 9400, (2015).
[7] SCHOUMANS O. F., BOURAOUI F., KABBE C., OENEMA O., VAN DIJK K. C. Ambio, 44, 180, (2015).
[8] HIROTA R., KURODA A., KATO J., OHTAKE H. J. Biosci. Bioeng., 109 (5), 423, (2010).
[9] CÉDRIC T., HUU-THANH N., BROGNAUX A., DELEPIERRE A., DE CLERCQ L. CHARLIER R., MICHELS E., MEERS E., DELVIGNE F. Sensor, 16 (6), 797, (2016).
[10] CAPODAGLIO A. G., HLAVÍNEK P., RABONI M. Journal of Applied Science, 11 (2), 250, (2016).
[11] NASEER R., ABDUALHAIL S., XIWU L. Saudi J. Biol. Sci., 20 (1), 11, (2013).
[12] FUDALA-KSIĄŻEK S., KULBAT E., ŁUCZKIEWICZ A. Environmental Technology, 38, 1, (2017).
[13] HUANG J., YANG P., LI C., GUO Y., LAI B., WANG Y., FENG L., ZHANG Y. Biotechnol. Res. Int. 798-397), (2015).
[14] TODT D., DORSCH P. Rev. Environ. Sci. Biotechnol., 15 (3), 355, (2016).
[15] COSKUN D., BRITTO D. T, SHI W., KRONZUCKER H. J. Nature Plants, 6, 170-174, (2017).
[16] RABONI M., TORRETTA V., VIOTTI P., URBINI G. Revista Ambiente & Agua, 8 (3), 22, (2013).
[17] PRAMANIK B. K., FATIHAH S., SHAHROM Z., AHMED E. Journal of Engineering Science and Technology, 7 (4), 428, (2012).
[18] CAPODAGLIO A. G., HLAVÍNEK P., RABONI M. An Interdisciplinary Journal of Applied Science, 11 (2), 250, (2016).
[19] CAPODAGLIO A. G., HLAVÍNEK P., RABONI M. Journal of Applied Science, 11 (2), 250, (2016).
[20] STYKA W. Conference materials: Research, design and operation of sequential reactors, 35, Poland, (2004).
[21] BORTONE G., SALTARELLI R., ALONSO V. SORM R., WANNER J., TILCHE Water Science and Technology, 34 (1-2), 119, (1996).
[22] KAPAGIANNIDIS A. G., ZAFIRIADIS I., AIVASIDIS A. Chemical Engineering Journal, 175 (1), 124, (2001).
[23] REN-JIAN D., JIN-SONG Z., and ZHI-JUN Q. Journal of Residuals Science & Technology, 13, 107, (2015).
[24] DÜRRENMATT D. J., GUJER W. 63 (6), 1153, (2011).
[25] BAYO J., LÓPEZ-CASTELLANOS J. Chemosphere, 155, 152, (2016).

[26] WĄSIK, E., CHMIELOWSKI, K., OPERACZ A. PCA Acta Sci. Pol. Form. Cir., 16 (1), 209, (2017).
[27] YANG Y., YU K., XIA Y., LAU F. T. K., TANG D. T. W., FUNG W. C., FANG H. H. P., ZHANG T. Applied Microbiology and Biotechnology, 98 (12), 570-579, (2014).
[28] GUJER W., HENZE M. Water Science and Technology, 23 (4-6), 1011, (1991).
[29] GUJER W., LARSEN T. A. Water Science and Technology, 31 (2), 257, (1995).
[30] GUJER W., HENZE M., MINO T., MATUSO T., WENTZEL M. C., MARAIS G. V. R. Water Science and Technology, 31 (2), 1, (1995).
[31] GUJER W., HENZE M., MINO T., VAN LOOSDRECHT M. Water Science and Technology, 39 (1), 183, (1999).
[32] HENZE M., GUJER W., MINO T., MATUSO T., WENTZEL M. C, MARAIS G. V. R., VAN LOOSDRECHT C. M. Water Science and Technology, 39 (1), 165, (1999).
[33] SNIP L. J. P., BOIOCCHI R., FLORES-ALSINA X., JEPPSSON U., GERNAEY K. V.Water Science & Technology, 70 (7), 1251, (2014).
[34] WU X., YANGA Y., WU G., MAO J., ZHOU T. Journal of Environmental Management, 165, (2016).
[35] MACHADO V. C, LAFUENTE J., BAEZA J. A. Bioprocess and Biosystems Engineering, 37 (7), 1271, (2014).
[36] ALIKHANI J., TAKACS I., AL-OMARI A., MURTHY S., MASSOUDIEH A. Water Science &Technology, 75 (6), 1370, (2017).
[37] GUO L., VANROLLEGHEM P. A. Bioprocess and Biosystems Engineering, 37 (2), 151, (2014).
[38] IKUMI D. S., HARDING T. H., EKAMA G. A. Water Research, 56, 267, (2014).
[39] MAKINIA J. 390, United Kingdom, (2010).
[40] RAUCH W., VANHOOREN H., VANROLLEGHEM P. A. Water Research, 33 (9), 2148, (1999).
[41] HENZE M., HARREMOËS P., JANSEN J., ARVIN E. 3rd ed. Springer. (2002).
[42] KUBA T., LOOSDRECHT M., HEIJNEN J. Water Research, 30 (7), 1702, (1996).
[43] CHEN Y., LI B., YE L., PENG Y. Biochemical Engineering Journal, 93, 235, (2015).
[44] MENG J., LI J., LI J., DENG K., NAN J., XU P. Bioresource Technology, 243, 922, (2016).
[45] Du D., Zhang C., Zhao K., Sun G., Zou S., Yuan L., He S. Front. Environ. Sci. Eng., 12 (2): 1, (2018).